The Pennsylvania State University
The Graduate School

SENSOR-BASED MODELING AND ANALYSIS OF ADVANCED MANUFACTURING SYSTEMS FOR QUALITY IMPROVEMENTS

A Dissertation in
Industrial Engineering
by
Farhad Imani

Submitted in Partial Fulfillment
of the Requirements
for the Degree of

Doctor of Philosophy

August 2020

The dissertation of Farhad Imani was reviewed and approved by the following:

Hui Yang
Harold and Inge Marcus Career Associate Professor of Industrial and Manufacturing Engineering
Dissertation Advisor, Chair of Committee

Timothy W. Simpson
Paul Morrow Professor in Engineering Design and Manufacturing

Edward W. Reutzel
Director of Center for Innovative Materials Processing through Direct Digital Deposition (CIMP-3D)

Saurabh Basu
Assistant Professor of Industrial and Manufacturing Engineering

Steven J. Landry
Department Head and Professor of Industrial and Manufacturing Engineering

Abstract

Advanced sensing is increasingly invested in modern manufacturing systems to cope with the complexity and enhance information visibility, thereby leading to data-rich environments. Generated data provide unprecedented opportunities to investigate system dynamics and further improve quality monitoring and control for advanced manufacturing in real-time. However, high-dimensionality and complex structures of sensing data pose significant challenges. Realizing full potentials of sensing data depends to a great extent on the development of novel analytical methods and tools for effective modeling, monitoring, and control of manufacturing systems.

The research objective of this dissertation is to develop new learning methodologies for real-time quality monitoring and control of complex manufacturing systems. This body of research will enable and assist in 1) understanding the effect of process conditions on quality of manufacturing builds, 2) extracting sensitive features and characterizing patterns of image data, 3) diagnosing defects in low-volume and highly-customized production settings, and 4) handling high dimensional spatiotemporal data. My research accomplishments include:

- *Process mapping and monitoring of porosity in additive manufacturing (AM)*: In Chapter 2, spectral graph theory and multifractal analysis are developed to quantify the effect of process conditions on lack of fusion porosity in builds made using AM process, and subsequently, to detect the onset of process conditions that lead to lack of fusion porosity from in-process sensor data.

- *Multifractal and lacunarity analysis for nonlinear pattern characterization*: In Chapter 3, the joint multifractal and lacunarity analysis is designed to resolve local densities and characterize the filling patterns in image profiles. Further, we derive the composite quality index by computing Hotelling T^2 statistics from multifractal and lacunarity features for defect detection and characterization in ultra precision machining (UPM) and AM image profiles.

- *Image-guided variant geometry analysis of layerwise build quality*: In Chapter 4, we develop a tailored deep neural network (DNN) framework that learns the broad geometrical diversity of images from builds made with AM. The

proposed methodology leverages the computer-aided design (CAD) file to register the region of interest (ROI) in each layerwise image. Next, we propose a dyadic partitioning method to delineate variant ROI into distinctive regions with the same size and in multiple scales. Then, we leverage the semiparametric spatial model to characterize the complex spatial patterns in subregion ROIs. Finally, a DNN is designed to learn incipient flaws from spatial characterization images.

- *Spatiotemporal Gaussian process for AM quality monitoring*: In Chapter 5, a novel spatiotemporal Gaussian process (STGP) is introduced to model the standard geometric profile within ROIs and capture layer-to-layer spatiotemporal deviations for quality monitoring. Finally, we leverage the STGP model to develop new monitoring charts, namely, the STT2 and STLR tests, for the anomaly detection in AM processes. This framework enables on-the-fly assessment of AM build quality.

Table of Contents

List of Figures

List of Tables

Acknowledgments

I would like to express my sincere gratitude to my advisor, Dr. Hui Yang, whose continuous guidance, support, and encouragement made this dissertation possible. Throughout the past four years, I have been extremely inspired and tremendously benefited from his critical way of thinking about research problems. The experience of working with him will be a precious treasure in my future life. I also would like to thank my other committee members: Dr. Timothy Simpson for his suggestions and inputs that have shaped and improved my research; Dr. Edward Reutzel for his generous helps in providing important process insights; and Dr. Saurabh Basu for his helpful discussion and constructive suggestions. Furthermore, I want to express my sincere appreciation to my mentors, Dr. Soundar Kumara, Dr. Conrad Tucker, Dr. Jerome Jourquin, Dr. Prahalada Rao, and Dr. Changqing Cheng.

I would like to extend my deepest appreciation to all my labmates in Complex Systems Monitoring, Modeling, and Control Laboratory and Laboratory for Intelligent Systems and Analytics. My special thank to Ms. Ruimin Chen whose unconditional support allowed my study to go the extra mile and friendship made my pursuit of Ph.D. easier. I would also like to thank the Harold and Inge Marcus Department of Industrial and Manufacturing Engineering at Penn State for their generous help during my study. I appreciate the Center For Innovative Materials Processing Through Direct Digital Deposition (CIMP-3D) at Penn State for continuous support and provide data of this research.

I gratefully acknowledge the financial support from the National Science Foundation (No. CMMI-1617148), NSF Center for e-Design, Lockheed Martin, and National Institute of Standards and Technology (NIST) to support my research. Any opinions, findings, or conclusions found in this dissertation are those of the author and do not necessarily reflect the views of the sponsors.

To conclude, I wish to thank my family and dedicate this thesis to my parents, Habibollah and Fatemeh, for their endless love and enduring support, which helped me get through this agonizing period in the most positive way.

Chapter 1 Introduction

1.1 Motivation

Modern manufacturing industries are increasingly investing in sensing technologies to cope with the ever-increasing complexity of systems and improve information visibility. As a result, large amounts of data are readily available, which facilitate the effective in-situ modeling, monitoring, and control of advanced manufacturing systems. For example, high-resolution imaging systems are increasingly developed for real-time monitoring of the printing in additive manufacturing (AM) processes. The in-situ layerwise images enable the investigation of how process conditions impact the microstructures of fabricated builds and provide critical information to improve AM build quality. Also, microscopic images have been utilized in ultra precision machining (UPM) to detect the onset of surface defects for assuring product quality and minimizing subsequent reworks. As a result, sensing data provide an unprecedented opportunity to realize smart and automated manufacturing and are becoming a key enabler for enhancing competitiveness.

However, value of data does not hinge only on the volume, but also on hidden information and knowledge. Realizing full potentials of sensing data depends to a great extent on novel analytical methods and tools with effective information-processing capabilities, which requires addressing the following challenges posed by large and complex-structured data in advanced manufacturing:

- The presence of extraneous noise and uncertainty factors prevents the direct estimation of system dynamics. New data-driven approaches are urgently needed to capture systems evolution from sensing data.

- Advanced imaging technology brings a large amount of data with nonlinear and nonhomogeneous patterns, which calls for effective analytical methods to exploit the acquired information and extract sensitive features for process monitoring and control.

- State-of-the-art monitoring methodologies are not designed to leverage generated sensing data in modern manufacturing environments (e.g., the dearth of image data for a build due to the one-of-a-kind manufacturing process). There is a dire need for customized analytical methods that perform real-time anomaly detection in advanced manufacturing.

- Advanced sensing brings the proliferation of spatiotemporal data that are distributed in space and evolving over time. Both spatial and temporal correlations need to be effectively addressed for high-dimensional monitoring.

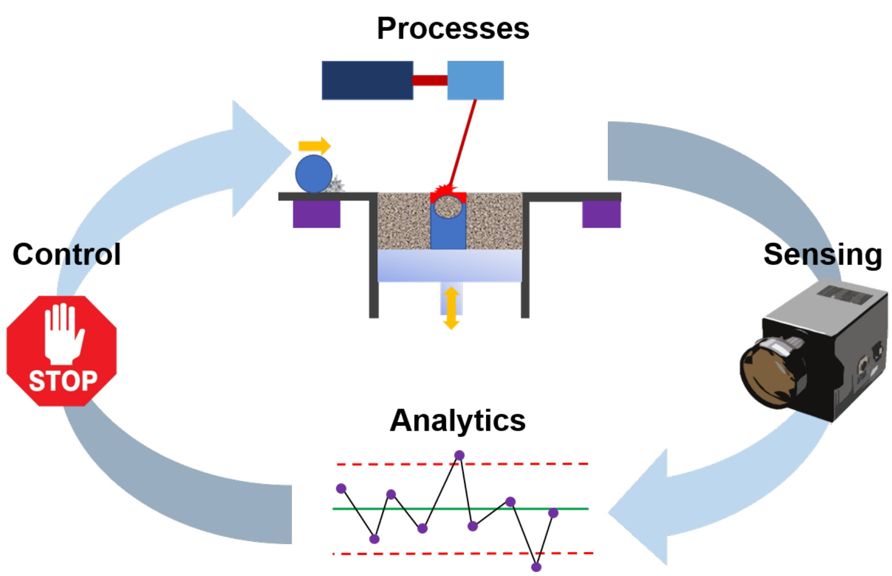

Figure 1.1. The overview of the proposed research.

As shown in Figure 1.1, the objective of this dissertation is to advance the knowledge on sensor-based modeling, monitoring, and control of advanced manufacturing for in-situ quality improvements.

1.2 Research Background

Modern manufacturing industries face increasing demands to provide highly personalized products and services to gain competitive advantages in the global market. This trend calls for the next-generation manufacturing system that is highly flexible and adaptive to complex and customized designs [3]. For example, AM is a group of processes that produce a 3D part layer by layer from computer-aided design (CAD) models. It enables the creation of complex, freeform geometries that are difficult, if not impossible, to realize using subtractive and formative manufacturing techniques [4]. Despite the great potential of AM to revolutionize manufacturing, process repeatability, and build consistency remain ongoing challenges [5].

Note that microstructure and mechanical properties of AM builds are significantly influenced by process variations and uncertain factors (e.g., materials with temperature dependency, transmission and absorption of laser energy, complicated cooling phenomena and materials, materials evaporation, thermal effects, hatching pattern, scanning velocity, and extraneous noises). This, in turn, causes the formation of various type of defects such as porosity (i.e., lack of fusion or entrapped gas), geometrical anomalies (e.g., curling, dimensional inaccuracy, and surface roughness), anisotropy and compromised phase stability, balling, cracks, and delamination (i.e., separation of consecutive layers) [6]. Defects substantially deteriorate build's strength, fatigue life, residual stress, and hardness, thereby flaw removal is critical to elongate mechanical properties of AM build.

Post-treatment techniques (e.g., machining and heat treatment) are conducive to rectify particular defects including trivial cracks, dimensional inaccuracy, and surface roughness on the exterior areas of finish build [7]. However, these expensive correction actions tend to be limited in addressing different types of anomalies and meeting challenging and stringent industrial requirements. Therefore, real-time quality monitoring becomes an urgent need for AM applications.

UPM is another type of advanced manufacturing processes and is widely used in fabrication of mirror finish surfaces for diverse engineering applications such as precision aluminum mirrors in lasers, hard drives, memory discs in the computer industry, rotating mirrors in copy machines, and optical elements of defense and aerospace industries [8]. Although UPM enables the production of surface finish in nanoscale, high variations due to machine precision, thermal instabilities, and tool vibration impact the stability of process. Previous research efforts have focused on mechanisms of material removal in UPM. However, there is a dire need to leverage advanced sensing for effective data-driven quality control that improves process stability and reduces reworks [9].

1.2.1 In-situ sensing in advanced manufacturing

Advanced sensing provides an unprecedented opportunity to cope with the process complexity and enable in-situ quality control of AM processes. Recent developments in communication and electronics have improved the design and development of low-cost and miniaturized sensors for use in AM settings that are previously not possible. In the state of the art, a variety of in-situ sensors (e.g., infrared sensors, video imaging, pyrometers, and photodiodes) have been used to capture information for advanced manufacturing process monitoring and control.

For instance, infrared camera has been utilized to capture the thermal distribution of AM builds, and provide information on residual stress and microstructures of 3D products. Krauss et al. [10] detected material discontinuities and process deviations by monitoring the temperature distribution of AM layers using an infrared camera in the selective laser melting (SLM) process. Rodriguez et al. [11] developed the in-situ thermography to identify absolute thermal non-uniformity in layer surfaces of AM parts for quality control. In a series of related works, Craeghs et al. [12–14] describe optical-based approaches for monitoring build quality in AM by imaging the thermal behavior at the meltpool. Craeghs et al. were able to detect process defects, such as deformation and overheating [13].

High-resolution cameras with visible wave-length also play an important role in monitoring the quality information of AM layers to identify material discontinuities and process errors. The CIMP-3D at the Penn State developed an in-chamber imaging system with high-definition 36.3 megapixel single-lens reflex (DSLR) 164 AQ4 camera (Nikon D800E) with multiple flash modules [15]. In this context, the use of optical imaging for quality monitoring and control is a novel contribution of this work. Optical imaging cameras are significantly less expensive than their thermal and high-speed counterparts.

1.2.2 Sensor-based quality monitoring and control of advanced manufacturing

In-situ sensing systems bring large amounts of complex structured data that call upon the development of new quality monitoring and control methodologies. In the past few years, sensor-based learning methods for process control have attracted increasing interests. For example, Grobert et al. [16] implemented the support vector machine as a binary classification technique to differentiate two types of build structures, namely, flaw and normal build conditions in powder bed fusion using optical imaging. Francis et al. [17] developed a geometric error compensation framework using a convolutional neural network (CNN) model that predicts distortion for LPBF process. Scime et al. [18] studied an unsupervised learning technique (i.e., K-means) to specify eight different types of anomalies of powder recoating in LPBF process.

However, current investigations are still far from maturity and mainly focused on the sensing system design and utilization with anomaly detection. The practical sensor-based analysis is limited, thus data-driven methodologies for real-time processing parameters optimization, defect detection, quality control are still insufficient. Especially, key shortcomings of the current practices are the lack of effective feature extraction (i.e., management of large amounts of data with the high sampling frequency) as well as the dearth of customized monitoring strategies (i.e., absence of training samples in the presence of one-of-a-kind and highly customized builds). Overcoming these limitations enables capturing the most critical information, quantifying process dynamics, and performing effective quality monitoring and control.

1.3 Research Objectives

My research goal is to develop innovative methodologies using sensing data and for real-time quality monitoring and control in advanced manufacturing systems. Specifically, the objectives of this dissertation include:

1. Studying a hybrid spectral graph theory and multifractal and lacunarity analysis to capture the most informative features for analyzing the process condition that leads to the porosity defect in AM process.

2. Developing an efficient method to investigate the nonlinear and non-homogeneity patterns in image profiles for defects identification and characterization in UPM and AM processes.

3. Designing methodology of deep learning of variant geometry for layerwise image-guided quality control in AM. Our methodology is divided into the following steps: 1) layerwise ROI estimation, 2) freeform geometry analysis by hierarchical dyadic partitioning, 3) spatial characterization, and 4) DNN learning of incipient flaws.

4. Introducing a novel spatiotemporal Gaussian Process to model the evolving dynamics within ROIs of layerwise images for AM process monitoring and control. Also, we design statistical control charts to effectively detect anomalies in layerwise images.

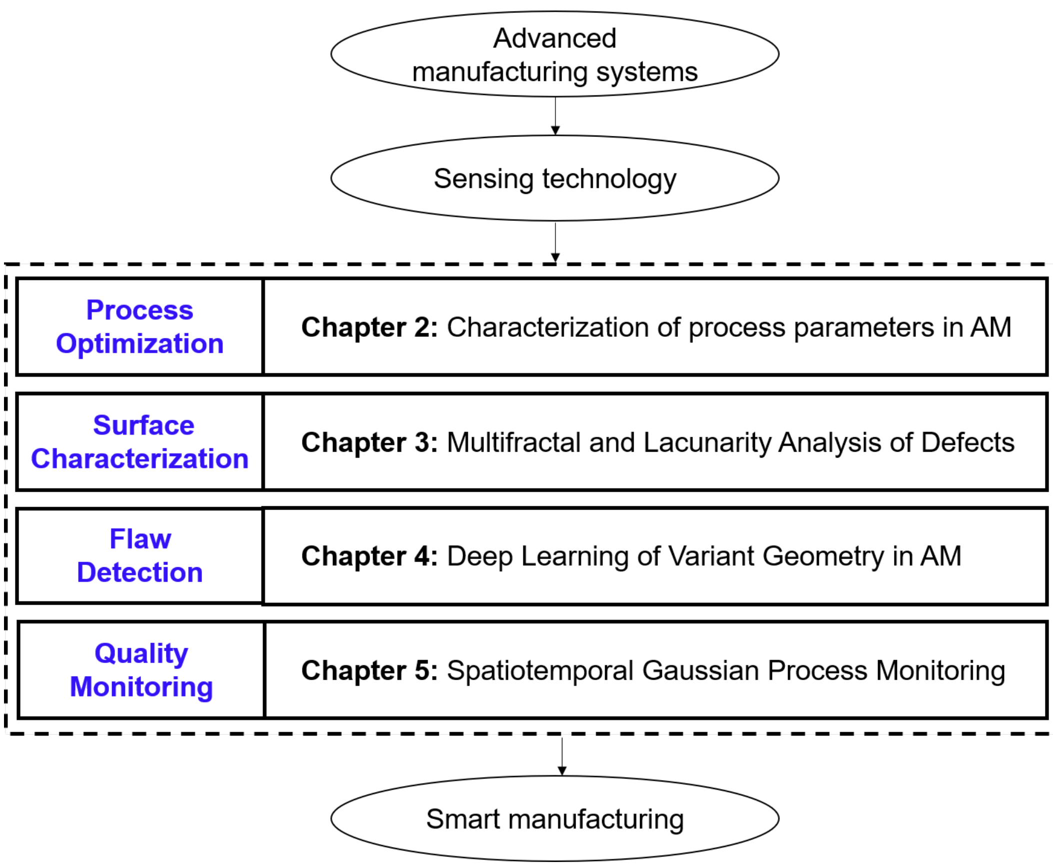

Figure 1.2. The overall structure of proposed research methodologies in this dissertation.

As shown in Figure 1.2, the proposed research will enable and assist in 1) mapping impact of process conditions on quality of build; 2) extracting pertinent information about system dynamics from complex sensing data; 3) designing a new methodology to learn defects from layerwise images with variant geometry; 4) introducing real-time quality monitoring with incorporating spatiotemporal dynamics in AM processes.

1.4 Organization of the Dissertation

The outline of this dissertation is illustrated in Figure 1.2. This dissertation is organized based on multiple manuscripts. Each of chapters 2-5 is written as a research paper (first three published and last paper is under review). The remainder of the dissertation is organized as follows:

In Chapter 2, we present the modeling and analysis of in-process layerwise images in LPBF to investigate the effect of LPBF process conditions on the severity, size, and location of porosity, and further connects the process conditions to sensor signatures. Online visible spectrum images of the part were acquired as they are built using a still camera. These images were analyzed using multifractal and graph-theoretic approaches.

In Chapter 3, we propose the joint multifractal and lacunarity analysis of image profiles in UPM and AM processes for manufacturing quality control. The multifractal spectrum resolves local densities and captures nonhomogeneous variations of image profiles. Lacunarity complements multifractal analysis by characterizing the filling patterns in image profiles. Further, we derive the composite quality index by computing Hotelling T^2 statistics from multifractal and lacunarity features for defect detection and characterization in UPM and AM image profiles.

In Chapter 4, we investigate the CAD file to perform shape-to-image registration and to delineate the ROIs in layerwise images. Next, a hierarchical dyadic partitioning methodology is developed to split layer-to-layer ROIs into subregions with the same number of pixels to provide freeform geometry analysis. Then, we propose a semiparametric model to characterize the complex spatial patterns in each customized subregion and boost the computational speed. Finally, a DNN model is designed to learn variant geometry in layerwise imaging profiles and detect fine-grained information of flaws.

In Chapter 5, we address the challenge of spatiotemporal data. We develop the spatiotemporal Gaussian process for high-dimensional AM quality monitoring. This model not only captures the standard layerwise AM mages in ROIs but also incorporates layer to layer spatial and temporal deviation to improve the performance of quality monitoring.

In the end, Chapter 6 concludes the dissertation and summarizes the contributions. Future research directions are also discussed in this chapter.

Chapter 2 Characterization of Process Conditions in AM

Process Mapping and In-Process Monitoring of Porosity in Laser Powder Bed Fusion using Layerwise Optical Imaging

Abstract

The goal of this work is to understand the effect of process conditions on part porosity in LPBF process, and subsequently, to detect the onset of process conditions that lead to porosity from in-process sensor data. In pursuit of this goal, the objectives of this work are two-fold: (1) quantify the count (number), size and location of pores as a function of three LPBF process parameters, namely, the hatch spacing (H), laser velocity (V), and laser power (P); and (2) monitor and identify process conditions that are liable to cause porosity through analysis of in-process layer-by-layer optical images of the build invoking multifractal and spectral graph theoretic features. These objectives are important because porosity has a significant impact on the functional integrity of LPBF parts, such as fatigue life. Furthermore, linking process conditions to defects via sensor signatures is the first-step towards in-process quality assurance in LPBF. To achieve the first objective, titanium alloy (Ti-6Al-4V) test cylinders of 10 mm diameter $\times 25$ mm height were built under differing H, V, and P settings on a commercial LPBF machine (EOS M280). The effect of these process parameters on count, size and location of pores

was quantified based on X-ray computed tomography (XCT) images. To achieve the second objective, layerwise optical images of the powder bed were acquired as the parts were being built. Spectral graph theoretic and multifractal features were extracted from the layer-by-layer images for each test part. Subsequently, these features were linked to the process parameters using machine learning approaches. Through these image-based features, process conditions under which the parts were built was identified with the statistical fidelity over 80% (F-score).

2.1 Introduction

2.1.1 Background

Powder bed fusion (PBF) refers to a family of AM processes in which thermal energy selectively fuses regions of a powder bed [19]. Figure 2.1 shows the schematic of the PBF process. A layer of powder material is spread across a build plate. Certain areas of this layer of powder are then selectively melted (fused) with an energy source, such as a laser or electron beam. The bed is lowered and another layer of powder is spread over it and melted [20]. This cycle continues until the part is built. The PBF process embodied in Figure 2.1 depicts a laser power source for melting the material, accordingly, the convention is to refer to the process as LPBF.

A galvanic mirror scans the laser across the powder bed. The laser is focused on the bed with a spot size on the order of $50\,\mu$m - $100\,\mu$m in diameter, the laser power is typically maintained in the range of 200 W to 400 W, the linear scan velocity of the laser is varied in the 200 mm/s to 2000 mm/s range, and the distance between each stripe of the laser, called the hatch spacing, is maintained in the range of $100\,\mu$m to $200\,\mu$m. The distance through which the bed is lowered is termed the layer height and is typically in the range of 30 to 50 μm [20]. Close to 50 other parameters are involved in the melting and solidification process in LPBF [21].

2.1.2 Motivation

The ability of LPBF to produce intricate geometry parts from hard-to-process materials, such as cobalt-chrome and nickel-based super alloys has been conclusively

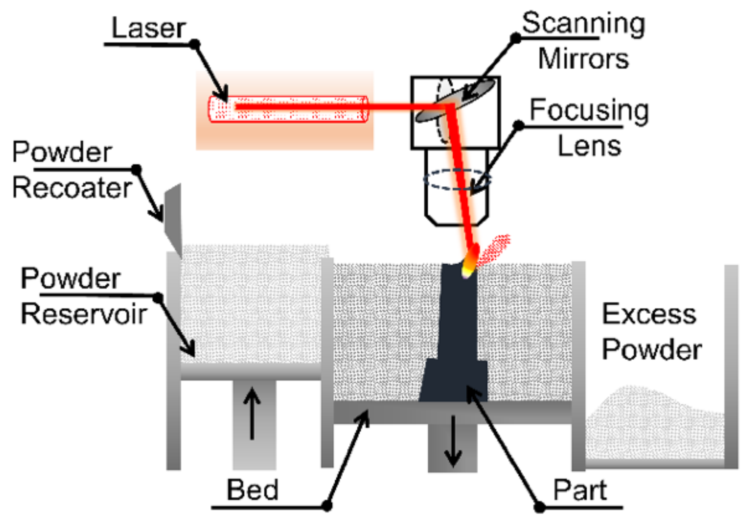

Figure 2.1. The schematic diagram of the LPBF process.

demonstrated for a variety of demanding applications ranging from biomedical to aerospace [22, 23]. Process repeatability and product quality, however, remain imposing barriers towards scaling LPBF to production environments [24]. Given the layer-by-layer nature of the process, a defect in a layer, if not averted, will be permanently sealed in by subsequent layers. These trapped defects adversely affect key functional properties of the part, such as its fatigue life and strength [25, 26].

A major gap in the current research lies in the lack of quantitative models to correlate the effect of process conditions on specific defects, such as porosity via the data acquired from in-situ sensors. Addressing this gap is the first-step towards in-process quality assurance in LPBF. Therefore, there is an urgent need to: 1) understand and quantify the effect of LPBF process conditions on defects, and 2) institute in-process sensing and monitoring to capture the onset of defects.

The following types of LPBF defects have attracted the most attention: porosity, surface finish, cracking, layer delamination, and geometric distortion. These defects are tracked to the following four root causes [27, 28]:

- Poor part design, such as inadequately supported features [29].
- Machine and environmental factors, such as poor calibration of the bed and optics.
- Inconsistencies in the input powder material, such as contamination and

deviations in particle distributions.

- Improper process parameter settings, for example, inordinately high laser power causes vaporization of the material leading to keyhole porosity, while insufficient laser power prevents powder particles from fusing together leading to large acicular pores [30, 31]. This work specifically focuses on characterizing and detecting porosity in-situ due to the improper selection of process parameters.

2.1.3 Objectives

The goal of this work is to quantify the effect of process conditions on part porosity in the LPBF process, and subsequently, detect the onset of porosity due to deviation in process conditions based on in-process sensor data. An example of such a possible deviation is the occlusion of the optics due to vaporization of the material during melting and its eventual condensation on the focusing lens. The gradual coating of residue on the laser will lead to loss of laser focus, and hence reduce the power delivered to the substrate without the knowledge of the operator. In extreme instances, because the residue deposited on the lens absorbs a significant portion of the incident energy, damage to the lens and optical train can occur [32].

In pursuit of this goal, the objectives of this work are two-fold:

1. Quantify the effect of three LPBF process parameters, namely, laser power (P), hatch spacing (H), and velocity (V) on the size, count, and location of pores using X-ray computed tomography (XCT) scan data of the part.

2. Monitor and discriminate process deviations that are liable to cause porosity using in-process optical images of the powder bed invoking multifractal and spectral graph theoretic analysis.

The first objective is realized by simultaneously building nine titanium alloy cylinders on a commercial LPBF machine (EOS M280) at varying P, H, and V conditions, and quantifying their effect on the pore spatial distribution count, size and location are quantified using XCT images.

The second objective is achieved by acquiring layer-by-layer optical images of the parts while they are being built, and then extracting statistical, multifractal and spectral graph theoretic features from these images. These features are subsequently used in various classification approaches such as neural networks to ascertain their ability to isolate process conditions that are liable to produce parts with severe pores.

The rest of this chapter is structured as follows. A brief review of the literature focusing on porosity and in-process sensing in LPBF is presented in Section 2.2; Section 2.3 describes the experimental conditions and layer-by-layer acquisition of part images; Section 2.4 explains the spectral graph theory and multifractal analysis of in-process image data for feature extraction and process modeling; and conclusions and avenues for future work are presented in Section 2.5.

2.2 Review of the Relevant Literature

The literature concerning the reasons and mechanisms of porosity formation and in-process sensing are summarized in Section 2.2.1 and Section 2.2.2, respectively.

2.2.1 Effect of LPBF process parameters on porosity

Of the various multi-scale defects in LPBF, porosity and its attendant causes have garnered the most attention [28, 33–35]. According to Rao et al., voids or pores are empty spaces in a material and porosity is a measure of the volume occupied by these empty spaces over the total part volume [36]. Mechanical properties such as strength and fatigue performance LPBF-processed parts are severely affected by porosity; pores cause high-stress concentration, which in turn results in crack formation [37–40].

The formation of porosity is closely tied to and governed by the thermal phenomena at the meltpool-level [41]. Gong et al. have identified four distinctive regimes of melting contingent on the laser power (P) and velocity (V) process parameter settings. These regimes are demarcated as Zone I (fully dense); Zone II (over melting); Zone III (incomplete melting); and Overheating Zone (OH) [38, 42]. Visualizing a process map of laser power plotted on the ordinate axis, and the velocity on the abscissa, the region along the 45 degree slope falls under Zone I, also termed as the conduction mode. In this region, parts with least porosity-related defects were obtained. Zone II is to the left of Zone I, herein the laser power is higher for a given velocity compared to Zone I. This region is home to the so-called keyhole mode melting, where, as experimentally and theoretically elucidated by King et al. material vaporization occurs due to excessive energy input [43]. Zone III is to the right of Zone I, and is characterized by relatively higher velocity for a given power setting compared to Zone I. In this zone (Zone III), there is inadequate energy for the material to completely fuse.

While Gong et al. found that parts can be made in either of Zones I, II, and III, however, parts could not be built in the OH Zone, which is mapped to the left of Zone II, because the layers tend to deform to such a high degree during the build that the deposition of subsequent layers is impeded. Gong et al. report that in their experiments the recoater jams occurred in the OH zone due to contact with the part [38, 42]. Similar process mapping results for other AM processes, such as powder and wire-fed directed energy deposition, and electron beam powder bed fusion are reported by Beuth et al. [44–46]. Within the three melting zones, Zone I-III, the mechanism, and nature of pores formed are distinctive.

Lack of fusion porosity occurs in Zone III because the laser energy supplied is insufficient to fuse the adjacent tracks, and the current and previously deposited layers. Lack of fusion porosity results in the formation of large acicular pores of size in the range of 30 μm - 100 μm [22]. From an experimental perspective for Titanium alloy Ti-6Al-4V, Gong et al. correlate areal energy density $E_A = \frac{P}{(H \times V)}$ J/mm^2 with porosity and observed the onset of lack of fusion porosity typically occurs for $E_A < 1.1$ (approximately). Considering also the layer thickness T as a factor (maintained constant at 30 μm the equivalent threshold for volumetric energy density $E_V = \frac{P}{(H \times V \times T)}$ is ≈ 36 J/mm^3.

Keyhole-collapse porosity in Zone II occurs due to vaporization of powder material [20–22]. King et al. elucidate through theoretical simulations and experimental studies that when the energy supplied by the laser is inordinately high, the laser melts through several layers of the powder vaporizing material in its path. The vapor cavity eventually collapses thus forming pores deep within the meltpool [43]. The pores resulting from operating in the keyhole melting mode are uniform and circular in shape and are typically on the scale of 10-20 μm [30]. Gong et al.'s studies indicate that as the energy density in the processing of Ti-6Al-4V increases beyond a threshold value (typically $E_A > 2, E_V > 66$) the process enters the keyhole melting mode [38, 42].

To avoid oxidation of the powder, the LPBF process is carried out in a chamber filled with inert gas (usually argon or nitrogen) depending upon the material to be processed. The argon or nitrogen gas may get trapped in the powder and lead to the formation of gas pores [47]. Additionally, gas pores are also formed when bubbles are trapped in the meltpool during the solidification process [36]. Gong et al. also explain the formation of voids and pits due to the ejection of powder material as spatter on account of the thermal energy [38, 42]. The ejected particles may settle within the boundary of the part, and on cooling may adhere to the surface of the powder bed. Further, as the next layer is being deposited, the adhered particles may subsequently be removed by the recoater leaving a pit or void in its place. Lastly, lower melting impurities and constituents may vaporize given a sufficiently high energy density (and not due to keyhole collapse) leaving voids in the part [48]. Such types of pores are not restricted to one type melting zone and are stochastic in nature.

From the extensive experimental work of Gong et al. it is surmised that for Ti-6Al-4V material, the conduction melting mode typically occurs in the range of $1.1 < E_A < 2$ J/mm^2; or equivalently $36 < E_V < 66$ J/mm^3. Aboulkhair et al. [30, 37] and Stucker et al. [49–51] report extensive process optimization studies related to porosity in LPBF with conclusions in line with findings by Beuth et al [44–46]. While most of the existing process maps relate the effect of areal or volumetric energy density to porosity with the aid of XCT, a conspicuous gap remains in relating pore size, density and location simultaneously with E_A. This work addresses the foregoing gap through objective 1.

In closing this section, we note that the process zones and concomitant types of porosity reported in the literature are contingent on the presumptions of stable process operation and that the part geometry and its location on the build plate have negligible effect.

2.2.2 Sensing and monitoring in LPBF

Comprehensive review articles for in-process sensing are available in Refs. [27, 52–55]. Significant research in process sensing and control for metal AM processes is being done in academe and national laboratories [15, 56–60]. Nassar et al. experimented with imaging of the LPBF powder bed under various illumination conditions

[1, 15, 60]. The resulting layer data was analyzed, and defects, such as voids caused by improper raking of the powder across the bed were identified. Lane et al. at NIST integrated an LPBF machine (EOS M270) with thermal and high-speed cameras, and a photodetector [56]. NIST and Edison Welding Institute (EWI) are currently building a customized LPBF testbed instrumented with multiple sensors [59, 61]. A large body of work in sensing and monitoring in LPBF is reported by the Kruth group [12–14] and Witt group [62–65] in Europe. Recent breakthroughs with in-situ X-ray imaging of the LPBF process has been reported by scientists at Lawrence Livermore National Laboratories [66].

To detect evolving process anomalies researchers have sought to incorporate sensing techniques such as vibration, charge-coupled device (CCD) video imaging, infrared and ultraviolet imaging, pyrometers, photodiodes, ultrasonic wave generators in AM machines [10, 62, 67–72]. An early example was presented by Melwin et al. [73], who used a video-micrography apparatus bearing band pass and polarizing filters for observing the meltpool in polymer LPBF.

In a series of related works, Craeghs et al. [12–14] describe optical-based approaches for monitoring build quality in PBF by imaging the thermal behavior at the meltpool. Craeghs et al. were able to detect process defects, such as deformation and overheating using their optical system [13]. Bartkowiak [74] describes a PBF apparatus integrated with a spectrometer for in situ measurements of the layer melt characteristics, such as emissivity. Other researchers, e.g., Chivel et al. [75], and Jacobsmuhlen et al. [62] have also developed optical imaging systems for process monitoring in AM [75]. In a recent work, Rieder et al. [69] used an ultrasonic sensing system for tracking build status in PBF. A broadband ultrasonic sensor mounted on the underside of the build plate is used to detect voids, akin to acoustic microscopy.

Craeghs et al. [13, 76, 77] report that the amplitude of the photodiode signal is correlated with the melt-pool area and the melt-pool temperature. They subsequently use this information to identify process failures, such as detection of deformation due to thermal stresses and overheating at overhang structures, in each build layer. Further, they developed a feedback control sensor based on optical images. Chivel and Smurov [75] use two different wavelengths and selected temperature profiles to extract information of the bed temperature distribution, and the size of the meltpool for process monitoring.

Regarding the fidelity of the different sensing approaches for detecting defects specific to PBF AM processes, the viability of thermal imaging and optical spectroscopy-based techniques has been demonstrated in the literature. Recent work done by researchers at NIST aims to comprehensively capture the effect of meltpool shape and thermal gradients to defects. From the meltpool monitoring vista, a fast response thermal camera with a high framerate (> 1000 frames/second) and resolution in the micrometer range is typically used to circumvent blurring effects [78]. In recent work by EWI researchers the meltpool-level thermal camera is coupled with another thermal camera that monitors the heat flux over the entire bed to detect large macro-scale defects, such as warping [61]. However, such high-fidelity thermal cameras are exceeding expensive, and moreover, they are appropriate for capturing thermal trends rather than the exact temperature of the target because the emissivity of the meltpool remains to be established. Dual color pyrometers can be used to circumvent the lack of emissivity information.

A far less expensive alternative to thermal imaging for detection of micrometer-level defects is through the use of photodetectors and spectrometers. Nassar et al. in a series of articles demonstrate the use of such optical emission spectroscopy-based sensing [58, 79, 80]. The key idea is to measure the intensity (amplitude) of the line-to-continuum ratio emission spectra of the material being processed and relate the readings to part defects. For this purpose, two photodetectors are coupled through a 50:50 beam splitter, and focused upon the entire bed area. Each of the photodetectors is fitted with an optical bandpass filter that captures light corresponding to the emission spectra of a particular element in the alloy being processed. For instance, for detecting anomalies in LPBF of Inconel 718, Nassar et al. used a 520 ± 5 nm and 530 ± 5 nm optical bandpass filters corresponding to the continuum and line spectra, respectively, of Cr I emissions [79].

Instead of using two photodetectors to capture formation of porosity, Montazeri et al. in two articles published in this journal, have used a single photodetector to capture the onset of material contamination, and also to distinguish the process signatures emanating for different feature geometries, such as overhang-related features [48, 81]. While photodetectors and spectrometers present a cost advantage over thermal imaging, and are capable of sampling rates nearing 1 MHz, their main drawback is that the output is in terms of a time series or frequency spectrum which have far limited information compared to thermal imaging.

In this context, the use of optical imaging for detection of conditions liable to produce porosity is a novel contribution of this work. Optical imaging cameras are significantly less expensive than their thermal and high-speed counterparts. However, the challenge of capturing pores directly from the layerwise optical images, as opposed, to the anomalous process conditions has not yet been attempted. In closure, we note that Abdelrahman et al. [1] have used optical imaging data to capture the large-scale ($> 100\ \mu$m) defects which were deliberately introduced during the build.

The main drawback in most of these studies is that they do not connect practical process conditions to defects, but rather focus on artificially inducing flaws by way of catastrophic process anomalies. Furthermore, the analytical techniques rely on classical time-series signal processing techniques, which may not be effective in capturing subtle defects. Recent progress to overcome this limitation is reported by the Clare group at Nottingham University who have used spatially resolved acoustic spectroscopy to detect porosity ex situ in LPBF, wherein the amplitude of a surface acoustic wave generated by laser is correlated with the location and severity of porosity at different laser power settings [82, 83]. The current work addresses this extant gap through objective 2.

2.3 Experimental Setup and Data Acquisition

Experiments were conducted on an EOS M280 LPBF machine. The input material was a Titanium alloy, ASTM B348 Grade 23 Ti-6Al-4V powder material whose particle size ranges from 14 μm to 45 μm. The parts analyzed in this study are cylinders which were printed by varying the hatch spacing (H), scan velocity (V) and laser power (P). The cylinders are 25 mm in length and 10 mm in diameter shows the seven process parameter settings which were used to print these cylinders. The nominal settings are labeled as $H0 = 0.12$ mm, $V0 = 1250$ mm/s, and $P0 = 340$ W. The layer height is maintained is constant at $T = 60\ \mu$m. Hatch spacing and laser print velocity are increased by 25% and 50%, and laser powder has been decreased by 25% and 50% from their nominal settings. The three process settings are aggregated in terms of the areal energy density applied for melting called the Andrew number: $E_A = \frac{P}{H \times V}$ J/mm^2 or the volumetric energy density $E_V = \frac{P}{H \times V \times T}$ J/mm^3. Comparing the E_V values reported in Table 2.1 with the experimental results of Gong et al. [38,42], we note that barring the nominal settings, which is set in the conduction regime (Zone I), all other experimental treatment combinations fall within the lack of fusion (Zone III) regime where acicular pores are expected ($E_V < 36$).

A digital single-lens reflex camera (DSLR, Nikon D800E) along with multiple flash-lamps placed inside the build chamber is used to capture the layer-by-layer powder bed images. Images are captured at two instances in every layer, namely, post laser scan and post re-coat. The camera shutter is controlled by a proximity sensor that registers the location of the recoater blade. Five images of the powder bed images are captured under bright-field and dark-field flash settings. The layout of the camera and flash-lamp location are shown in Figure 2.2, and the representative images under the five light schemes are shown in Figure 2.3. In this work, images from the bright-field light scheme in Figure 2.3(a) are analyzed. Details of the experimental setup are available in Ref. [1].

Table 2.1. The combination of power (P), hatch spacing (H), scan velocity (V), and layer height (T) process conditions used for making the titanium alloy parts.

Process Condition ($P, H, V, T = 0.060$) [W, mm, mm/s, mm]		E_A [J.mm^{-2}]	E_V [J.mm^{-3}]
P0, H0, V0	(340, 0.12, 1250,0.06)	2.27	37.8
P -25%, H0, V0	(255, 0.12, 1250,0.06)	1.70	28.3
P-50%, H0, V0	(170, 0.12, 1250,0.06)	1.13	18.8
P0, H +25%, V0	(170, 0.15, 1250,0.06)	1.81	30.1
P0, H +50%, V0	(170, 0.18, 1250,0.06)	1.51	25.1
P0, H0, V +25%	(170, 0.12, 1562,0.06)	1.81	30.1
P0, H0, V +50%	(170, 0.12, 1875,0.06)	1.51	25.1

2.4 Methodology and Results

As shown in Figure 2.4, the LPBF process data is analyzed in two phases, namely, (1) offline analysis of XCT data in Section 2.4.1; and (2) analysis of in-situ images of the powder bed in Section 2.4.2.

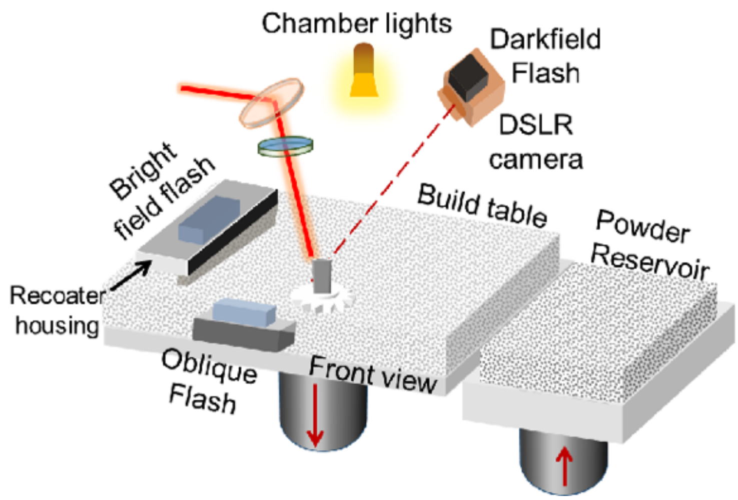

Figure 2.2. Schematic diagram of the location of flash-lamps and camera used to capture in-situ powder bed images [1]

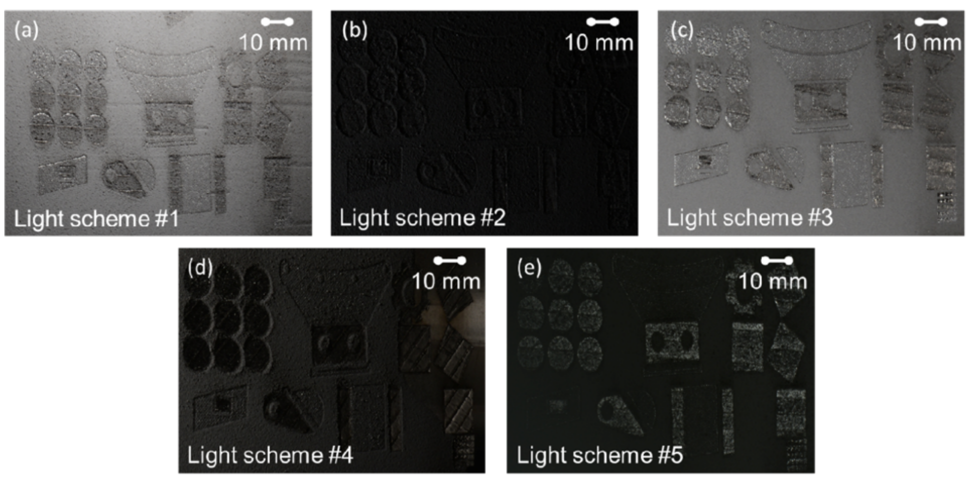

Figure 2.3. Cropped image of the powder bed in different light schemes.

2.4.1 Phase 1: offline analysis of porosity

This section aims to analyze the effect of hatch spacing (H), laser velocity (V), and laser power (P) on the count, size, and location of pores. Representative XCT images of parts under different P, H and V conditions are shown in Figure 2.5. A visual inspection of the XCT scans shows that the size and number (count) of the pore is inversely proportional to the areal energy density (E_A).

As the areal energy density (Andrew's number, E_A) is reduced, we observed that the size and number of the pores become larger. However we caution that,

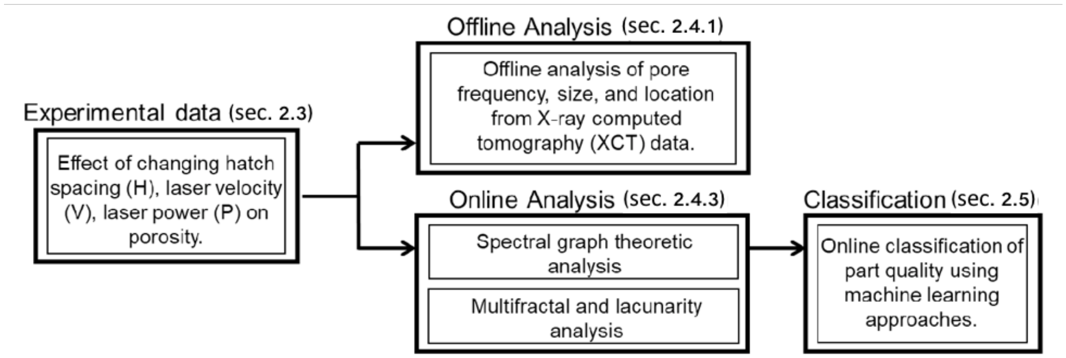

Figure 2.4. An overview of the methodology for analysis of offline computed tomography data, and in-situ images of powder bed fusion process.

although, the critical process parameters, such as laser power (P, W), hatch spacing (H, mm), scan velocity (V, mm/s), and layer height (mm) can be optimized for certain part geometries, and aggregated in terms of the global volumetric energy density (E_A) pores can still occur. This is because, (E_A) does not account for the thermal aspects in the part (heat flux), which is contingent on the part geometry, orientation, and its location on the build plate. For instance, parts in the far edge of the build platen (near the end of the recoater action) may suffer from insufficient powder feed (powder shorting), likewise, the laser spot size is liable to change as the laser tends to defocus on the outer edge of the build platen leading to lack-of-fusion related porosity.

Furthermore, there is the possibility of a complex, nonlinear interaction between P, V, and H which remains as yet undiscovered and therefore not captured in the relationship representing the areal energy density. For instance, in the equation for E_A, all terms are assumed to be equal in weight, i.e., the exponent P, V, and H is unity (=1) and therefore the relationship between E_A and the process parameters is implicitly assumed to be a simple linear relationship. The following inference is made based on Figure 2.5. For instance, while the severity of pores is influenced by all three process parameters. However, laser power (P) seems to have an inordinately high effect. This observation is further quantified by extracting count, size and location attributes by analyzing the XCT scan images through the steps shown in Figure 2.6.

- Figure 2.6(a) – XCT scans for 30 randomly chosen cross-sectional areas are analyzed.

- Figure 2.6(b) and (c) – The XCT scan images are binarized based on a heuristically determined threshold. Some information is inevitably compromised during the binarization process. A complement of the binary image is taken to return a black background, which makes computation easier as the image matrix becomes sparse.

- Figure 2.6(d) – To reduce noise induced due to binarization the nearest neighborhood approach is used [84]. We note that while it is customary to refer to voxels in the context of XCT, because the images are converted to binary images (binarized), we revert to using the term pixel. In this procedure, a binarized XCT pixel is labeled as a defect only if it is connected to the 8-nearest pixels. In other words, if the 8 nearest neighboring pixels of a particular pixel are also bright (i.e., 1), then the pixel is deemed to represent part of a defect.

Next, the pore count, size and location are extracted as follows:

- Pore count - The number of 8-connected binarized XCT pixel over a layer translates to the pore count.

- Size of pores - The size of a pore is grouped into one of 5 classes contingent on its radius. Each pore is considered as an annular structure on the noise reduced image, and then, the number of pixels within each annulus is calculated. Depending on the number of pixels in the annulus, the pores are classified into various radii, namely 1-5 pixel radii. A radius of one-pixel unit equates to a pore radius of 16 μm on the part.

- Pore Location - The pore location is determined by segmenting the XCT scan image into 5 concentric areas as shown in 2.7. The number of pores in each 1 mm thick segment of the XCT scan image is then counted. This establishes the distance of the pores from the center of the cylinder.

(a) *Effect of process parameters on count and size of pores*

Analysis of the XCT scan images shows that decrease in the areal energy density (E_A) leads to an increase in the count (number of pores) and size of pores. This effect of laser power (P), hatch spacing (H), and laser print

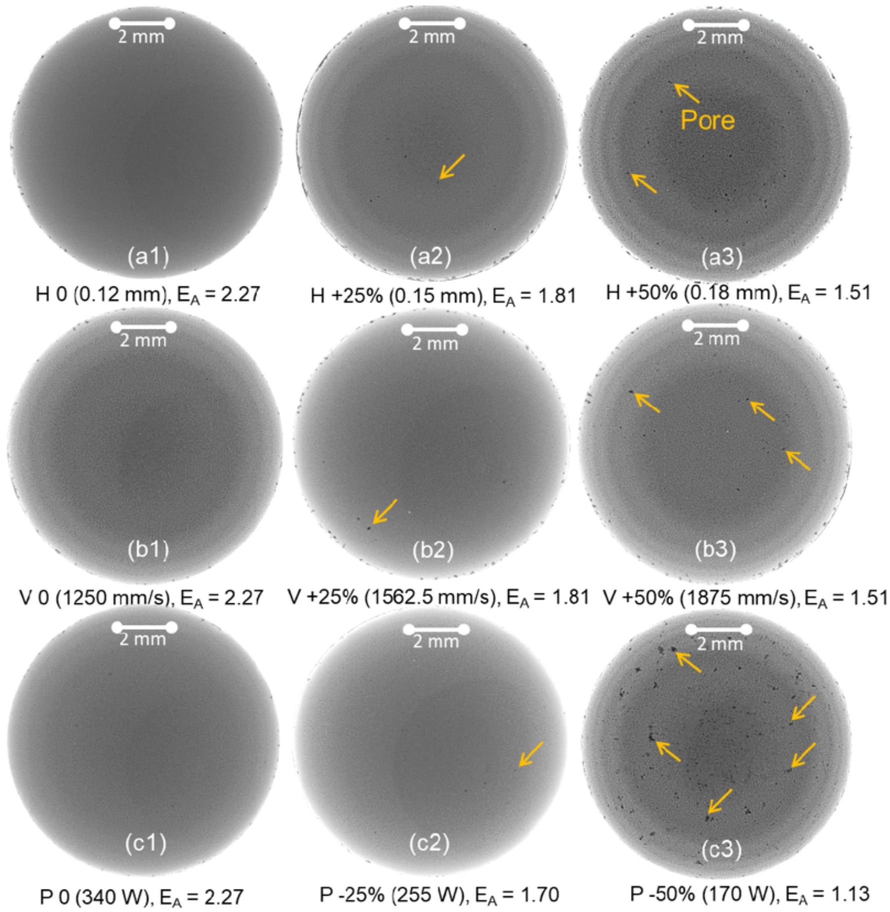

Figure 2.5. Effect of process conditions on the parts as seen in XCT scan images. Pore count increases as process conditions drift from nominal conditions. Highest number of pores are seen in the part printed at P -50% (c3).

velocity (V) on pore count and size are exemplified in Figure 2.8 from which the following inferences are drawn. In Figure 2.8, the x-axis is the pore size, and the y-axis is the mean count (or number) of the pore observed on 30 randomly selected slices of the XCT scan. These results are also detailed in Table 2.2, which reports the mean number of pores, rounded to the nearest integer, along with the standard deviation for 30 randomly chosen layers.

(a) Referring to Figure 2.8(a), the pore distribution in terms of count vs. pore size is plotted for different levels of laser power (P). The decrease in laser power by 50% (170 W) leads to almost a 100-fold increase in the number of pores. Further, parts produced under P -50% (170 W) have pores ranging from 1 pixel to 4 pixels in size, i.e., 16 μm to 64 μm,

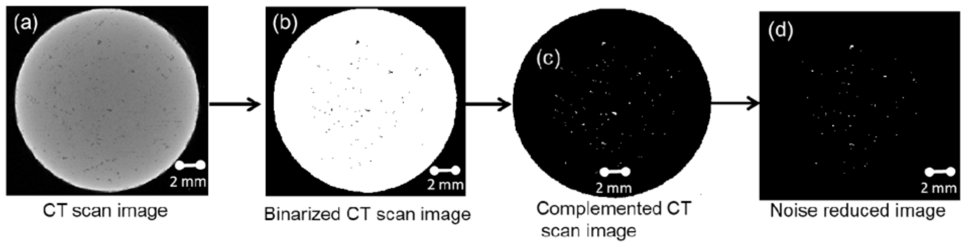

Figure 2.6. An overview of the image processing methodology used to analyze the XCT scan images. (a) XCT scan image of part printed with P -50%, (b) binarization of the XCT scan image of the part, (c) complemented binary image of the XCT scan image, and (d) noise reduced XCT scan image which is used for the spatial distribution analysis.

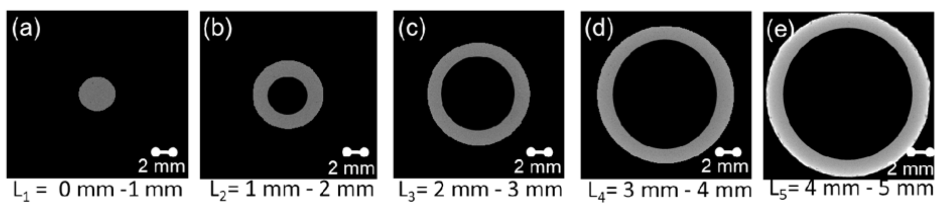

Figure 2.7. An example of the procedure followed to divide XCT scan image of a part into concentric segments. (a) First segment 0 mm – 1 mm of the XCT scan image (L1), i.e., the segment that encompasses the center of the XCT scan image, (b) second segment 1 mm – 2 mm of the XCT scan image (L2), (c) third segment 2 mm – 3 mm of the XCT scan image (L3), (d) fourth segment 3 mm – 4 mm of the XCT scan image (L4), and (e) last segment 4 mm – 5 mm of the XCT scan image (L5), i.e., the segment which is farthest from the center of the XCT scan image.

whereas parts produced under nominal power (P0= 340 W) and P -25% (270 W) have pores of radius 2 pixels ($\sim$ 32 μm at most).

(b) Referring to Figure 2.8(b), increasing the hatch spacing (H) leads to an increase in both the count and size of pores. The magnitude of the effect of laser hatch spacing is significantly smaller than that of laser power. In case of varying hatch spacing (Figure 2.8(b)), the highest number of pores are seen in the cylinder which is printed with H +50%, i.e., 0.18 mm hatch spacing. From Figure 2.8(b), for all the three levels of hatch spacing, the largest pore radius observed is 2 pixels.

(c) Referring to Figure 2.8(c), akin to hatch spacing, increase in laser print velocity (V) leads to increase in count and size of pores. The largest pore size of radius 3 pixels ($\sim$48 μm was recorded in the cylinder printed with V +50% (1875 mm/s). The effect of velocity on porosity is least consequential of the three factors studied in this work.

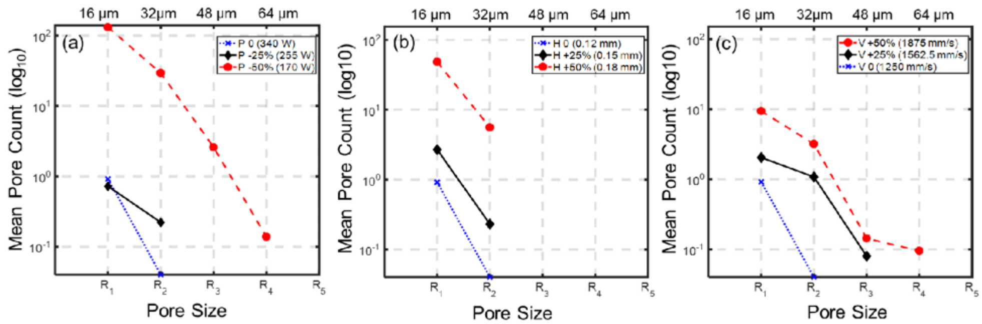

Figure 2.8. Count of pores vs. pore size in varying process conditions. (a) In P -50% printing condition highest number of pores are seen of size R1 (16 μm), and in P0 and P -25% printing condition, very few pores of size R1 (16 μm) are seen. (b) In parts printed with varying hatch spacing only pores of size R1 (16 μm) and R2 (32 μm) are seen, and the highest number of pores is seen in H +50% printing condition. (c) In comparison with other printing conditions, the lowest number of pores is seen in parts printed with varying velocity. Pores of size R1 (16 μm) are highest in number in V0, V +25%, and V +50% printing conditions.

Table 2.2. Mean count of pores and its standard deviation (in brackets) of various sizes in the XCT scan image slice in various printing conditions obtained from 30 randomly sampled layers.

	Mean count of pores						
Size	H0, V0, P0 (Nominal condition) (0.12 mm, 1250 mm/s, 340 W)	H + 25% (0.15 mm)	H + 55% (0.18 mm)	V + 25% (1562.5 mm/s)	V + 50% (1875 mm/s)	P -25% (255 W)	P - 50% (170 W)
R1 $\sim$ 16 μm	1(1)	3(2)	42(22)	3(2)	10(5)	1(1)	132(31)
R2 $\sim$ 32 μm	1(1)	1(1)	6(4)	2(2)	4(3)	1(1)	30(12)
R3 $\sim$ 48 μm	0	0	0	1(1)	1(1)	0	3(2)
R4 $\sim$ 64 μm	0	0	0	0	1(1)	0	1(1)

(b) *Effect of process parameters on the location of pores*

The location of pores in the test cylinders is determined by segmenting the XCT scan image of a cylinder into 5 concentric parts as described previously in the context of Figure 2.7. This establishes the distance of the pores from the center of the cylinder. The mean and standard deviation of pores in each segment of the part for 30 randomly chosen layers are reported in Table 2.3 and depicted in Figure 2.9, from which the following inferences are drawn:

- Referring to Figure 2.9(a), it is evident that as the laser power decreases, more number of pores are recorded in the L_2 (1 - 2 mm) to L_4 (3 - 4 mm) segment, of the cylinder. Figure 2.9(a) further reveals that the cylinder printed with nominal laser power (340 W) has most number of pores in the first two annular segments of length L_1 (0 - 1 mm) and L_2 (1 - 2 mm), which indicates that the pores are located close to the center. This trend is also observed in the cylinder printed with P -25% laser power (270 W). In contrast, the cylinder printed with -50% laser power has most number of pores in the third segment (2 - 3 mm).
- Referring to Figure 2.9(b) and (c), in cylinders printed with varying hatch spacing (H) and laser print velocity (V), respectively it is observed that parts produced at +50% hatch spacing (0.18 mm) and laser print velocity 1875 mm/s) have the highest number of pores at the radial distance with L_3 (2 - 3 mm). Pores in the cylinders printed with +25% and nominal hatch spacing and laser print velocity are mainly located in the first two segments 0 - 1 mm and 1 - 2 mm.

The sharp drop in porosity in L_5 is likely due to the reason that the external boundary of the part is scanned with increased E_A after the rest of the part (post-contour melting). The added heat at the periphery mitigates porosity in L_5. Further, the concentration of heat in the core of the part may explain the reduced porosity towards the center (L_1). Lastly, the effect of thresholding to convert may lead to a loss of information, this last reason can be largely discounted in the light of Figure 2.6 (a and d), wherein pores in the boundaries are captured appreciably.

2.4.2 Phase 2: analysis of online data of LPBF process

This section aims to link the process conditions to the layer-by-layer images of the parts as they are melted. This will allow detection of process drifts in their early stages. For this purpose, two methods are proposed, the first based on spectral graph theory, and the second using multifractal and lacunarity analysis.

(a) *Application of spectral graph theory for part image analysis*

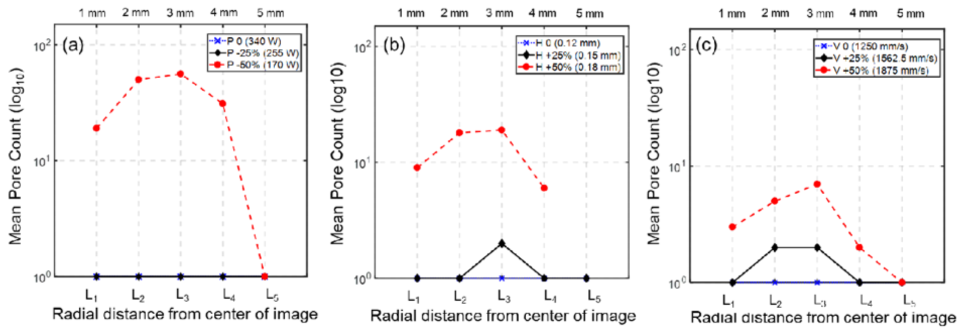

Figure 2.9. Mean pore count vs. radius from center of image at varying process conditions. (a) Parts printed with laser power of P -50% have highest number of pores in the third segment ($L3$ = 2-3 mm) of the XCT scan image. Parts printed with P 0 (nominal condition), and P -25% have pores located in second segment ($L2$ = 1-2 mm) of the XCT scan image. (b) In parts printed with varying hatch spacing highest number of pores are seen in the third segment ($L3$ = 2-3 mm) of the XCT scan image in all conditions. (c) In parts printed with varying velocity highest number of pores are seen in V +50% in the third segment ($L3$ = 2-3 mm), and in V0 and V +25% conditions, highest number of pores are seen in the second segment ($L2$ = 1-2 mm) of the XCT scan images.

Table 2.3. Mean counts of pores and its standard deviation (in brackets) at various locations of the XCT scan image in various printing conditions.

	Mean count of pores						
Radial distance from center of image	H0, V0, P0 (Nominal condition) (0.12 mm, 1250 mm/s, 340 W)	H + 25% (0.15 mm)	H + 55% (0.18 mm)	V + 25% (1562.5 mm/s)	V + 50% (1875 mm/s)	P +25% (255 W)	P + 50% (340 W)
L_1 = 0-1 mm	1(1)	1(1)	9(6)	1(2)	3(3)	1(1)	19(9)
L_2 = 1-2 mm	1(1)	1(1)	18(8)	2(2)	5(4)	1(1)	50(22)
L_3 = 2-3 mm	1(1)	2(1)	19(10)	2(2)	7(5)	1(1)	56(22)
L_4 = 3-4 mm	1(1)	1(1)	6(4)	1(1)	2(2)	1(1)	31(13)
L_5 = 4-5 mm	1(1)	1(1)	0	1(1)	1(1)	1(1)	1(2)

Spectral graph theoretic Laplacian eigenvalues extracted from online images are used to identify the process conditions under which a part is produced. The approach has the following two steps.

Step 1: *Representing the image of each part as a graph.*

A layer-wise image obtained from the DSLR camera for a laser sintered cylinder layer with $M \times N$ pixels can be represented by a matrix $\boldsymbol{X}^{M\times N}$. As shown in Figure 2.10, each row of the matrix X is considered as a row vector and it represents a node or vertex (V) of an undirected graph which is denoted as $G \equiv (V, E)$, where E is the edges in the graph [85]. The M row vectors of the matrix are represented as α_K, $K = \{1, 2, ..., M\}$.

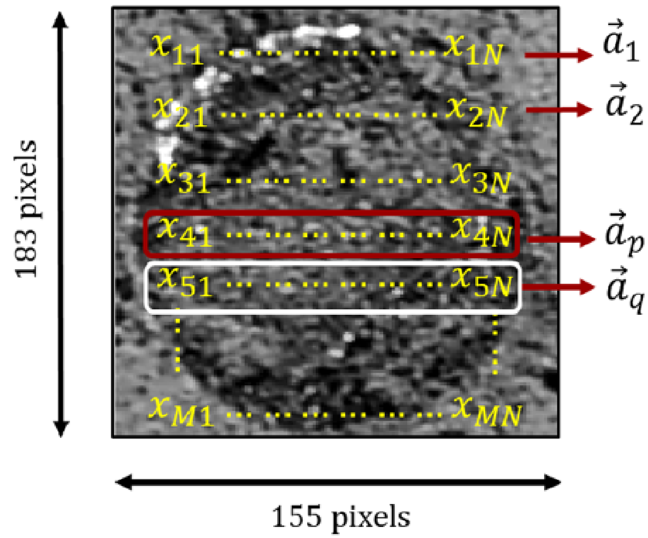

Figure 2.10. An in-situ image of part depicting the row vectors which are used for pairwise comparison.

Further, a pairwise comparison is performed between each of the row vectors through a kernel function Ω [86]. A pairwise comparison along the columns has been shown to lead to similar results as long as the image is homogeneous [87].

$$w_{pq} = \Omega(\overrightarrow{a_p}, \overrightarrow{a_q}) \quad \forall\, p, q \in K \tag{2.1}$$

The kernel function Ω used in this study to compute the pairwise comparison is the radial basis kernel function (Eq. 2.2 and 2.3) .

$$w_{pq} = e^{-[\frac{\boldsymbol{E}}{\sigma_X}]^2} \tag{2.2}$$

$$\boldsymbol{E} = [\|\overrightarrow{\boldsymbol{a}_p} - \overrightarrow{\boldsymbol{a}_q}\|^2] \tag{2.3}$$

where, σ_X is the overall standard deviation of $\boldsymbol{E}$. Next, a binary similarity matrix $\boldsymbol{\mathcal{S}} = [w_{pq}]$ is created with help of a threshold function. This threshold function θ when applied to w_{pq} converts it into binary form [88].

$$\Theta(w_{pq}) = \mathrm{w}_{pq} = (0, 1) \tag{2.4}$$

This threshold function facilitates in determining whether there is a connection between two nodes [88]. $w_{pq} = 1$ if there is a connection and otherwise it is zero.

$$\Theta(w_{pq}) = \mathrm{w}_{pq} = \begin{cases} 1, & w_{pq} \leq r \\ 0, & w_{pq} > r \end{cases} \tag{2.5}$$

Here r is given by,

$$r = \frac{\sum_{p=1}^{p=M} \sum_{q=1}^{q=M} \mathrm{w}_{pq}}{M^2} \tag{2.6}$$

Step 2: *Extracting features from the graph.*

Once a graph is formulated from the image, topological features are extracted from the graph. These features are useful in classification of parts which are made with different process parameters. The first step towards feature extraction is computing the degree d_p of a node p, i.e., the number of edges that pass through the node p. The degree of node p is computed by summing each row in the similarity matrix $\boldsymbol{\mathcal{S}}$. From the degree of node d_p, a diagonal degree matrix $\boldsymbol{\mathcal{D}}$ is formed as follows:

$$\boldsymbol{\mathcal{D}}(d_1, ..., d_M) \tag{2.7}$$

Now, with the help of the degree $\boldsymbol{\mathcal{D}}$ matrix and the similarity matrix $\boldsymbol{\mathcal{S}}$, the normalized Laplacian $\boldsymbol{\mathcal{L}}$ of the graph is defined as follows,

$$\boldsymbol{\mathcal{L}}\boldsymbol{\mathcal{D}}^{-\frac{1}{2}} \times (\boldsymbol{\mathcal{D}} - \boldsymbol{\mathcal{S}}) \times \boldsymbol{\mathcal{D}}^{-\frac{1}{2}} \tag{2.8}$$

where, $\boldsymbol{\mathcal{D}}^{-\frac{1}{2}} = (\frac{1}{\sqrt{d_1}}, ..., \frac{1}{\sqrt{d_M}})$.

Finally, the Eigen spectra of the Laplacian is computed as follows [89].

$$\boldsymbol{\mathcal{L}}\boldsymbol{v} = \lambda^* \boldsymbol{v} \tag{2.9}$$

The eigenvalues (λ) of the Laplacian are used in the classification of LPBF parts per their processing conditions. In this work, the first five smallest non-zero eigenvalues are used. Also, the Kirchhoff index for each graph is computed as follows, where λ_i are the non-zero eigen values of the Laplacian.

$$K_f = 2 \times \varepsilon \times \sum_{i=2}^{M} \lambda_i^{-1} \tag{2.10}$$

where $\varepsilon = \frac{\sum_{i=1}^{i=M} \sum_{j=1}^{j=M} \boldsymbol{s}_{ij}}{2}$.

The non-irradiated part of the part image i.e. the un-sintered powder, is fairly homogenous, so when it the image undergoes a row-wise comparison, the distance kernel function becomes zero. The nodes which are far apart from each other are connected on the graph.

(b) *Multifractal and lacunarity analysis of part images*

The fractal dimension has been extensively used to characterize the texture and patterns of manufactured surfaces [35, 90–92]. This work goes beyond the traditional methods that extract a single fractal dimension from the surface image, but rather assume the irregularity and non-homogeneity of image data are due to the presence of several fractal dimensions [92]. As such, we extract a spectrum of multifractal features to characterize the layer-by-layer images obtained in LPBF. A fractal is defined as a shape that embodies geometric similarity across multiple scales [9, 93, 94]. Assuming that a fractal object occupies a limited area in the Euclidean space, then the object can be covered by N measure elements with size as follows,

$$N(l) = l^{-D} \tag{2.11}$$

where D is the fractal dimension. The box-counting method is widely used to estimate the fractal dimension of an irregular object. This method covers a fractal set with measure elements (e.g., box) at different sizes and observes how the number of boxes varies with its size [95]. This procedure is repeated using different boxes of size l. Once the l becomes sufficiently small, $N(l)$ being the number of boxes that are needed to cover a fractal object with the size l, then the box-counting dimension D_0 is defined as,

$$D_0 = \lim_{l \to 0} \frac{\ln N(l)}{\ln \frac{1}{l}} \tag{2.12}$$

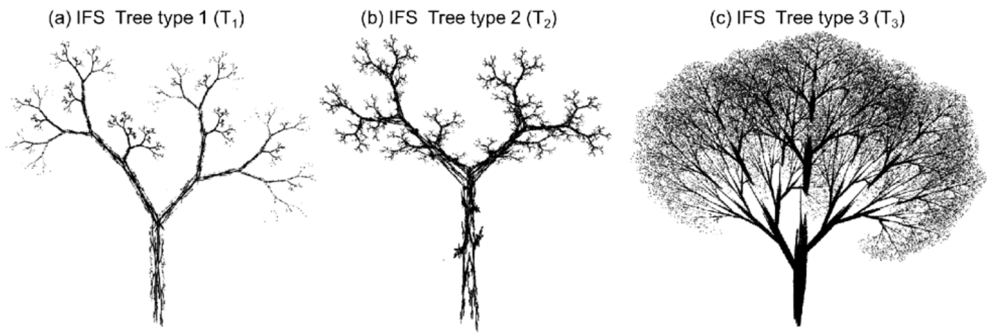

Figure 2.11. An in-situ image of part depicting the row vectors which are used for pairwise comparison.

For example, Figure 2.11 shows three types of fractal objects called multifractal trees that are constructed with the iterated function systems (IFS) method. These fractal trees are labeled T_1, T_2, and T_3. The estimates of fractal dimension (D_0) using the box-counting method in Figure 2.11 are $D_0 = 2.0449$ for all three fractal trees. However, three trees show high levels of self-similarity, irrgularity and heterogeneity due to the presence of a spectrum of fractal dimensions. This demonstrates that the traditional box-counting fractal dimension is limited in the ability to fully characterize the patterns of multifractal objects [96]. Multifractal analysis provides a means to overcome this limitation of traditional fractal dimensions. The procedure to estimate the multifractal spectrum from image data is as follows:

Step 1: *Estimating the local densities function* $(P_i(L))$.

$$P_i(l) = \frac{N_i(l)}{N_T} \tag{2.13}$$

where $N_i(l)$ is the number of mass or pixels in the ith box of size l, N_T is the total mass of a set and $P_i(l)$ is the probability in the ith box.

Step 2: *Calculating singularity strength exponent* (l^{α_i}).

$$P_i(l) \sim l^{\alpha_i} \tag{2.14}$$

where α_i reflects the local behavior of $P_i(l)$ in the ith box with size l and it can be derived as

$$\alpha_i = \lim_{l \to 0} \frac{\ln P_i(l)}{\ln l} \tag{2.15}$$

Step 3: *Estimating multifractal spectrum* ($f(\alpha)$).

The multifractal spectrum $f(\alpha)$ is the fractal dimension of the set of locations that have same values for singularity strength exponents α_i. Given the number of boxes $N(\alpha)$ where the probability $P_i(l)$ has exponent values between α and $\alpha + d\alpha$ the multifractal spectrum $f(\alpha)$ can be calculated as follows,

$$f(\alpha) = \lim_{l \to 0} \frac{\ln N(\alpha)}{\ln \frac{1}{l}} \tag{2.16}$$

Step 4: *Characterizing multifractal measures* (D_q).

Multifractal measures are characterized by the scaling of the q^{th} moments of $P_i(l)$ distributions as,

$$\sum_{i=1}^{N(l)} P_i^q(l) = l^{\tau(q)} \tag{2.17}$$

where $\tau(q)$ is called the mass exponent of q^{th} order moment. Then, the generalized fractal dimensions D_q can be written as,

$$D_q = \frac{\tau(q)}{q-1} \tag{2.18}$$

Then, the Legendre transformation is used to derive the multifractal spectrum as

$$f(\alpha(q)) = q\alpha(q) - \tau(q) \tag{2.19}$$

$$\alpha(q) = \frac{d\tau(q)}{dq} \tag{2.20}$$

However, Legendre transformations are computationally demanding in the calculation of $f(\alpha)$. Also, this approach requires smoothing the D_q curve the which causes errors in the estimated $f(\alpha)$ [97]. To overcome this limitation and bypass intermediate smoothing steps in estimating $f(\alpha)$, a family of normalized measures $\mu_i(q,l)$ as qth moments of mass probability $P_i(l)$ are introduced in Eq. 2.21. A constant l range is also used to avoid multifractal properties over a small interval of scales.

$$\mu_i(q,l) = \frac{P_i^q(l)}{\sum_{i=1}^{N(l)} P_i^q(l)} \tag{2.21}$$

As such, the multifractal spectrum $f(\alpha)$ and the average singularity strength exponent $\alpha(q)$ can be written as,

$$f(\alpha(q)) = \lim_{l \to 0} \frac{\sum_{i=1}^{N(l)} \mu_i(q,l) \ln[\mu_i(q,l)]}{\ln l} \tag{2.22}$$

$$\alpha(q) = \lim_{l \to 0} \frac{\sum_{i=1}^{N(l)} \mu_i(q,l) \ln[P_i^q(l)]}{\ln l} \tag{2.23}$$

Figure 2.12 shows the multifractal spectra for three IFS trees in Figure 2.11. It is evident that multifractal features effectively distinguish the differences in the three IFS trees that were not captured using the traditional fractal dimension. Note that the tail of the third IFS tree T_3 is longer than other two IFS trees. Because T_3 has more pixels with lower values (value towards 0 or black pixels) in comparison to the other two trees and the $f(\alpha(q))$ spectrum intensifies the effect of pixels with lower values.

Furthermore, lacunarity complements multifractal analysis by characterizing the manner or distribution in which the fractal objects fill the space [98, 99]. Lacunarity and multifractal analysis jointly describe the irregularity and non-homogeneity in fractal objects as well as how they fill the space that cannot be otherwise achieved by traditional box-counting dimension or statistical features. To obtain the lacunarity measure, a unit box of size l is placed over the object and the number of set points s (black pixels) in the image is counted - this is called the box mass. Next, the box is translated one space along the set, and the box mass is again determined. This process is repeated over the entire set, creating a frequency distribution of the box masses represented as $N(s,l)$. This frequency distribution is converted into a

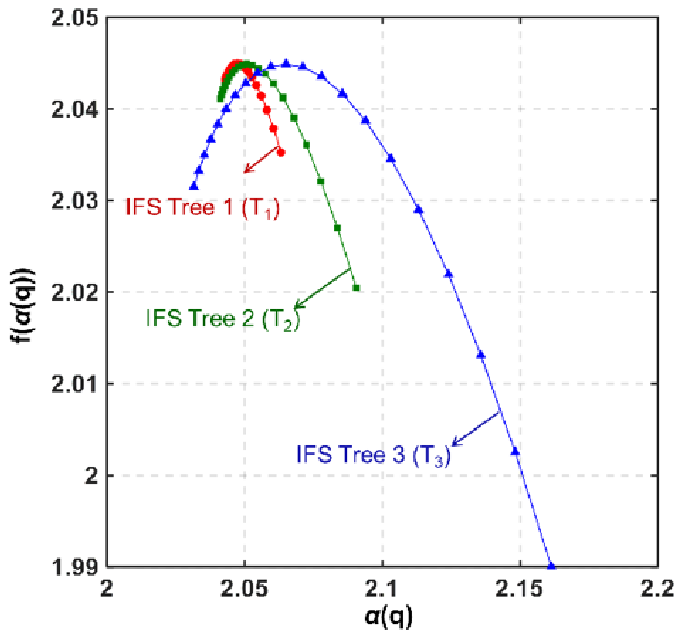

Figure 2.12. Multifractal spectra of IFS trees shows the self-similarity, irregularity, and non-homogeneity of fractal objects that cannot be adequately characterized using a single fractal dimension.

probability distribution $Q(s, l)$ by dividing by the total number of boxes $N(l)$ of a given size l [100].

$$Q(s, l) = \frac{N(s, l)}{N(l)} \tag{2.24}$$

The first and second moments of this distribution can be written respectively as:

$$Z(1) = \sum sQ(s, l) \tag{2.25}$$

$$Z(2) = \sum s^2 Q(s, l) \tag{2.26}$$

The lacunarity method with box size l can be computed as:

$$\Lambda(l) = \frac{Z(2)}{(Z(1))^2} \tag{2.27}$$

In Eq. 2.24, $\Lambda(l)$ represents the lacunarity for the box size l. This procedure is repeated for different box sizes, and a log-log plot of the lacunarity versus the size of the box is traced. Figure 2.13 shows T_3 has higher lacunarity values in comparison to the two other trees. The distribution of gap sizes is termed as lacunarity.

Figure 2.14 shows the singularity strength exponent (q) and multifractal spectrum $f(\alpha(q))$ estimated from 3132 layerwise images in the LPBF process. There are 1044 images in $E_A = 2.27$; 696 in $E_A = 1.81$; 348 in $E_A = 1.70$; 696 in $E_A = 1.51$; and 348 in $E_A = 1.13$. Note that multifractal spectra of these images show significant variations with respect to the different Andrew's numbers.

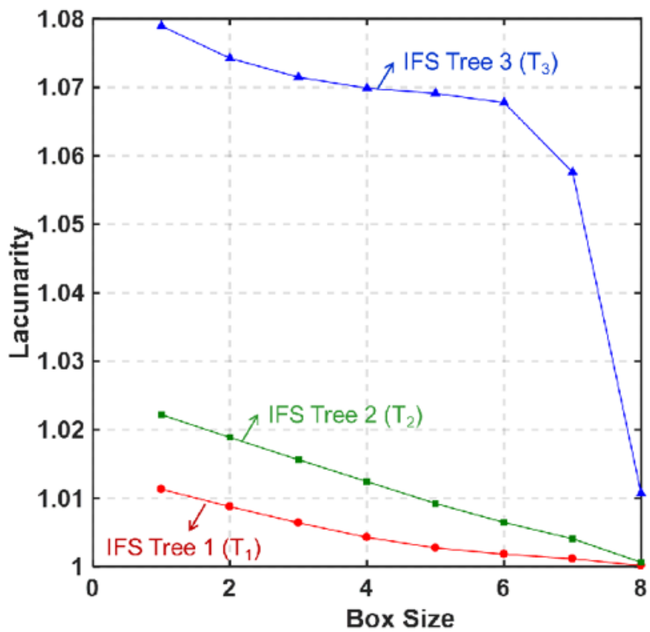

Figure 2.13. Lacunarity analysis of IFS trees describes how fractal objects fill the space that cannot be adequately captured using traditional fractal analysis.

2.4.3 Application of multifractal and spectral graph theory to online images

Further, the parts built under the different E_A conditions described in Table 2.1 were classified using different machine learning approaches with various types of input features. A 70%-15%-15% split for training, testing, and validation data were imposed. The classification fidelity is reported in terms of the F-score, which is an

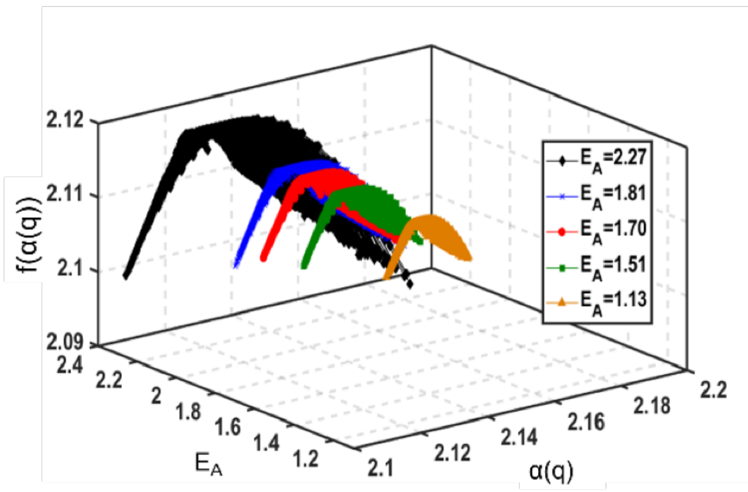

Figure 2.14. The variations of multifractal spectra with respect to the the Andrew's Number for 3132 layerwise images in the LPBF process.

aggregate of the Type I and Type II statistical errors. The results are summarized in Table 2.4.

Table 2.4. Mean counts of pores and its standard deviation (in brackets) at various locations of the XCT scan image in various printing conditions.

Classifier	Statistical features	(A) Spectral graph theoretic features	(B) Multifractal and lacunarity features	Combined features A+B
Support Vector Machine	55.58% (0.58)	71.94% (0.20)	76.16% (0.30)	89.36% (0.21)
Complex Tree	54.10% (0.14)	68.02% (0.50)	68.60% (0.30)	79.98% (0.23)
Linear Discriminant Analysis	52.72% (0.34)	63.22% (0.49)	63.02% (0.08)	82.16% (0.21)
K-Nearest Neighbor	56.62% (0.50)	67.66% (0.25)	70.38% (0.27)	78.60% (0.34)
Ensemble (Bagged Trees)	51.06% (0.58)	72.50% (0.10)	72.68% (0.61)	85.86% (0.30)
Feed Forward Neural Network	49.66% (1.99)	64.62% (1.70)	66.54% (1.76)	84.40% (1.67)

Three types of input features are used: (1) statistical image features, namely, intensity (mean) of an image, and local standard deviation of an image in 3×3 neighborhood, (2) spectral graph theoretic features, namely, the first five non-zero Eigenvalues and the Kirchhoff index, and (3) the multifractal and lacunarity features. It is observed that irrespective of the classification approaches used, the spectral graph and multifractal and lacunarity features outperform the conventional statistical features. Furthermore, combining the spectral graph and multifractal features results in F-score around 80%. The results reported in Table 2.4 show that the spectral graph theoretic and multifractal features discriminate the part quality with higher fidelity than traditional statistical analysis. This is valuable from the in-process quality monitoring viewpoint. In a practical scenario, images of the parts can be used to conclude whether the process within an optimal window.

2.5 Conclusions

This paper presents the modeling and analysis of in-process layerwise images in LPBF to investigate the effect of LPBF process conditions on the severity, size, and location of porosity, and further connects the process conditions to sensor signatures. This is an indirect way to monitor the LPBF process. The specific outcomes of the work are as follows:

1. Three process parameters, namely, laser power (P), hatch spacing (H), and scan velocity (V) were varied during the LPBF of Ti-6Al-4V powder material. The effect of varying these parameters on porosity was characterized offline using X-ray computed tomography (XCT). Based on analysis of the XCT images the following inference is tendered. Decreasing the laser power by 50% from 340 W to 170 W leads to almost a three-fold increase in the average number of pores, compared to an equivalent percentage increase in hatch spacing, and ten-fold increase compared to scan velocity. Hence, the control of laser power is most consequential for avoiding porosity.

2. Online visible spectrum images of the part were acquired as they are built using a still camera. These images were analyzed using multifractal and graph theoretic approaches. The features extracted by applying these approaches were subsequently used within various machine learning techniques. The aim was to distinguish the process conditions under which the parts were built given an image of the part. It is observed that combining multifractal and graph theoretic analysis leads to as much as 30% increase in the accuracy of discriminating process conditions compared to using traditional statistical measurements. Using this approach, the process conditions can be isolated with F-score approaching 80%. From a practical perspective, although the P, H, and V settings are predetermined for each material in terms of the

Andrew number (E_A), the laser power, particularly, is liable to drift due to occlusion of the focusing optics; the vaporized material tends to condense on the lens especially during long builds.

3. There is the possibility of a complex, nonlinear interaction between P, V, and H which remains as yet undiscovered and therefore not captured in the relationship representing the areal energy density. For instance, in the equation for E_A, all terms are assumed to be equal in weight, i.e., the exponent P, V, and H is unity (=1) and therefore the relationship between E_A and the process parameters is implicitly assumed to be a simple linear relationship. The observed nonlinear relationship leads to the considerable distance among the 5 group of classes as a function of P. This in turn impacts more pronounced differentiation in classification results.

Chapter 3 Multifractal and Lacunarity Analysis

Joint Multifractal and Lacunarity Analysis of Image Profiles for Manufacturing Quality Control

Abstract

The modern manufacturing industry faces increasing demands to customize products according to personal needs, thereby leading to the proliferation of complex designs. To cope with design complexity, manufacturing systems are increasingly equipped with advanced sensing and imaging capabilities. However, traditional statistical process control methods are not concerned with the stream of in-process imaging data. Also, very little has been done to investigate nonlinearity, irregularity, and inhomogeneity in the image stream collected from manufacturing processes. This paper presents the joint multifractal and lacunarity analysis to characterize irregular and inhomogeneous patterns of image profiles, as well as detect the hidden dynamics in the manufacturing process. Experimental studies show that the proposed method not only effectively characterizes surface finishes for quality control of ultra precision machining but also provides an effective model to link process parameters with fractal characteristics of in-process images acquired from additive manufacturing. This, in turn, will allow a swift response to processes changes and consequently reduce the number of defective

products. The proposed multifractal method shows strong potentials to be applied for process monitoring and control in a variety of domains such as ultra precision machining and additive manufacturing.

3.1 Introduction

Fierce competition in global market leads manufacturing companies to offer highly personalized products with complex designs according to the customers' needs [101, 102]. This trend calls for the development of a next-generation manufacturing system that is highly flexible and adaptive to complex and customized designs according to personal needs and requirements. However, quality control of such complex products depends on advanced sensing, process monitoring and control. For example, UPM is a commonly used manufacturing process to produce optical discs, photoreceptor components, and aircraft engines [103]. Such applications require mirror surface finishes with extremely high geometrical accuracies and smooth surfaces (i.e., surface roughness < 50 nm). Also, AM provides a higher level of flexibility to print a 3D product with the complex geometry layer by layer [3]. The LPBF process spreads the material powder over previous layers, and then use a laser or electron beam energy source to melt the material powder to print a new layer of the product [104]. Qualifying complex builds is extremely challenging. It was reported that among seven parts built simultaneously on a commercial LPBF machine, only two out of seven are defect free. Therefore, there is an urgent need to develop advanced quality control methods for monitoring surface finishes as we move into a more complex and high-precision manufacturing [105].

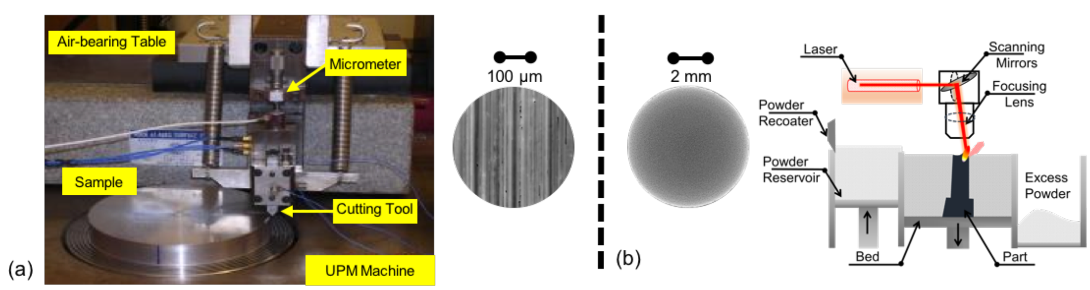

Figure 3.1. (a) UPM experimental setup, and (b) the schematic diagram of the LPBF process.

Most of the complexity in the data arises from the complex products as well as nonlinear and nonstationary dynamics in the manufacturing processes. Prior work showed the characterization of nonlinear dynamics in manufacturing systems and the resulted variations in products and systems performances [106]. Traditional SPC methods mainly focus on key characteristics of the product and the conformance to specification, but they are less concerned about high-dimensional image data and nonlinear dynamics in manufacturing processes. Manufacturing system dynamics, confined by the evolution of states of the underlying process, exhibit aperiodic, strange and irregular behaviors. Gültekin et al. [107] and Singer and Ben-Gal [108] showed that engineering control implementations often bring nonlinear dynamics of sensor observations in manufacturing processes.

There is a critical gap in the knowledge base that pertains to integrating nonlinear dynamics research with manufacturing quality control. Available nonlinear dynamics techniques are either not concerned with quality control objectives or fail to effectively analyze big data (e.g., high-dimension image data) to extract useful information for process control. There is an urgent need to harness and exploit nonlinear dynamics for creating new products (or services) with exceptional features such as adaptation, customization, responsiveness, and quality in unprecedented scales. The nonlinear dynamics theory focuses on the geometric properties of the state space of dynamical systems. For example, the fractal dimension is commonly used to describe the complex geometries of fractal objects (e.g., time series, 2D or 3D images) that are self-similar and scale invariant. The fractal dimension can be a non-integer value that exceeds the topological dimension of the object.

However, a single fractal dimension focuses on the self-similarity (scale invariant) behavior of the fractal object and is limited in the ability to completely describe the multifractal patterns (i.e., nonlinearity, irregularity, and inhomogeneity) in complex real-world objects. For example, image data from real-world manufacturing processes often do not show perfect self-similarity but are formed by subsets with inhomogeneous scaling properties. The multifractal analysis is an effective tool to characterize inhomogeneity and nonlinear patterns of real-world images using an interwoven set of fractals with different dimensions. Furthermore, lacunarity complements multifractal analysis by characterizing the manner or distribution in which the fractal objects fill the space. Lacunarity and multifractal analysis jointly describe the irregularity and non-homogeneity of fractal objects as well as how they fill the space that cannot be otherwise achieved by traditional fractal dimension or statistical features.

This chapter presents the multifractal and lacunarity analysis of image profiles in UPM and AM processes for manufacturing process and monitoring and quality control. The multifractal spectrum resolves local densities and captures nonhomogeneous variations of image profiles. Lacunarity complements multifractal analysis by characterizing the filling patterns in image profiles. Further, we derive the composite quality index by computing Hotelling's T^2 statistics from multifractal and lacunarity features for defect detection and characterization in UPM and AM image profiles. Finally, we investigated the correlation between the Hotelling's T^2 statistics and process parameters (i.e., hatch spacing, scan velocity, and laser power) in AM using multivariate regression analysis. Experimental results on real-world UPM and AM applications show that the proposed approach not only effectively detects and characterizes defects in image profiles, but also provides an effective prediction model to link process parameters with image characteristics in AM processes.

The remainder of this chapter is organized as follows: 3.2 introduces research background of nonlinear dynamics in manufacturing systems, imaging technology, and fractal theory. 3.3 presents the research methodology of multifractal and lacunarity analysis of image profiles from manufacturing processes. Case studies and experimental results are provided in 3.4. 3.5 discusses and concludes the present research.

3.2 Research Background

3.2.1 Manufacturing processes and advanced imaging technology

As shown in Figure 3.1, UPM and AM processes are advanced manufacturing technologies that offer unique capabilities such as high precision and flexible customization that cannot be matched by traditional manufacturing techniques. UPM is equipped with air-bearing spindles and diamond tools to produce optical surface finishes (i.e., roughness < 50 nm). Also, the LPBF process employs a laser power source for melting the material. A scanning galvanic mirror assembly scans rasters the laser across the powder bed. The laser is focused on the bed with a spot size on the order of 50 μm to 100 μm in diameter. Its power is typically maintained in the range of 200 W to 400 W, and the linear scan speed of the laser is varied in the 200 mm/s to 2000 mm/s range [33]

Advanced sensing brings the increasing availability of high-dimensional images, which are critical to quality inspection and process improvement. For examples, Figure 3.1(a) shows the UPM surface extracted by high resolution optical laser interference microscope (MicroXAM®) and a stylus-based profilometer (TalySurf®). Figure 3.1(b) shows the industrial X-ray computed tomography (XCT) image for quality inspection of complex builds from LPBF process.

Although UPM and AM offer exceptional capabilities, qualifying complex products are still challenging. Very little has been done to study nonlinear and fractal patterns in real-world images and further exploit the useful information from high-resolution image data for the purpose of quality inspection.

3.2.2 Fractal Theory

In the natural world, there exist many irregular objects that show self-similarity to some degrees. For example, the human heart is formed of a fractal network of myocardium cells [109–111]. They are often referred to be the fractal geometry. The fractal theory has found many applications in many domains such as health informatics and manufacturing. Ruschin-Rimini et al. [112] developed a fractal-SPC method that uses the fractal dimension to measure the probability of the occurrence of correlated data sequences for process monitoring and change detection.

Further, manufactured surface finishes often exhibit fractal characteristics [93, 113]. For example, UPM surface finishes seem to have smooth surfaces with the visual inspection. However, fine-grained surface textures in the microscope demonstrate fractal behaviors over a range of scales. Fractal models provide insights on various functional and operational behaviors of manufacturing processes. In the literature, a single fractal dimension has been utilized to investigate the scale effect in surface metrology and consequently process monitoring [114, 115]. Note that prior works showed that a single fractal dimension is limited in the ability to fully characterize heterogeneous and irregular patterns in the surface finishes from the manufacturing process. The surface finishes of manufacturing parts often comprise of complex characteristics that are due to the existence of spectrum of fractal dimensions that interact with each other to generate highly nonlinear behaviors. In addition, lacunarity analysis complements the multifractal analysis by describing how the fractal object fills the space. Very little has been done to integrate multifractal analysis with lacunarity patterns in image profiles for the purpose of quality monitoring and control of UPM and AM processes.

3.3 Research Methodology

As shown in Figure 3.2, this paper presents a joint multifractal and lacunarity analysis for the characterization and modeling of image profiles in manufacturing process and further link fractal characteristics with manufacturing process parameters. First, we extract the multifractal spectrum and lacunarity measures to characterize the heterogeneous and irregular patterns of UPM and AM image profiles. Second, we compute the composite quality index, i.e., the Hotelling's T^2 statistic of multifractal and lacunarity features. In other words, this composite index helps summarize the variations in the multi-dimensional features. Third, we utilize the Hotelling's T^2 control chart to monitor the quality of UPM surface finishes, as well as develop a regression model to link the composite index with process settings in AM.

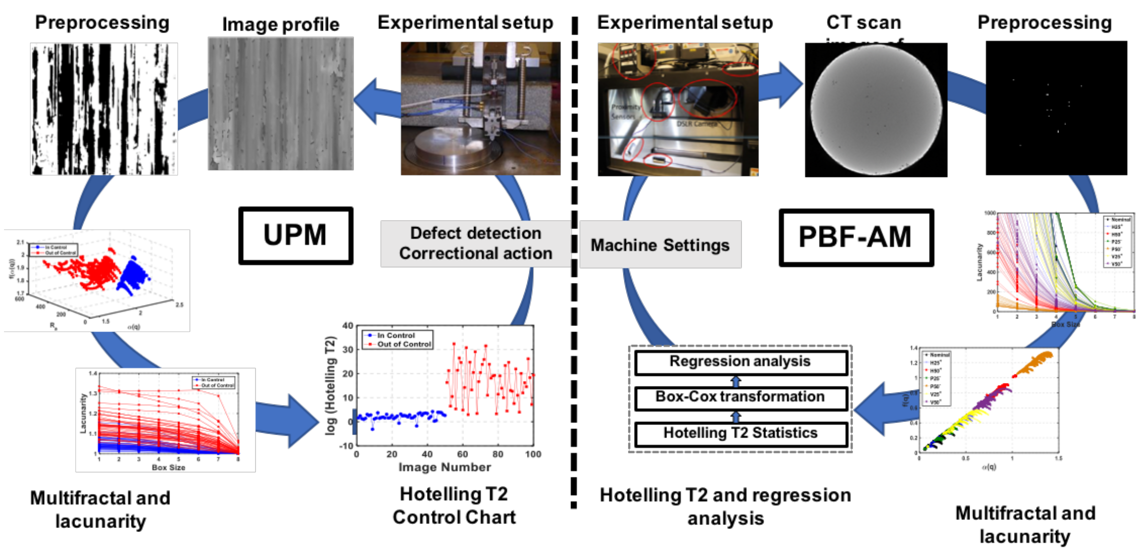

Figure 3.2. Flow diagram of the research methodology.

3.3.1 Multifractal analysis

The fractal object shows self-similarity across multiple scales. In other words, if one zooms in or out the fractal set, there will be a similar appearance in the geometry. Fractal are irregular geometric objects that cannot be fully characterized by the topological dimensions. Therefore, the fractals dimension is introduced to describe scale-invariance properties of the fractal object by measuring the changes of covering relative to the scaling factor and characterizing the filling space capacity.

The box-counting method is widely utilized to estimate the fractal dimension of an irregular object. For example, if we cover the fractal object by N measure elements (e.g., boxes) with size l as follows,

$$N(l) = l^{-D} \tag{3.1}$$

where D is the box-counting fractal dimension, then Eq. 3.1 provides the scaling law to demonstrate the distribution size of objects. This method covers a fractal set with measure elements (e.g., boxes) at different sizes and observes how the number of boxes with respect to the size [96]. This procedure is repeated using different size of l. Once the l becomes sufficiently small, the number of boxes $N(l)$ is increased to cover a fractal object. Then, the box-counting dimension is defined as follows,

$$D_0 = \lim_{l \to 0} \frac{\ln N(l)}{\ln \frac{1}{l}} \tag{3.2}$$

To illustrate the self-similarity and irregularity in surface finishes, we used the Voronoi tessellation to iteratively divide a plane with points into convex polygons such that each polygon holds just one generating point and each point in a specified polygon is closer to its generating point than to any other (See Figure 3.3 (a-c)). The dual of the Voronoi tessellation has been denoted as Delaunay triangulation. Figure 3.3 (d-f) show the Delaunay triangulation that is the dual of Voronoi tessellation. As shown in Figure 3.3 the surface of Voronoi tessellation and Delaunay triangulation undergo significant changes when the number of cells is increased from 100 to 1000. The box-counting method shows the fractal dimension is for both Voronoi and Delaunay surfaces in Figure 3. This indicates that a single fractal dimension just represents the average fractality in an image and is not sufficient enough to describe nonlinear and irregular behaviors. The box-counting method

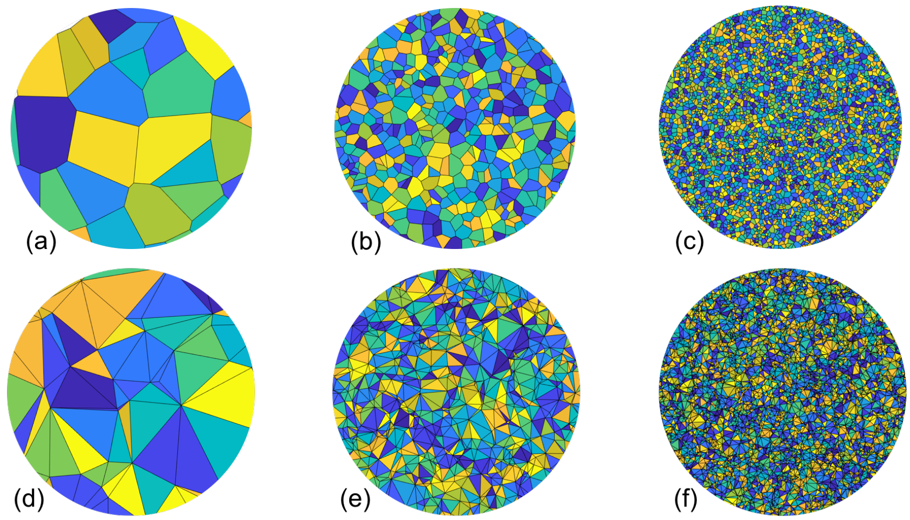

Figure 3.3. Voronoi tessellation with different number of cells: (a) 100 cells; (b) 1000 cells; (c) 10000 cells; and Delaunay triangulation with different number of cells: (d) 100 cells; (e) 1000 cells; (f) 10000 cells.

assumes that the number of boxes has a linear relationship with the ruler length of each box when both are logarithmically transformed. In other words, it is very rare to have perfect self-similarity in the real world.

To overcome the limitation of single fractal dimension, multifractal analysis splits the fractal set with the complex statistics into the various homogeneous sets with different fractal dimensions. As a result, multifractal spectrum provides a more complete and intuitive description of the irregular object with an interwoven set of fractal dimensions. The procedure for calculating the multifractal spectrum is as follows,

a. Estimating the local density function. In practice, one way to quantify local densities is by estimating the mass probability in the i^{th} box as:

$$P_i(l) = \frac{N_i(l)}{N_T} \tag{3.3}$$

b. Calculating the singularity strength exponent. For the inhomogeneous set, we can define the singularity strength exponent α_i as,

$$P_i(l) \sim l^{\alpha_i} \tag{3.4}$$

Where α_i reflects the local behavior of $P_i(l)$ in the i^{th} box with size l and it can be estimated as

$$\alpha_i = \lim_{l \to 0} \frac{\ln P_i(l)}{\ln l} \tag{3.5}$$

c. Estimating the multifractal spectrum. The multifractal spectrum $f(\alpha)$ characterizes the variations and provides statistical distribution of singularity exponents α_i. The number of boxes $N(\alpha)$ where the probability $P_i(l)$ has exponent values between α and $\alpha + d\alpha$ also follows the scaling law with the size l and multifractal spectrum $f(\alpha)$. It can be shown as follows.

$$N(\alpha) \sim l^{-f(\alpha)} \tag{3.6}$$

The multifractal spectrum is a concave downward function due to two extreme properties of the measure (i.e., sparser or denser measure) and can be estimated from Eq. 3.6 as

$$f(\alpha) = \lim_{l \to 0} \frac{\ln N(\alpha)}{\ln \frac{1}{l}} \tag{3.7}$$

The scaling of the q^{th} moments of $P_i(l)$ distributions can be expressed as,

$$\sum_{i=1}^{N(l)} P_i^q(l) = l^{\tau(q)} \tag{3.8}$$

where $\tau(q)$ is called the mass exponent of q^{th} order moment. Thus, the fractal dimensions D_q can be written as:

$$D_q = \frac{\tau(q)}{q-1} \tag{3.9}$$

When $q = 0$, Eq. 3.8 becomes $N(L) = l^{-D_0}$ which is similar to Eq. 3.1. In other words, the generalized fractal dimension D_q is the same as box-counting dimension D_0. The Legendre transformation is a conventional method used to estimate multifractal spectra:

$$f(\alpha(q)) = q\alpha(q) - \tau(q) \tag{3.10}$$

$$\alpha(q) = \frac{d\tau(q)}{dq} \tag{3.11}$$

However, computing $f(\alpha(q))$ via Legendre transformation is complex and needs to smoothn D_q curve that causes errors to the estimated $f(\alpha$. Eq. 3.12 introduces a family of normalized measures as q^{th} moments of mass probability $P_i(l)$. A constant range of l is utilized to estimate multifractal properties over a small interval of scales.

$$\mu_i(q,l) = \frac{P_i^q(l)}{\sum_{i=1}^{N(l)} P_i^q(l)} \tag{3.12}$$

As a result, multifractal spectrum $f(\alpha(q))$ and average singularity strength exponent $\alpha(q)$ can be formulated respectively as:

$$f(\alpha(q)) = \lim_{l \to 0} \frac{\sum_{i=1}^{N(l)} \mu_i(q,l) \ln[\mu_i(q,l)]}{\ln l} \tag{3.13}$$

$$\alpha(q) = \lim_{l \to 0} \frac{\sum_{i=1}^{N(l)} \mu_i(q,l) \ln[P_i^q(l)]}{\ln l} \tag{3.14}$$

where $f(\alpha(q))$ and $\alpha(q)$ are the function of the moments q. These two curves are tangent to each other at $q = 1$. Figure 3.4 shows the multifractal spectrum and its major characteristics. The values in the right and left of D_0 represent negative and positive q values. Moments $q > 0$ signify the contribution of boxes with higher-value pixels in the estimates of $f(\alpha(q))$ and $\alpha(q)$. On the other hand, moments $q < 0$ signify the contribution of boxes with lower-value pixels in the estimation. It may be noted that the right tail of $f(\alpha(q))$ is longer than the left side. This is mainly due to the fact that the variation of $f(\alpha(q))$ and $\alpha(q)$ with respect to q is more sensitive when and the probability $P_i(l)$ are between 0 and 1.

3.3.2 Lacunarity

Further, lacunarity helps measure the filling-space capacity of fractals and textures that have the same fractal dimension and a very different visual appearance [116]. Lacunarity complements fractal dimension by determining how the fractal objects fill the space and thereby allows differentiating spatial patterns in different scales [117]. If we define the gaps in an image as pixels with a specific value or a specific interval of values, the higher lacunarity value is, the more variability is expected to be in

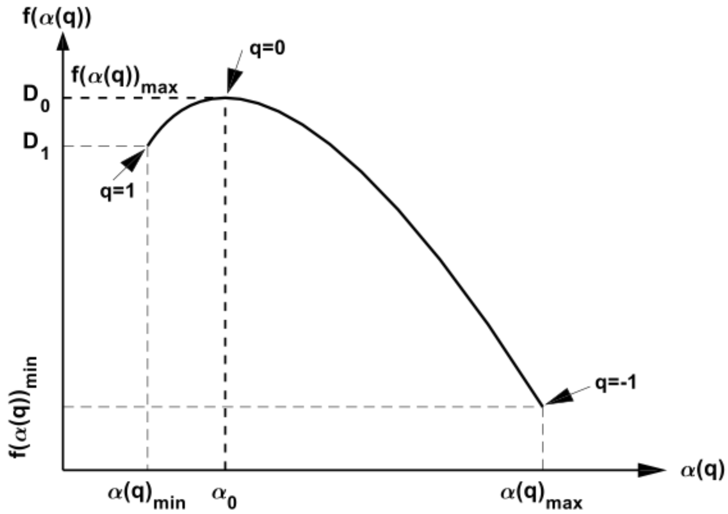

Figure 3.4. Characteristic points in the multifractal spectrum.

an image.

Gliding-Box and Differential Box-Counting are two main algorithms to calculate lacunarity of an image. We implement the computationally tractable "gliding box" method to compare the lacunarity [118]. A box of size l is placed in the image to counts the number of set points s (black pixels). Then, this box is moved to another spot in the image, and the box mass is again counted. This process is repeated over the entire image, creating a frequency distribution of the box masses $N(s,l)$. This distribution is converted into a probability distribution $Q(s,l)$ by dividing by the total number of boxes size l, $N(l)$ [117].

$$Q(s,l) = \frac{N(s,l)}{N(l)} \tag{3.15}$$

The first and second moments of this distribution and lacunarity for the gliding box method can be written respectively as:

$$Z(1) = \sum sQ(s,l) \tag{3.16}$$

$$Z(2) = \sum s^2 Q(s,l) \tag{3.17}$$

$$\Lambda(l) = \frac{Z(2)}{(Z(1))^2} \tag{3.18}$$

where $\Lambda(l)$ represents the lacunarity for the box size l. This procedure is repeated for different box sizes. The box size varies in the range of $2^1, ..., 2^b$ where b is the number of box sizes. Then we obtain the log-scale plot of the lacunarity versus the box sizes.

Figure 3.5(a) shows the estimated multifractal spectrum for Voronoi tessellation and Delaunay triangulation with 10000 cells (see Figure 3.3). Figure 3.5(b) illustrates lacunarity spectra of the Voronoi tessellation with different cells number in Figure 3.3.

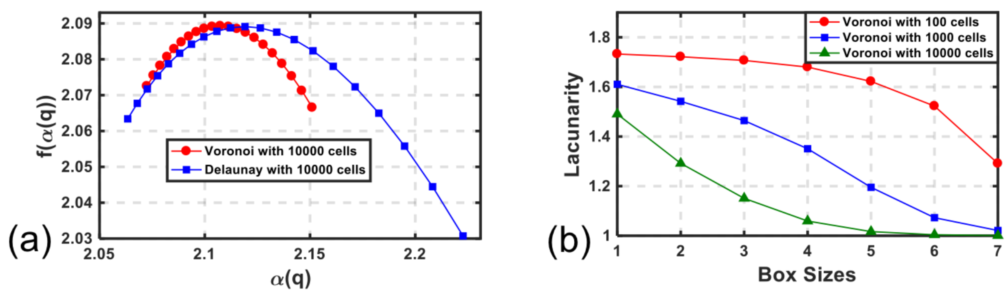

Figure 3.5. Multifractal spectra of the Voronoi tessellation and Delaunay triangulation in Figure 3.3; (b) lacunarity spectra of the Voronoi tessellation with different cells number in Figure 3.3.

Figure 3.5(a) shows that the single fractal dimension, i.e., the maximum values of $f(\alpha(q))$ is the same for both images. However, their multifractal spectra are significantly different from each other. The right tail of the Delaunay triangulation is longer than the dual Voronoi tessellation. This is due to the fact that Delaunay triangulation has more pixels with lower values (value towards 0 or black pixels) in comparison with the Voronoi tessellation. Figure 3.5(b) shows the Voronoi tessellation with 100 cells has higher lacunarity values than the other two. This mainly because lacunarity is related to the size distribution of the holes and deviation of an image from translational invariance. In other words, an object is very lacunar if its holes tend to be large and large gaps exist in an image. If there is a homogeneous image that has the same pixels per box, then the standard deviation, for a box count at the length scale l, will be close to the zero, and therefore lacunarity has a value close to the zero.

3.3.3 Multifractal-based Hotelling's T^2 control charts

The multifractal spectrum and lacunarity analysis provide a set of quality features relevant to the characteristics of surface finishes. When multiple variables require simultaneous monitoring, a univariate approach to monitor each feature is usually neither effective nor efficient. The hypothesis testing is to determine whether there is a significant mean shift in the feature vector as follows:

$$x^{(i)} = \{[\alpha(q_j), f(\alpha(q_j)), \Lambda(l_w)_{\forall w=1...b}]^{(i)}\} \quad \forall i = 1, ..., m \tag{3.19}$$

where k is the length of q-vector, $q_j \in [-1, 1]$ and b is the number of box sizes utilized in lacunarity calculation. If m is the number of images and p is the dimensionality or number of features which is determined by $f(\alpha(q))$, $\alpha(q)$ and $\Lambda(l)$, then the feature matrix will be $\boldsymbol{X}_{m\times p} = [\boldsymbol{x}^{(1)}, \boldsymbol{x}^{(2)}, ..., \boldsymbol{x}^{(m)}]^T$ with both multifractal and lacunarity quantifiers. To increase the sensitivity to small changes in each direction of multi-dimensional feature vector, we compute the Hotelling's T^2 statistics for the i^{th} image as

$$T^2(i) = (\boldsymbol{x}^{(i)} - \bar{\boldsymbol{x}})\boldsymbol{S}^{-1}(\boldsymbol{x}^{(i)} - \bar{\boldsymbol{x}}) \tag{3.20}$$

where the sample mean vector $\bar{\boldsymbol{x}}$ and sample covariance matrix $\boldsymbol{S}$ are estimated from in-control or nominal data. The upper control limit of Hoteling T^2 control chart is

$$UCL = \frac{p(m+1)(m-1)}{m(m-p)} F_{\alpha,p,m-p} \tag{3.21}$$

where p is the number of features of the dimensionality of $\boldsymbol{x}^{(i)}$ and m is the number of images, $F_{\alpha,p,m-p}$ is the upper $(1-\alpha)\%$ point of F distribution with p and $m-p$ degree of freedom. The Hotelling's T^2 statistics are utilized to characterize the differences in multifractal and lacunarity spectrum of UPM and LPBF image profiles. The proposed approach of multifractal analysis will be validated in experimental studies in the next section.

3.4 Experimental Design and Results

We evaluate and validate the proposed multifractal methodology in two real-world case studies UPM and LPBF image characterization for process monitoring and quality control. In the first case study, we aim to detect defects in the surface finishes of products from UPM process. In the second case study, we focus on modeling the relationship between process parameters with multifractal and lacunarity characteristics of XCT image profiles in LPBF process.

3.4.1 UPM application

This case study is aimed at evaluating the performance of multifractal and lacunarity for quality inspection of image profiles from the UPM process. In UPM process monitoring and control, R_a is one of the commonly used parameters which is the arithmetic average of absolute distance from each point of the roughness trace to the mean. However, this single parameter is restricted in its ability to represent and characterize the surface. It is possible that two surfaces have same R_a value, but they have different morphology.

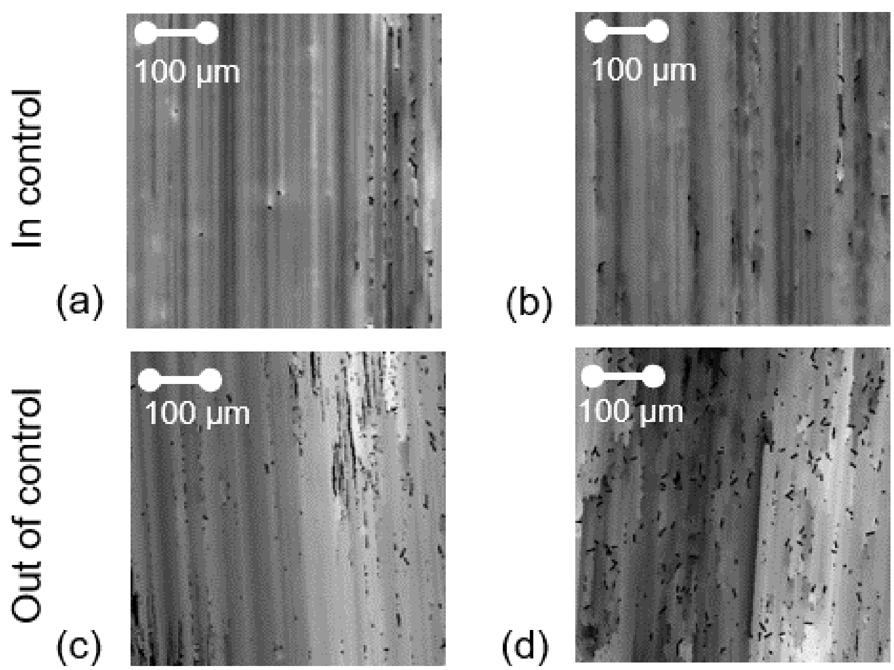

Figure 3.6. UPM images with smooth surfaces (in-control) with (a)R_a = 43.81 nm, (b) R_a = 43.83 nm and rough surfaces (out-of-control), (c) R_a = 297.58 nm, and (d) R_a = 296.92 nm.

As shown in Figure 3.6, R_a provides the aggregated information and tends to be limited in the ability to fully characterize the surface. Figure 3.6(a) and Figure 3.6(b) show two smooth surfaces with $R_a = 43.81$ nm and $R_a = 43.83$ nm, respectively. Also, Figure 3.6(c) and Figure 3.6(d) show two rough surfaces with $R_a = 297.58$ nm and $R_a = 296.92$ nm, respectively. Although R_a values are very close for two surfaces (either smooth or rough), their spatial patterns are different.

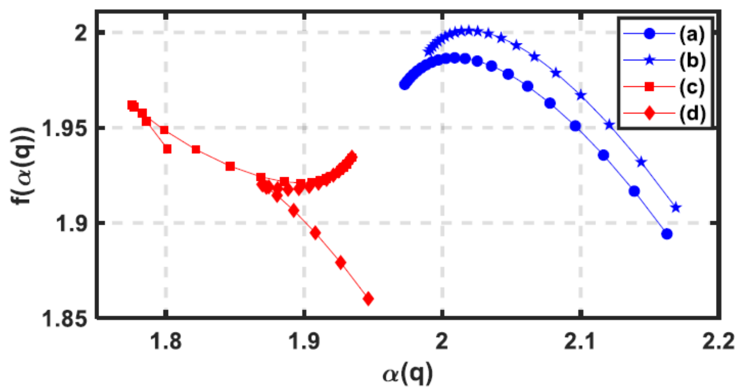

Figure 3.7. Multifractal spectra of four UPM images: (a) $R_a = 43.81$ nm, (b) $R_a = 43.83$ nm, (c) $R_a = 297.58$ nm, and (d) $R_a = 296.92$ nm in Figure 3.6

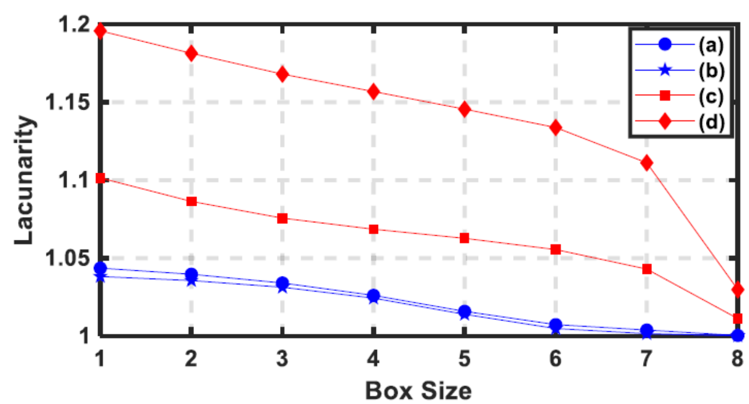

Figure 3.8. Lacunarity spectra of four UPM images: (a) $R_a = 43.81$ nm, (b) $R_a = 43.83$ nm, (c) $R_a = 297.58$ nm, and (d) $R_a = 296.92$ nm in Figure 3.6

Figures 3.7 and Figures 3.8 show the multifractal and lacunarity spectra for 4 UPM image profiles in Figure 3.6, respectively. Note that multifractal and lacunarity spectra of smooth surfaces (i.e., $R_a \approx 43$ nm) are away from those of rough surfaces (i.e., $R_a \approx 297$ nm). For the surfaces with the same R_a values, multifractal and lacunarity spectra are close to each other but show differences because of the variations in spatial patterns.

Based on the threshold value of the $R_a = 100\,\text{nm}$ which is commonly considered for detecting the defects in UPM process [119], 100 image profiles are split into the two groups of 50 in-control and 50 out-of-control. Figure 3.9 shows the multifractal spectra of all images regarding their surface roughness.

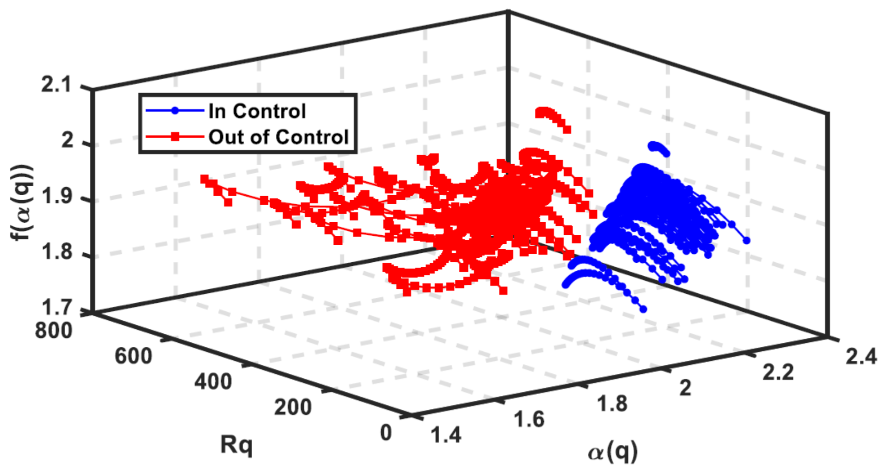

Figure 3.9. Multifractal spectra of UPM image profiles.

As shown in Figure 3.9, image profiles from in-control group show distinct multifractal spectra in comparison with those from out-of-control group. It is worth mentioning that, the multifractal spectra of in-control group are concave and they have higher values for $\alpha(q)$ in compare to the out-of-control image profiles. This is mainly due to the fact that there are more variation and heterogeneity in the inner layer of the out-of-control images, which can be uniquely represented by the novel method of multifractal analysis. Also, we extracted lacunarity measures for in-control and out-of-control image profiles to consider filling-space capacity of a multifractal object from the perspective of translational invariance. Figure 3.10 illustrates lacunarity spectra of in-control and out-of-control UPM image profiles with respect to the lacunarity box sizes.

As shown in Figure 3.10, the out-of-control images have higher lacunarity values for different box sizes in comparison with in-control image profiles. This shows that there are more gaps and heterogeneity in out-of-control image profiles. Next, we characterize the differences in multifractal spectrum $f(\alpha(q))$ and $\alpha(q)$ and

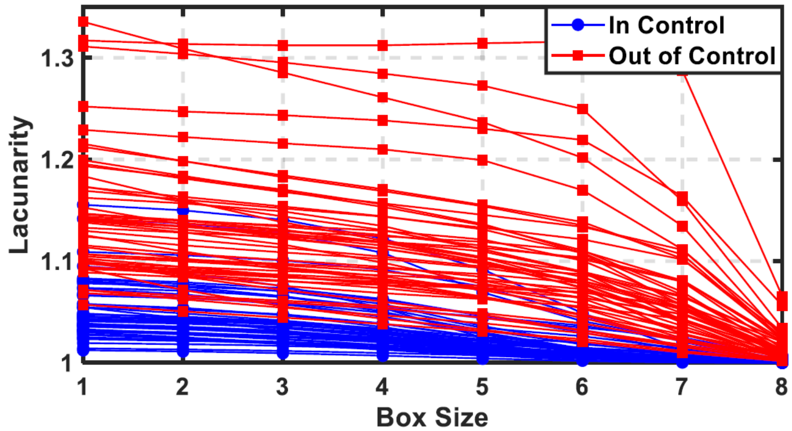

Figure 3.10. Lacunarity spectra of UPM image profiles.

lacunarity values of UPM image profiles by Hotelling's T^2 statistics. Figure 3.11 demonstrates the logarithm values of Hotelling's T^2 for in-control and out-of-control image profiles.

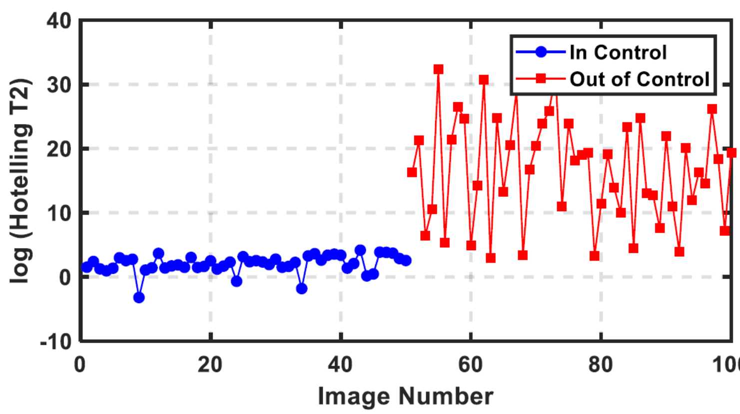

Figure 3.11. Hotelling's T^2 chart of UPM image profiles.

As shown in Figure 3.11, Hotelling's T^2 statistics intensifies the differences of feature vectors between in-control and out-of-control image profiles. It may be noted that the negative values of log Hotelling's T^2 statistics are related to Hotelling's T^2 statistics that have values close to the zero. The results show that multifractal and lacunarity analysis captures nonlinear variations inherent to an image profile by extracting useful information from local densities and heterogeneous patterns in multiple scales, as well as converting these features to the Hotelling's T^2 statistics for simultaneous monitoring.

3.4.2 LPBF application

The aim of this section is to quantify the effect of process conditions on part porosity in LPBF. In pursuit of this aim, we developed a multivariate predictive model to investigate the effects of three LPBF process parameters, namely, laser power (P), hatch spacing (H), and velocity (V) on the Hotelling's T^2 values from image profiles. LPBF experiments for this study were conducted using the EOS M280 machine along with spherical ASTM B348 Grade 23 Ti-6Al-4V powder whose particle size ranges from 14 to 45 μm. The parts analyzed in this study are cylinders which were printed by varying the aforementioned parameters. Figure 3.12 shows the process parameter settings which were used to print these cylinders.

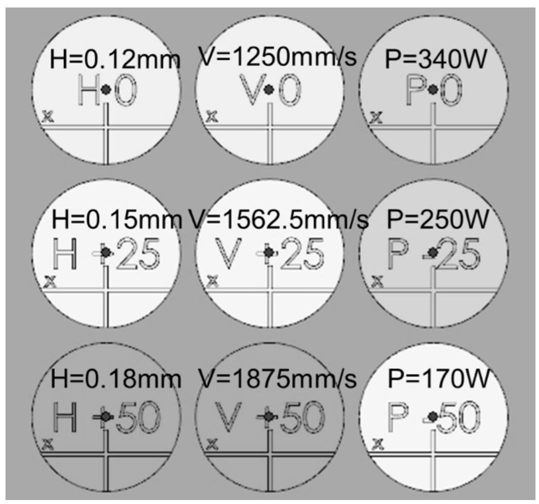

Figure 3.12. Process parameter setting of the LPBF cylinders.

As shown in Figure 3.12, hatch spacing and laser scanning velocity have been increased by 25% and 50%, (i.e., 0.12 mm, 0.15 mm and 0.18 mm for hatch spacing and 1250 mm/s, 1562.5 mm/s, and 1875 mm/s for scanning velocity), and laser power has been decreased by 25% and 50% (i.e., 340 W, 250 W, and 170 W). We collected the 3D XCT scan data of the components built in the Applied Research Laboratory at the Pennsylvania State University. The XCT scan data are analyzed to determine the effects of varying process parameters on the part quality. As the component is built layer by layer, we extract the 2D sliced images of each layer in the 3D printed cylinders. Our objective is to investigate how the change in process parameters impact the porosity levels represented by Hotelling's T^2 statistics for 2D each sliced imaging profile in each layer. Figure 3.13(a) and Figure 3.13(b) show the corresponding 3D XCT scan images and top view of the component which has a size of 25 mm in length and 10 mm in diameter.

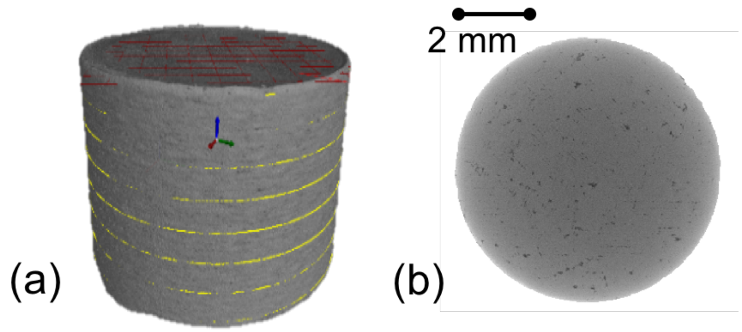

Figure 3.13. (a) 3D visualization of component XCT scan, and (b) Top view of XCT scan.

Figure 3.14 shows the multifractal spectra of 144 images under different printing conditions. It may be noted that the variations of printing conditions lead to distinct multifractal spectra. Each printing condition produces one group of multifractal spectra that are different from each other (e.g., color, range in Figure 3.14). The 50% decrease in power (i.e., $P50^{-}$) yields the most significant impact on multifractal characteristics (i.e., farthest from other groups in top right corner of Figure 3.14). This implies that higher heterogeneity exists in the layers of AM parts under this printing condition. Also, the increase in hatch spacing and velocity leads to the multifractal spectra that are different from the nominal condition (i.e., ($H0$; $V0$; $P0$)). Such experimental results show that multifractal characteristics effectively reveal hidden features in LPBF images that are strongly correlated with the variations of printing conditions. This is conducive to the quality control of 3D AM processes.

Figure 3.15 shows the lacunarity spectra of 144 XCT scan images of LPBF process. It may be noted the smaller values of lacunarity indicate more heterogeneous the images are. In other words, the increase in laser power has the most significant impact on causing more pores or defects on that layer. The second important factor in pertinent to defects in the LPBF process is the increase in hatch spacing. The joint lacunarity and multifractal results demonstrate the fact that the proposed methodology is effective to identify the defects caused by variations in printing conditions and consequently has the potential to control the system or take the correction action before the defects are extended to next layers in LPBF manufacturing

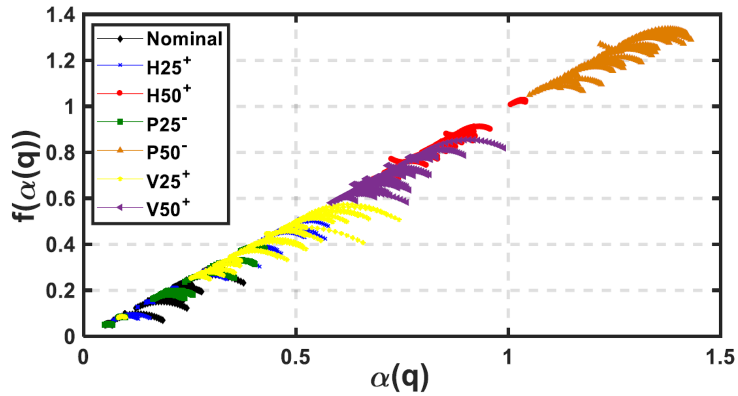

Figure 3.14. Multifractal spectra of XCT scan images of LPBF process.

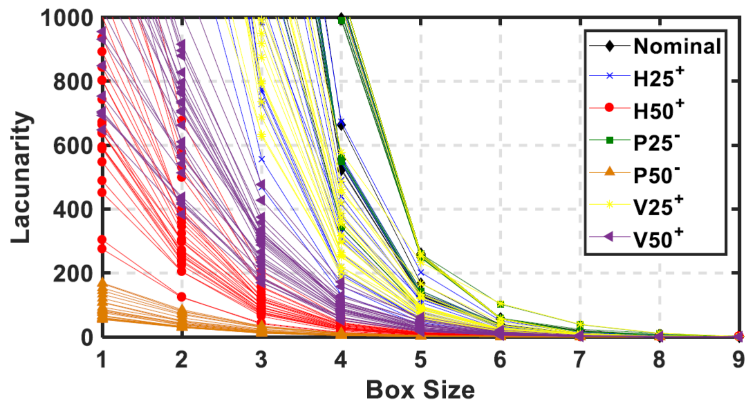

Figure 3.15. Lacunarity spectra of XCT scan images of LPBF process.

process. Further, we develop a regression model to investigate the effects of process parameters on multifractal characteristics. Here, the Hotelling's T^2 statistics is calculated based on the combined features of multifractal and lacunarity. Before the regression analysis, we use the power transformation to transform the response variable y to improve variance stabilization and reduce the heteroscedasticity:

$$z = f(y) = \begin{cases} \frac{y^\lambda - 1}{\lambda} & \lambda > 0 \\ \log y & \lambda = 0 \end{cases} \tag{3.22}$$

where y represents the Hotelling's T^2 statistic. The optimal value λ^* is selected to be -0.022 that provides the most parsimonious model with no unusual patterns in the residual plots. Based on the transformed data z, the resulted model is as follows:

$$
\begin{aligned}
Z = 11.802 - 68.77H - 0.0052P - 0.00698V + 208.82H \times H \\
+0.000015P \times P + 0.000002V \times V
\end{aligned}
\tag{3.23}
$$

Table 3.1. R-squared values for the regression model.

R-squared	R-squared (adjusted)	R-squared (predicted)
94.98%	94.76%	94.44%

The R-squared statistic is utilized to illustrate the percentage of the response variable variation that is explained by a linear model. As shown in Table 3.1, regression results show that the adjusted R-squared statistic reaches 94.76%, showing that the variations of process conditions are highly correlated with multifractal characteristics in the imaging profiles of AM builds. Note that H, P, V and H^2, V^2 and P^2 have a p-value of zero. All the parameters are significant in confidence level of 95%. In this model when we decrease the laser power, increase the scan velocity, and increase the hatch spacing from the nominal setting, Hotelling's T^2 statistics will be increased. In other words, the heterogeneity of LPBF images is increased, which indicates an increasing level of defects. Figure 3.16, normal probability plot is utilized as descriptive graphical tools to verify the underlying assumption of normality.

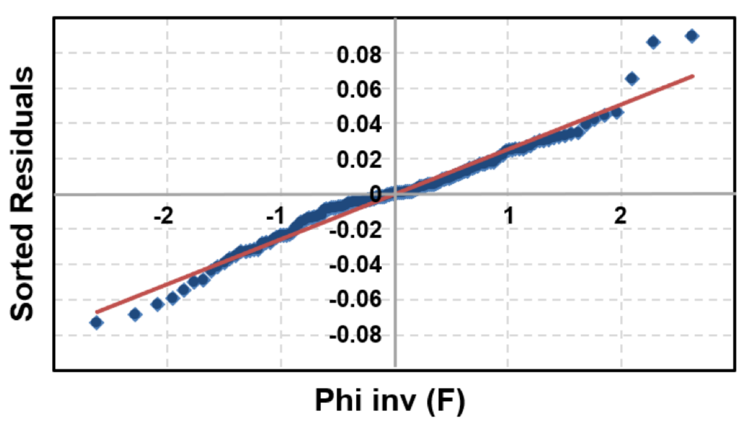

Figure 3.16. Normal probability plot for residual diagnosis of the regression model.

As is shown in Figure 3.16, the horizontal axis, i.e., phi inv (F), is the order statistic medians and vertical axis ordered residual values. Data are plotted against a theoretical normal distribution in such a way that the points should form an approximate straight line. Figure 3.16 does not show any evidence against the normality assumption.

3.5 Conclusions

Advanced imaging technology is increasingly invested to increase information visibility, thereby coping with the complexity of manufacturing processes. Massive image data provide rich information on the hidden dynamics of manufacturing processes and are conducive to improve the data-driven process monitoring and control. However, traditional statistical process control (SPC) methods are only concerned about key quality characteristics in the finished products and are less concerned about large amounts of high-dimensional images from manufacturing processes. Although image-based SPC methods have received increasing interests in past few year, very little has been done to investigate nonlinear and nonstationary of image data for the purpose of process monitoring and quality control.

This paper presents a novel methodology of multifractal and lacunarity analysis characterize and quantify image profiles from manufacturing processes (i.e., UPM and LPBF). We first extract multifractal and lacunarity characteristics from each image profile and then compute Hotelling's T^2 statistics to detect the change in the underlying process dynamics as well as identify the onset of process conditions that lead to defects. The proposed methodology is evaluated and validated with the multifractal and lacunarity methods in real-world applications in UPM and AM processes. Experimental results show that the proposed methodology captures nonlinear variations inherent to image profiles by extracting useful information from local densities and heterogeneous patterns in multiple scales, as well as converting these features to the Hotelling's T^2 statistics for process monitoring. The joint multifractal and lacunarity analysis not only effectively characterizes the surface finishes for quality control of UPM but also provides an effective predictive model to link process parameters with fractal characteristics of in-process images acquired from AM process. The proposed methodology has strong potentials to be applied for process monitoring and control of large amounts of image profiles in a variety of domains such as additive manufacturing, and biomanufacturing.

Chapter 4
Deep Learning of Variant Geometry

Deep Learning of Variant Geometry in Layerwise Imaging Profiles for Additive Manufacturing Quality Control

Abstract

Additive manufacturing is a new paradigm in design-driven build of customized products. Nonetheless, mass customization and low volume production make the AM quality assurance extremely challenging. Advanced imaging provides an unprecedented opportunity to increase information visibility, cope with the product complexity, and enable on-the-fly quality control in AM. However, in-situ images of a customized AM build show a high level of layer-to-layer geometry variation, which hampers the use of powerful image-based learning methods such as deep neural networks (DNNs) for flaw detection. Very little has been done on deep learning of variant geometry for image-guided process monitoring and control. The proposed research is aimed at filling this gap by developing a novel machine learning approach that is focused on variant geometry in each layer of the AM build, namely region of interests, for the characterization and detection of layerwise flaws. Specifically, we leverage the computer-aided design (CAD) file to perform shape-to-image registration and delineate the regions of interest in layerwise

images. Next, a hierarchical dyadic partitioning methodology is developed to split layer-to-layer regions of interest into subregions with the same number of pixels to provide freeform geometry analysis. Then, we propose a semiparametric model to characterize the complex spatial patterns in each customized subregion and boost the computational speed. Finally, a DNN model is designed to learn variant geometry in layerwise imaging profiles and detect fine-grained information of flaws. Experimental results show that the proposed deep learning methodology is highly effective to detect flaws in each layer with an accuracy of $92.50 \pm 1.03\%$**. This provides a significant opportunity to reduce interlayer variation in AM prior to completion of a build. The proposed methodology can also be generally applicable in a variety of engineering and medical domains that entail customized design, variant geometry, and image-guided process control.**

4.1 Introduction

Additive manufacturing is a process to construct customized builds layer-by-layer directly from the digital design. This expanding technology enables the creation of complex and freeform geometries that are difficult to realize using conventional manufacturing techniques [19]. AM provides a higher level of flexibility to produce builds with complex geometries and is predicted to have a market size of $50 billion by 2031 [120]. However, high quality is mandated in a large number of AM applications (e.g., biomedical and aerospace). AM mass customization poses critical challenges on existing quality control practices, which are designed for high-volume, low variability settings [15].

To cope with the complexity in AM customization, advanced imaging technology is increasingly invested in the industry. Layerwise images provide rich information on the hidden dynamics of the process and are conducive to improve the process monitoring and quality control on-the-fly. However, realizing the full potential of sensing data for quality control relies largely on the information-processing abilities [93, 121, 122]. Note that traditional machine learning methods have been utilized to detect anomalies from in-situ layerwise images in AM [1, 2, 123, 124]. These methods (e.g., K-nearest neighbor (KNN), logistic regression (Logit), support vector machine (SVM), decision tree (DT), linear discriminant analysis (LDA) and boosted trees (BT)) perform flaw detection via handcrafted statistical features that are extracted from layerwise images [33, 34]. Note that the effectiveness of these traditional methods is highly dependent on domain knowledge and features extraction.

On the other hand, deep neural networks (DNNs) show a remarkable ability for image-guided learning and detection of different anomalies autonomously. It is worth mentioning that DNNs are less dependent on domain knowledge and automatically learn spatial hierarchies of features through backpropagation by using multiple building blocks, such as convolution layers, pooling layers, and fully connected layers. There is an urgent need to develop new DNN image learning methods to tackle challenges pertinent to quality control of low-volume and high-mix production in AM. However, real-time flaw detection in AM environment poses several obstacles for DNNs:

1. **Image contrast:** Although an optical image could represent the spatial distribution of visible light emitted from each AM layer, the presence of unfused powder leads to low contrast between the fused object and the powder area. Figure 4.1 shows the in-situ layerwise images of a laser powder bed fusion (LPBF) build from three different layers. The low contrast between regions of interest (ROIs) and powder areas leads to the bias in DNN learning of incipient flaws.

2. **Layerwise geometry variation:** Layerwise geometry variation in this low-volume (even one-of-a-kind) production limits the number of potential training images for a given build. If a cropped squared region is used for all layers, then some layers will have small ROIs and large powder areas while others have large ROIs and small powder areas. As a result, the DNN learning of cropped squared regions is highly biased due to inconsistent ROIs from one layer to another. As shown in Figure 4.1, ROIs have a variety of different geometries throughout the build which challenge the realization of DNNs for process monitoring and control in AM.

3. **Spatial characterization:** Statistical features captured from layerwise AM image (i.e., mean, median, variance, etc.) aggregate the surface information. Consequently, flaw detection based on these features causes a deficiency in

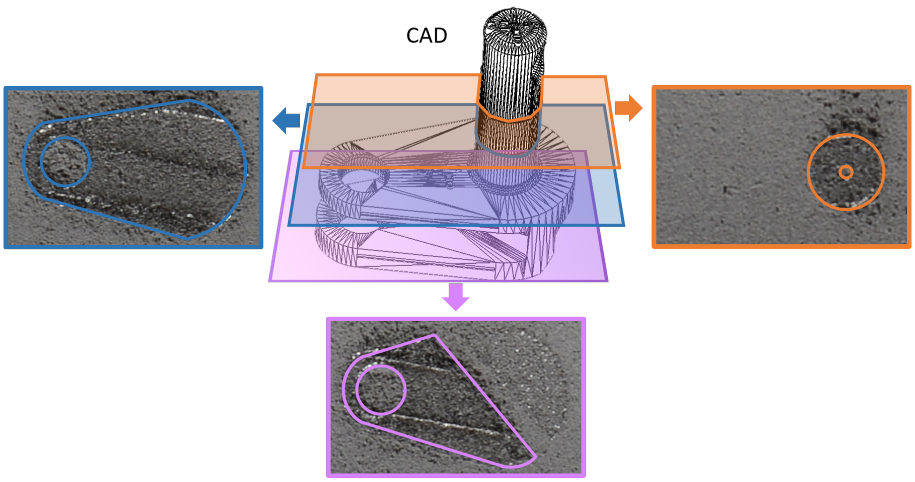

Figure 4.1. An example of in-situ images between the fused object and the powder area as well as high-level of layer-by-layer regional variation in the LPBF process.

surface characterization and inaccuracy in prediction. On the other hand, flaw detection via raw image profiles with inherent complex structure leads to the curse of dimensionality and incurs a great computational overload on real-time quality control. There is a dire need to develop new spatial characterization algorithms for flaw detection in AM.

The present research investigation is aimed at filling these gaps by developing a novel deep learning approach that is tailored for low-volume and highly-customized production in AM. Specifically, our contributions are as follows:

1. **Layerwise ROI estimation:** We leverage the computer-aided design (CAD) file to perform shape-to-image registration and delineate ROIs in layerwise AM image profiles.

2. **Freeform geometry analysis:** Each layerwise ROI is partitioned into a number of subregions of interest (sROIs) to tackle the problem of varying cross-sectional geometries. Also, the hierarchical dyadic scaling method is developed to provide fine-grained information about the location of flaws.

3. **Spatial characterization of sROIs:** Each sROI consists of the same number of pixels, but in different shapes. Spatial characterization provides critical information on spatial patterns in the distribution of pixels in each sROI. Note that the profiles of sROI spatial characterization are consistent in the

dimensionality and thus avoid the bias in the learning of cropped squared regions in raw image profiles (as discussed previously).

4. **DNN learning of incipient flaws:** Hence, the profiles of spatial characterization are used as input data to the DNN model. We developed the customized DNN model to extract the underlying flaws hidden in the spatial representation of sROIs and ROIs. Several convolutional layers will be used to learn representations of images with multiple levels of abstraction.

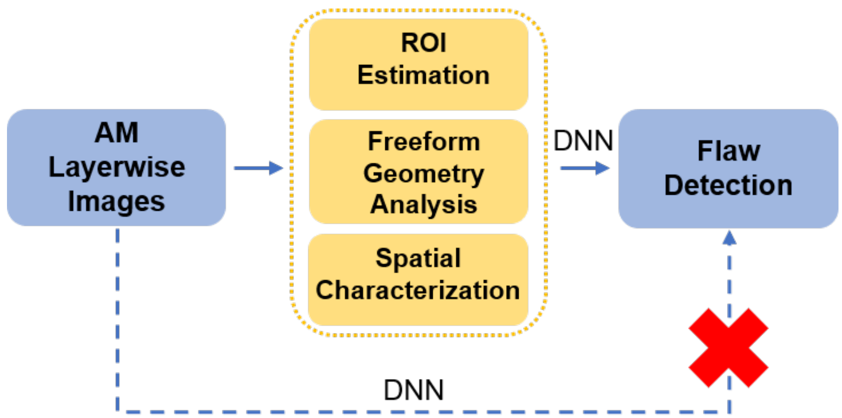

Figure 4.2. The challenges to implement DNN directly on layerwise images include variable ROIs, layerwise geometry variation, and spatial characterization of sROIs, which call upon the development of new deep learning methods for low-volume and highly-customized production in AM.

New DNNs have advantages over traditional machine learning methods, but the worst scenario is to just "feed images of layers" (i.e., with variant geometries) to a neural network and then "let artificial intelligence (AI) figure it out", given the broad geometrical diversity of images from any number of builds made with AM. As shown in Figure 4.2, it is practically impossible to learn layerwise images directly using the DNN because the ROI is not delineated and the geometry varies from layer-to-layer in a customized build. After all, it is not desirable to use the DNN to learn the cropped square region in an image that contains both ROIs and the unfused powder outside the ROIs. We evaluate and validate the proposed methodology with a real-world case study on the drag link joint part with intentional flaws and complex geometry from the LPBF machine (see details in the section of experimental design and materials). Layerwise images are collected during the fabrication of parts with a DSLR camera that is installed in the chamber of LPBF machine. In the case study, we focus on the lack of fusion flaws a common type of flaws in LPBF, but the proposed methodology shows strong potentials to be generally applicable to other flaws (e.g., surface contaminations and super-elevated edges). Note that image-guided process monitoring is the next vertical step to mitigate scrap and rework rates, and further ensure the economic viability of AM.

This paper is organized as follows: Section 2 provides a literature review on the current monitoring for AM. Section 3 proposes a methodology to develop real-time in-situ monitoring in AM. Section 4 covers the experimental design and materials for this study. Section 5 shows the experimental results for the drag link joint part. Finally, we conclude this paper by highlighting the limitations of the current image-guided monitoring for AM quality control and provide an overview of the proposed methodology.

4.2 Research Background

There has been an extensive body of researches investigating process monitoring and control in AM. Note that monitoring of metal AM has received great attention owing to its widespread applications as well as its critical quality problem. A comprehensive review of sensor-based process monitoring with the focus on metal AM processes are provided in Tapia and Elwany [53], Foster [60], Everton et al. [24], Mani et al. [52], and Grasso and Colosimo [27].

4.2.1 Sensor-based Monitoring in AM Processes

Heterogeneous sensors are integrated with AM machines to detect interior flaws (e.g., cracking, porosity, layer delamination, surface finish and geometric distortion) and provide a significant opportunity to reduce inter-layer variation in an AM build [82]. Powder bed fusion (PBF) and directed energy deposition (DED) are the two popular AM processes that utilize thermal energy to fuse powder. As a result, numerous studies have focused on gauging heat radiation of melt pools via photodetectors, photodiodes and thermocouple for process monitoring in AM [27, 48, 125, 126]. On the other hand, proximity sensors operate based on the time that takes for a signal to be sent, hit and return to a receiver. Numerous studies have utilized proximity sensors to monitor the layer thickness during the build process [127]. For instance, Cheng et al. [128] implemented laser flash sensors on the LPBF process to measure the thermal diffusivity and the normalized temperature history during the experiment. Also, ultrasonic sensors have implemented to detect changes in porosity in metal builds during fabrication on a PBF and laser powder deposition (LPD) processes [129].

Among different type of sensors, optical cameras have been largely adopted in studies because they are capable of realizing the real-time, precise and low-cost monitoring [130]. These optical cameras have one of following technologies: CCD, in which all of the signals related to pixels are processed by a unit circuit in a camera, or complementary metal oxide semiconductor (CMOS), where every pixel has a separate processing circuit. Note that CMOS is less expensive but leads to the high-noise images [24]. Chivel and Smurov [75] utilized a CCD camera integrated with a single spot sensor-pyrometer according to photodiodes for process monitoring. Bayle and Doubenskaia et al. [131] implemented an analogous setup with an infrared (IR) camera and a pyrometer on an LPBF machine. Kleszczynski et al. [64] presented a system for error detection using a CCD camera installed outside the build chamber. Heigel and Lane [78] measured the length of melt pool during the single-track laser scan in DED process using a high-speed infrared camera. Mahmudi et al. [132] used a high-speed thermal imaging to capture the temperature of the melt pool in the LPBF process.

Kruth et al. [133,134] developed a feedback control system using a coaxial optical monitoring system CMOS camera and a photodiode to monitor and measure the geometry of the melt pool area. However, the system was not capable of capturing images with a high sample rate, and therefore the melt pool dynamics were not characterized effectively. The optical system was upgraded by Clijsters et al. [135]. They leveraged a high-speed near-infrared thermal CMOS camera and a photodiode optical system linked to a programmable gate array. Seifi et al. [136] leveraged a co-axial pyrometer camera to capture melt pools and an infrared camera to capture the global heat flow in the DED process. Craeghs et al. [76, 77] introduced a real-time optical process monitoring system for the layerwise laser melting (LLM) process by instantaneously mapping the melt pool data with a relative position on the printing plane. Recently, researchers at The Pennsylvania State University (PSU) have examined the use of inexpensive optical imaging to perform layerwise in-situ monitoring of AM. For example, Imani et al. [2, 33, 34], Chen et al. [137]

and Yao et al. [35, 93] utilized layerwise optical images taken from melt pool of LPBF machine to characterize flaws and quantify the impact of design and process parameters on the quality of builds.

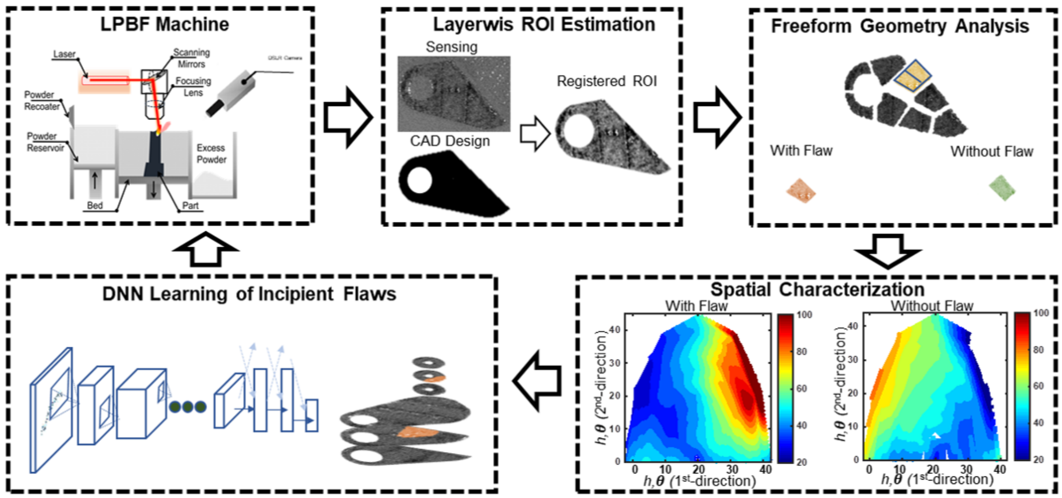

Figure 4.3. Flow diagram of the research methodology.

4.2.2 Gaps in In-situ Optical Process Monitoring

In-situ optical imaging is a prudent alternative for process monitoring to tackle challenges for quality control of low-volume and high-mix production in AM. However, realizing the full potential of sensing data for quality control relies largely on the information-processing capabilities [35, 93]. Traditional machine learning methods (e.g., KNN, SVM and DT) have been utilized to detect anomalies from layerwise images [1, 123, 124, 138, 139]. AM anomalies are detected through handmade of statistical features extracted from layerwise images. However, design and extraction of sensitive features depend to a great extent on the domain knowledge. In other words, the performance of traditional machine learning methods for anomaly detection is highly correlated to the effectiveness of handcrafted feature extraction.

On the other hand, DNNs automatically learn features from images and represent them hierarchically in multiple levels. Sun et al. [140] developed a system that employs a neural network to find thermal fusion flaws. Librantz et al. [141] implemented this method to improve the inspection ability in plastic mold surfaces of AM. Zhang et al. [142] leveraged SVM and convolutional neural networks (CNN) for quality level identification in PBF. Kwon et al. [143] applied a DNN to categorize melt pool images of SLM regarding the laser power. Scime and Beuth [18] used a CNN for autonomous anomaly detection related to flaws caused by perturbations in LPBF. However, there are critical challenges that hamper DNNs from learning the critical features including low image contrast, layer-to-layer ROI variation and complexity of the surface. There is an urgent need to develop new DNN methods for real-time process monitoring and control in AM environment.

4.3 Research Methodology

This section presents the proposed methodology of deep learning of variant geometry for layerwise image-guided quality control in AM. As shown in Figure 5.1, our methodology is divided into the following steps: 1) layerwise ROI estimation, 2) freeform geometry analysis by hierarchical dyadic partitioning, 3) spatial characterization, and 4) DNN learning of incipient flaws. Here, multiple DNN convolution layers are utilized to learn multiple levels of abstraction for automatic feature leaning and extraction. Layerwise AM quality control is an indispensable step to mitigate scrap and rework rates, and further promote the widespread application of AM.

A DSLR camera (i.e., Nikon D800E) with resolution 36.3 megapixel resolution (i.e., 7360 $\times$ 4912 pixels) captures layerwise image profiles of powder bed . We also utilize a Phoenix industrial high-resolution CT & X-ray system for post-build inspection. The camera shutter is controlled by a proximity sensor which reads the location of the re-coater blade, and then the powder bed images are taken under the bright-field flash setting. The layout of the advanced imaging system that is integrated with the LPBF machine as well as the final drag link joint build are shown in Figure 4.4 (a) and Figure 4.4 (b), respectively. Figure 5.5 illustrates an in-situ layerwise image of the build plate along with the part of interest (i.e., the rectangular region with red border).

4.3.1 Layerwise ROI Estimation

The objective of layerwise ROI estimation is two-folded. First, it is aimed at confirming an image to ground truth (i.e., CAD file) and removing any biases that are created in images due to the camera settings. Second, by masking the

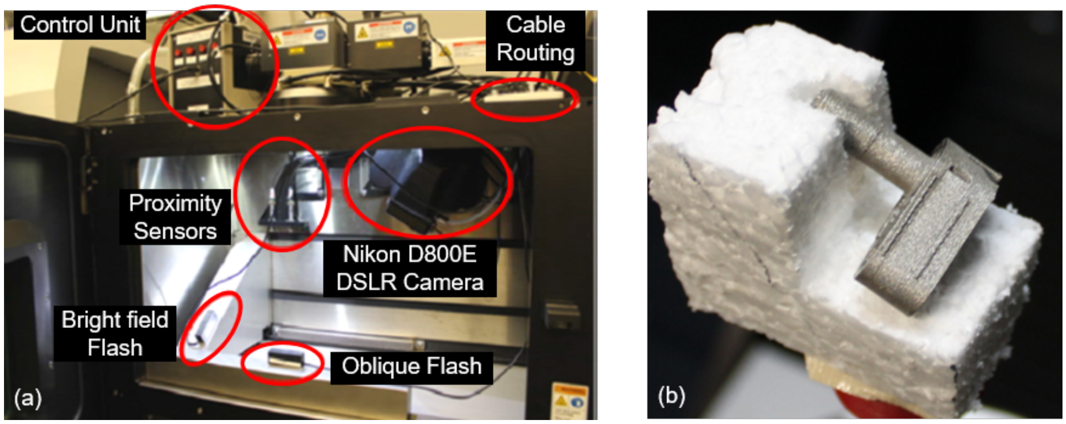

Figure 4.4. (a) The advanced imaging system installed in the LPBF machine at PSU, and (b) final build of the drag link joint.

Figure 4.5. The layerwise in-situ image of build plate with DSLR camera in the LPBF machine [2].

image against the CAD slice for each respective layer, we isolate ROI from the surrounding region of the powder bed.

It is worth mentioning that the build geometries can change drastically layer to layer, which makes it difficult to use pre-defined landmarks to perform one-time registration. However, the shape-to-image registration between sliced CAD file and layerwise images leads to the robust and accurate ROI estimation, because this is a one-to-one mapping to original engineering designs.

In-situ images were cropped at the same location and then histogram equalization method is considered to enhance edge contrast. Assume that an AM build consists of the L layerwise images where $\mathbf{x}$ shows the image domain. The i^{th} pixel locations in the l^{th} layerwise image is denoted by $\mathbf{x}_i^{(l)} \in \mathbb{R}^2 \; \forall i = 1, ..., N^{(l)}$ where $N^{(l)}$ is the total number of the pixels in layer l. Also, $\mathbf{y}$ represents the gray level (GL) image intensities with the range $[0, R-1]$. The probability density function (PDF) for image l is approximated as:

$$P^{(l)}(r) = \frac{n_r^{(l)}}{N^{(l)}} \quad \forall \, r = 0, 1, ..., R-1 \tag{4.1}$$

where $n_r^{(l)}$ is the number of pixels in the image which their GL is r. The cumulative density function (CDF) of the image is defined as:

$$F^{(l)}(r) = \sum_{m=0}^{r} P^{(l)}(m) \quad \forall \, r = 0, 1, ..., R-1 \tag{4.2}$$

Histogram equalization maps an input with GL r into the output $O_r^{(l)}$ using the CDF values:

$$O_r^{(l)} = (R-1) \times F^{(l)}(r) \tag{4.3}$$

The increase in output level $O_r^{(l)}$ is computed as:

$$\Delta O_r^{(l)} = (R-1) \times P^{(l)}(r) \tag{4.4}$$

Eq. (4.4) shows that $O_r^{(l)}$ is proportional to the probability of its level. For better performance, $P^{(l)}(r)$ in Eq. (4.4) is substituted by $P_{wt}^{(l)}(r)$ via the method of weighted thresholded enhancement as follows:

$$P_{wt}^{(l)}(r) = \begin{cases} P_u^{(l)} & if \; P^{(l)}(r) > P_u^{(l)} \\ (\frac{P^{(l)}(r) - P_l^{(l)}}{P_u^{(l)} - P_l^{(l)}})^k \times P_u & if \; P_l^{(l)} \leq P^{(l)}(r) \leq P_u^{(l)} \\ 0 & if \; P^{(l)}(r) < P_l^{(l)} \end{cases} \tag{4.5}$$

where $P_{wt}^{(l)}(r)$ transforms all values between the upper threshold $P_u^{(l)}$ and lower threshold $P_l^{(l)}$ using power law function with index k. After obtaining the PDF of weighted thresholded from Eq. (4.5), the CDF and level mapping function are estimated respectively as:

$$F_{wt}^{(l)}(r) = \sum_{m=0}^{r} P_{wt}^{(l)}(m) \quad \forall\, r = 0, 1, ..., R-1 \tag{4.6}$$

$$\tilde{\mathbf{y}}(\mathbf{x}_i^{(l)}) = W_{out}^{(l)} \times F_{wt}^{(l)}(\mathbf{y}(\mathbf{x}_i^{(l)}) + M_{adj}^{(l)} \tag{4.7}$$

where $W_{out}^{(l)}$ is the dynamic range of the output image, and $M_{adj}^{(l)}$ is the mean adjustment factor which compensates for the change of mean luminance level after enhancement.

After adjusting the contrast, shape to image registration method is utilized to perform an initial segmentation of the build area from enhanced images. The objective of image registration is to find the point-to-point correspondence between two images (i.e., a moving image and a fixed image) using a common coordinate system. Note that we shift the moving image towards the fixed image. The registration process involves four components, namely similarity metric, optimizer, moving transformation, and interpolator. The similarity metric is aimed at evaluating the accuracy of the image registration. It takes two images (i.e., the moving image and the fixed image) and returns a scalar value that measures the similarity between the two images. Note that the similarity metric is also named as the cost function in some literature. Here, the similarity is defined as a function of the pixel values in images. The optimizer specifies the searching strategy, and we utilized step gradient descent as our optimization policy. The interpolator maps the pixel intensities to the new coordinate system based on the moving transformation, and measures the difference between the intensity values. Note that we utilized bi-linear interpolation in our research study. Figure 4.6 illustrates this iterative process which obtains the moving transformation that optimizes the similarity metric when applied to the moving image.

We utilize the mean square differences ($\mathcal{D}$) to define the similarity metric in this research study. For a fixed image $\acute{\mathbf{y}}(\mathbf{x}^{(l)})$ and a transformed image $\tilde{\mathbf{y}}(\mathbf{x}^{(l)})$, $\mathcal{D}$ is formulated as:

$$\mathcal{D}(\acute{\mathbf{y}}, \tilde{\mathbf{y}}) = \frac{1}{N_{ROI}^{(l)}} \sum_{i=1}^{N_{ROI}^{(l)}} \|\acute{\mathbf{y}}(\mathbf{x}_i^{(l)}) - \tilde{\mathbf{y}}(\mathbf{x}_i^{(l)})\|^2 \quad \forall\, \mathbf{x}_i^{(l)} \in \acute{\mathbf{y}} \cap \tilde{\mathbf{y}} \tag{4.8}$$

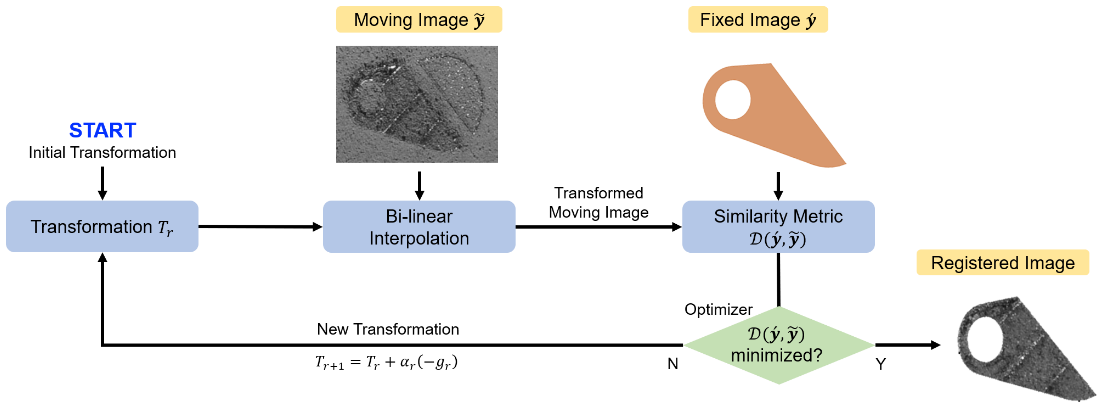

Figure 4.6. The flow chart of image registration.

where $N_{ROI}^{(l)}$ represents the number of pixels in each image, $\acute{\mathbf{y}}(\mathbf{x}^{(l)})$ shows the intensity of pixel $\mathbf{x}_i^{(l)}$ in the fixed image, $\tilde{\mathbf{y}}(\mathbf{x}^{(l)}))$ denotes intensity of pixel $\mathbf{x}_i^{(l)}$ in the transformed image. $\acute{\mathbf{y}}$ is formulated as:

$$\tilde{\mathbf{y}} = T_r(\tilde{\mathbf{y}}(\mathbf{x}^{(l)})) \tag{4.9}$$

where T is the transformation function. We want to find T that minimizes $\mathcal{D}(\acute{\mathbf{y}}, \tilde{\mathbf{y}})$. The optimization problem is formulated as (6).:

$$argmin_T \, \mathcal{D}(\acute{\mathbf{y}}, \tilde{\mathbf{y}}) \tag{4.10}$$

We utilized the gradient descent to calculate T and reach to the minimum value of $\mathcal{D}$:

$$T_{r+1} = T_r + a_r(-g_r) \tag{4.11}$$

where $a_r > 0$ is the step size at iteration r, g_r is the gradient vector of $\mathcal{D}$ at iteration r. The iteration terminates when $\mathcal{D}$ reaches within a threshold of its minimum value.

Then, we isolate the ROI of layer l from the powder area in the registered image by defining a Heaviside function on each pixels of the CAD slice of layer l and excluding the pixel information of powder area by assigning the value 0 to them.

4.3.2 Freeform Geometry Analysis

Due to ROI variations from one layer to another, a standalone DNN is incapable of extracting helpful features directly from layerwise images. ROI partitioning is required to split an ROI into sROIs with the same number of pixels and remove the dependency on layerwise geometries. In addition, sROI analysis approximately determines the location of flaws in layerwise images. Therefore, ROIs are partitioned into a number of discrete segments using the Lloyd's algorithm [144]. We assume that $\mathbf{x}_i^{(l)}\ \forall i = 1, ..., N_{ROI}^{(l)}$ is the i^{th} pixel location in the ROI of image l and $N_{ROI}^{(l)}$ is the total number of the pixels in the region. Given the pixel's location $\mathbf{x}_i^l$ and integer $K^{(l)}$, the algorithm finds $K^{(l)}$ points $C_1, ..., C_{K^{(l)}} \in \mathbb{R}^2$ which minimizes the following clustering error:

$$F_{KM}(C_1, ..., C_{K^{(l)}}) = \sum_i \min_k \left\|\mathbf{x}_i^{(l)} - C_k\right\|^2 \tag{4.12}$$

The clustering error $F_{KM}(C_1, ..., C_{K^{(l)}})$ is the squared distance between all pixels and their closest centroids.

Algorithm 1 Freeform geometry analysis

input: $C_1, ..., C_{K^{(l)}} \leftarrow$ place centroids at regular intervals

while objective function still improves **do**
 $S_1, ..., S_{K^{(l)}} \leftarrow \phi$
 for $i \in 1, ..., N_{ROI}^{(l)}$
  $k \leftarrow argmin_k \|x_i^{(l)} - C_k\|^2$
  add i to S_k
 end for
 for $k \in 1, ..., K^{(l)}$ **do**
  $C_k = \frac{1}{|S_k|} \sum_{i \in S_k} x_i^{(l)}$
 end for
end while

As shown in Algorithm 2, S_k presents the set of pixels in ROI of the layer l to which C_k is the nearest centroid. The set cluster centers are initiated at the beginning. In our images, cluster centers were placed at regular intervals within an ROI and partitioned into $K^{(l)}$ sROIs (masks) of roughly equal size (number of pixels). Assume that C is the center of a set of pixels S. Then, moving the center C to $\frac{1}{|S|} \sum_{i \in S} x_i$ occurs if there is reduction in clustering error. The number of clusters for a given layer geometry is a function of the size of the ROI (i.e., the larger the region, the greater the value of K). In order to optimize the choice of the value K, ROI partitioning in each layer is performed based on the relative sizes of a given layer and the smallest ROI. For layer l with $N_{ROI}^{(l)} \quad \forall l = 1, ..., L$ number of pixels, the number of sROIs is defined as:

$$K^{(l)} = \frac{N_{ROI}^{(l)}}{gcd(N_{ROI}^{(l))}, min(N_{ROI}^{(l))}))} \quad \forall\, l = 1, ..., L \tag{4.13}$$

where $gcd(.)$ is the greatest common divisor. For example, if the smallest ROI has 4000 pixels and the largest ROI includes 50000 pixels, then the $gcd(4000, 50000) = 2000$. As a result, the number of partitions will be 2 and 25 for the smallest and largest ROIs, respectively. Then, each sROI of the drag link joint is dyadically partitioned. The partitioning step has two main benefits:

1. By isolating flaws to the same cluster, the features that are extracted by the DNN are much more pronounced. For instance, given the pre-processing methodology, the DNN will more efficiently detect the significant pixel intensity gradients that are characteristic of flaws.

2. From a practitioner's perspective, if the DNN model predicts that a given partition contains a flaw, the classification not only keeps track of which layers are problematic, but it also identifies which sROI within the layer contains the potential flaw.

Thus, the hierarchical dyadic partitioning allows for extraction of useful spatial information about the location of flaws.

4.3.3 Spatial Characterization of sROIs

DNN process monitoring and control without characterized sROIs creates the following challenges:

1. The inspection results of AM layerwise images show that intensities in flaw locations are lighter than the surrounding nominal material. Previous methods have utilized this fact through traditional thresholding and intensity gradient methods to highlight potential flaws [1]. However, in a real-life case study,

there are also lighter areas around the edges of the part due to various factors, including the flash location, effect of the hatch/contour interface at the edge of a build, or stochastic powder buildup in these areas. In other words, robust methods cannot simply rely on pixel intensities to identify flaws.

2. DNN directly learns features from sROIs. Hence, the shape of sROIs is one of the important factors that influence learning. In other words, DNN without spatial characterization may be impacted more by the shape of sROIs instead of flaw occurrences, thereby creating a bias in prediction.

We propose a semiparametric model to characterize sROI in AM, which has two main benefits:

1. Spatial characterization extracts useful information from sROIs and provides characteristics of spatial patterns in each sROI.

2. DNN cannot directly use sROIs with different shapes and geometries as the input. Spatial characterization consolidates variant shapes into spatial-characterization images of the same size. The spatial characterization images can then be fed into DNNs for learning incipient flaws.

It is worth mentioning that semiparametric models (e.g., Gaussian mixture model and ordinary Kriging) are more robust than parametric models (e.g. spline and inverse distance weighted methods). Also, due to the lower number of parameters, these semiparametric models are calculated rapidly. A semivariogram is commonly used to display the variability between pixels in an image as a function of distance [145]. In the LPBF process, due to the impact of machine parameters (e.g., laser direction, hatch spacing and distance from the center of the build plate), spatial characterization can be dissimilar along with different directions. Therefore, we leverage the anisotropic semivariogram model, which is the function of distance and direction as follows:

$$\gamma_{(k)}^{(l)}(h,\boldsymbol{\theta}) = \frac{1}{2}\ E[\{Y(\mathbf{x}_{(k)}^{(l)}) - Y(\mathbf{x}_{(k)}^{(l)} + h, \boldsymbol{\theta})\}^2] \tag{4.14}$$

where $\gamma_{(k)}^{(l)}(h,\boldsymbol{\theta})$ represents the semivariogram of two random pixels in the layerwise image l and subregion k with the lag distance h and angle $\boldsymbol{\theta}$. The superscript is the layer number and the subscript denotes the subregion defined in freeform geometry analysis. $Y(\mathbf{x}_{(k)}^{(l)})$ is the variable representing pixel intensity at $\mathbf{x}_{(k)}^{(l)}$ and $Y(\mathbf{x}_{(k)}^{(l)}+h, \boldsymbol{\theta})$ shows the pixel intensity at a lag distance h and angel $\boldsymbol{\theta}$ from $\mathbf{x}_{(k)}^{(l)}$. The anisotropic semivariogram illustrates these values in two dimensions and extracts sROIs' spatial characteristics. The value of $\gamma_{(k)}^{(l)}(h, \boldsymbol{\theta})$ in Eq. (4.14) is estimated as:

$$\hat{\gamma}_{(k)}^{(l)}(h, \theta) = \frac{1}{2N(h, \theta)} \sum_{i=1}^{N(h,\theta)} [\mathbf{y}(\mathbf{x}_{i(k)}^{(l)}) - \mathbf{y}(\mathbf{x}_{i(k)}^{(l)} + h, \theta)]^2 \tag{4.15}$$

where $N(h, \theta)$ is the total number of pixel pairs separated by a specific lag h in the angles along pixel $\mathbf{x}_{i(k)}^{(l)}$ and $\mathbf{x}_{i(k)}^{(l)} + h$. In our experiment, θ takes two angels which are orthogonal to each other. Qualitatively, these plots performed relevant analysis that identified steep intensity gradients and related them to location, capturing information about the problematic areas around the edge of the build. For the purposes of the DNN prediction, by moving our dataset from a pure image space to a more normalized realm, we can help avoid overfitting to the wrong data set during training.

4.3.4 DNN Learning of sROIs in Layerwise Image Profiles for Detection of Incipient Flaws

High-dimensional sensing data (e.g., image profiles) provide rich information about underlying processes but pose significant challenges on the efficient representation of the flaw in each layer of AM build. We propose the DNN to learn and represent incipient flaws from sROIs in layerwise images collected from the AM process. As shown in Figure 4.7, the input to the DNN consists of large amounts of images resulting from the spatial characterization of individual sROIs. We chose our pillar DNN structure based on AlexNet, which includes 5 convolutional layers (comprising the vast majority of the computational effort) and 3 fully connected layers [146, 147]. The rationale to choose AlexNet is as follows:

1. **Image learning:** AlexNet is designed to learn various patterns from 2-dimensional images in comparison with other neural network methods.

2. **Transferability:** It is constructed to offer a higher level of flexibility for transfer learning, which helps take advantage of prior knowledge on image patterns to learn incipient flaws in layerwise AM images.

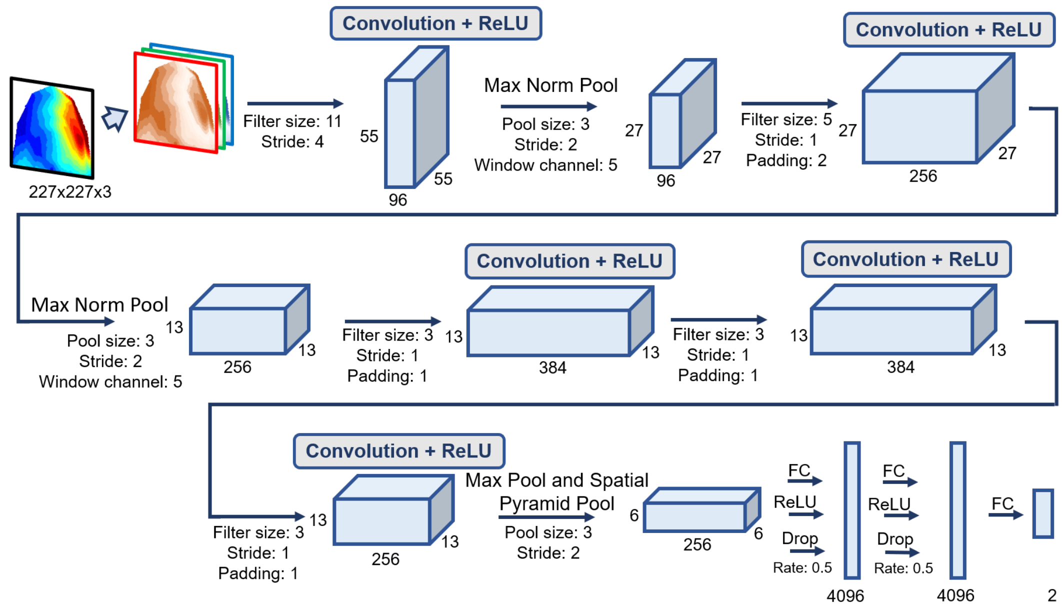

Figure 4.7. The flowchart of the deep neural network employed to detect flaws from spatial characterization of multiscale subregion of interests.

Note that we are able to perform DNN learning of incipient flaws for two main reasons. First, we perform freeform geometry analysis in multiple scales, which decomposes each ROI into the multiple sROIs. Further, the dyadic partitioning of sROIs splits each region into smaller subregions and provides a large amount of data for DNN learning. Second, we leverage the transfer learning, which exploits what has been learned in the DNN model to improve generalization. In other words, image learning does not start from ground zero but rather utilize prior knowledge and thus circumvent the need for enormous dataset for the image learning tasks. For example, the drag link joint build in this study consists of 362 ROIs. Partitioning of ROIs with freeform geometry analysis generates 1,708 sROIs. These sROIs are spatially characterized and used as inputs into the pre-trained DNN structure for incremental learning of incipient flaws.

Rectified linear units (ReLUs) are utilized to account for the significant non-linearity in complex images and greatly decrease training time compared to tanh-based neurons [148]. ReLUs have desirable properties such as better gradient propagation, sparse activation, and efficient computation. To prevent overfitting, incorporating the estimations of various models is an effective way to decrease test errors, but this action is computationally expensive. Dropout is an efficient version of model combination that is not computationally expensive. This regularization technique shrinks overfitting in DNN by precluding complex co-adaptations on training data. The neurons which are "dropped out" do not contribute to the forward pass and backpropagation. Note that each time an input is provided, the neural network samples a dissimilar architecture, although all of these architectures share weights. Therefore, the model only learns the most relevant features, leading to increased robustness.

Assume that the input sample $\Gamma = \{\hat{\gamma}_{(1)}^{(1)}(l,\theta), ..., \hat{\gamma}_{(K^{(L)})}^{(L)}(l,\theta)\}$ denotes the characterized image of the all sROI for L layers. $z_{(k)}^{(l)} \in \{1,2\}$ represents the associated true label for sample $\hat{\gamma}_{(k)}^{(l)}(h,\theta)$. Assume that the number of layers in pre-trained DNN is P, also we have weight combinations $\mathbf{\Psi} = (\Psi^1, ..., \Psi^P)$ for the DNN. Let $\boldsymbol{\psi} = (\psi^1, ..., \psi^{P-1})$ denotes the associated weights for each classifier in each hidden layer of the pre-trained DNN. The linkage between the weight parameters and the filters are formulated in Eq. (4.16) and Eq. (4.17), respectively as:

$$Z^p = f(Q^p) \tag{4.16}$$

$$Q^p = \psi^p \times Z^{p-1} \tag{4.17}$$

where P and p represent the total number of layers and the index for specific layer in the pre-trained DNN. Also, $\psi^p, p = 1, ..., P$ are the network weights that need to be learned; Q^p denotes the convoluted responses on the last feature map; and f denotes the pooling function on Q. Therefore, we have a total cost function for this pre-trained DNN as follows:

$$S(\mathbf{\Psi}) = R(\mathbf{\Psi}) + Q(\mathbf{\Psi}) \tag{4.18}$$

where $R(\mathbf{\Psi})$ is the output objective and $Q(\mathbf{\Psi})$ is the summed companion objective, which are respectively written as:

$$R(\mathbf{\Psi}) = \|\psi^{out}\|^2 + L(\mathbf{\Psi}, \psi^{out}) \tag{4.19}$$

$$Q(\mathbf{\Psi}) = \sum_{p=1}^{P-1} [\|\psi^p\|^2 + l(\mathbf{\Psi}, \psi^p) - r] \tag{4.20}$$

where $\|\psi^{out}\|^2$ is the norm classifier weight of the output layer and $L(\mathbf{\Psi}, \psi^{out})$ is the squared hinge loss function for output layer. Also, $\|\psi^p\|^2$ and $l(\mathbf{\Psi}, \psi^p)$ are the margin and squared hinge loss function in each hidden layer. These hinge functions can be written as follows:

$$L(\mathbf{\Psi}, \psi^{out}) = \sum_{l,m} [1- < \psi^{out}, f(Z^p, z^1) - f(Z^p, z^1) >] \tag{4.21}$$

$$l(\mathbf{\Psi}, \psi^{p}) = \sum_{l,m} [1- < \psi^{p}, f(Z^p, z^1) - f(Z^p, z^1) >] \tag{4.22}$$

We can write the final objective of pre-trained DNN as:

$$S(\mathbf{\Psi}) = \|\psi^{out}\|^2 + \sum_{p=1}^{P} \phi_p \times [\|\psi^{out}\|^2 + l(\mathbf{\Psi}, \psi^p) - r] \tag{4.23}$$

The pre-trained DNN is capable of learning the convolutional kernels Ψ^* as well as forcing a constraint at each hidden layer to create a good label prediction. Therefore, it leads to a powerful driving force for having discriminative features at each layer. The next term usually has a zero value during the training the DNN. It is worth mentioning that the optimization procedure is conducted using the stochastic gradient descent (SGD) algorithm.

$$\mathbf{\Psi} = \mathbf{\Psi} - \eta \nabla S(\mathbf{\Psi}) \tag{4.24}$$

where η is the learning rate. While the original method was trained on millions of training images in 1000 categories, we adopted this structure to support a binary (flawed or nominal) classification trained on the anisotropic semivariograms produced of each sROI. We trained our models using SGD, the momentum γ of 0.9, and weight decay (η) of 0.0005. We train the network on GPU with 2GB NVIDIA Quadro 4000 and 256 parallel processing CUDA Cores configuration.

In this study, the bootstrapping method is investigated to decrease the bias of the DNN model. In the classification problem of AM builds with optimized machine parameters, the size of classes is not usually equal i.e., 303 without flaws and 59 with flaws. Common classification methods try to maximize the overall prediction accuracy assuming that each class has sufficient cases in the training dataset. As a result, for highly imbalanced datasets, classification methods lean toward the majority class and relatively neglect the minority class (which in this case represents the flawed sROIs). Therefore, the bootstrapping method is utilized to sample randomly and replace images from the dataset to reconstruct the balanced datasets.

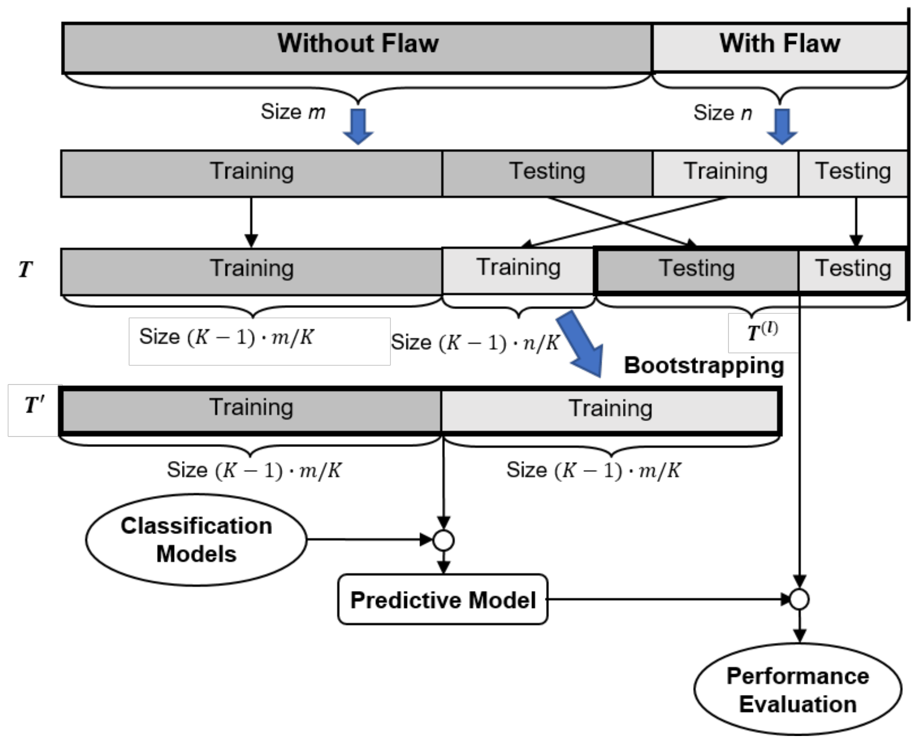

Figure 4.8. The diagram of cross-validation and boostrapping in the proposed methodology.

As shown in Figure 4.8, our dataset includes m without flaw and n with flaw recordings ($m > n$). The splitting ratio (i.e., $(K-1)$ training folds vs. 1 validation fold) is the same for without flaw and with flaw groups. Furthermore, a balanced training set T is remade with the use of the bootstrapping method. The group with the flaw is enlarged to yield the same size as the nominal group in the new training set T'.

4.4 Experimental Design and Materials

Experiments were performed on an EOSINT M 280 LPBF machine. The material was a Titanium alloy, Ti-6Al-4V also known as ASTM B348 Grade 23 powder material which has a particle size between 14 μm to 45 μm. The LPBF machine experimental setting is shown in Table 4.1.

Table 4.1. LPBF machine parameters setting for fabrication of the drag link joint build

Print Parameters	Value
Laser Power	340 W
Scan Speed	1250 mm/s
Hatching Distance	0.12 mm
Layer Thickness	60 μm

The drag link joint build has an enclosing box dimension of 23.7 mm $\times$ 13.3 mm $\times$ 27.3 mm, with the 60 μm layer thickness. Note that 362 layerwise images were collected with the optical system. Intentional flaws were embedded in the build at four different locations along the build-up direction that is intersected with cubical and cylindrical patterns. Figure 5.12 illustrates locations (i.e., 8 defects per location) inside the drag link joint build. Objects within the defect pattern consist of 50 μm, 250 μm, 500 μm, and 750 μm cubes which are centered in z plane direction. Cylindrical flaws with the diameter of 50 μm, 250 μm, 500 μm, and 750 μm are also placed in the part. Here, all cylindrical flaws have the height to diameter ratio of 1 : 1, except the 50 μm one, which has a height of 250 μm.

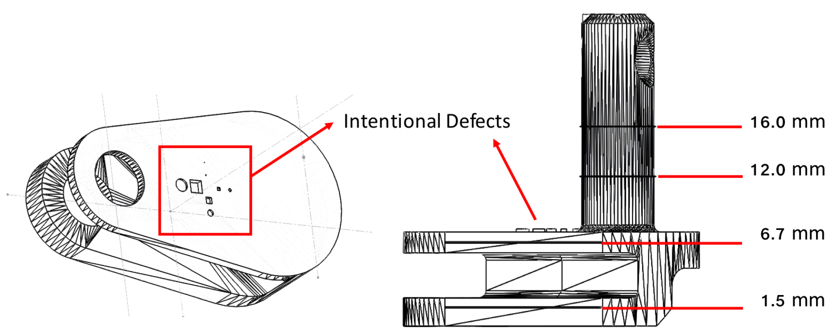

Figure 4.9. Locations of intentional flaws in CAD file of the drag link joint build.

Embedded flaws represent the lack of fusion problem in LPBF (i.e., small zones of infused material placed in a component), which is caused by multiple factors including the improper selection of laser power, layer thickness, hatch spacing, scanning speed [2]. In the case study, AM technicians in the Center for Innovative Material Processing Through Direct Digital Deposition (CIMP-3D) at

The Pennsylvania State University visually inspected each layer in XCT scans of the build to identify the flaws in the optical layerwise image. The XCT scans serve as the ground truth in this study, which helps confirm the presence of intentional flaws and other unwanted flaws. The layout of the build plate for this study is shown in Figure 4.10.

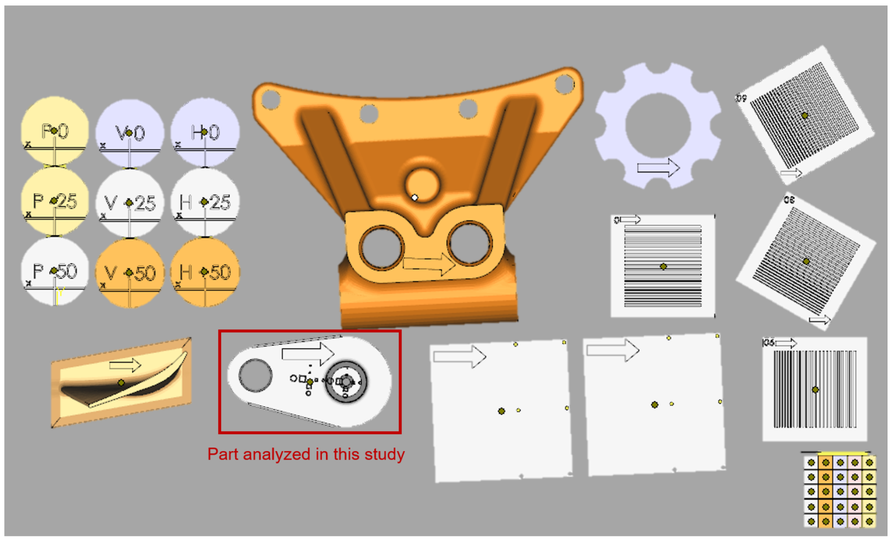

Figure 4.10. Build plate of the experiment in LPBF machine.

We utilize the following metrics to benchmark the performance of the proposed methodology with alternative methods: specificity (SPE), sensitivity (SEN), accuracy (ACC), negative predictive value (NPV) and positive predictive value (PPV).

$$
\begin{aligned}
SEN = \frac{TP}{TP+FN},\ SPE = \frac{TN}{FP+TN}, \\
ACC = \frac{TP+TN}{TP+TN+FP+FN}, \\
NPV = \frac{TN}{TN+FN},\ PPV = \frac{TP}{TP+FP}
\end{aligned}
\tag{4.25}
$$

where TP, FP, TN, FN and mean "true positive", "false positive", "true negative" and "false negative", respectively. Note that specificity measures the proportion of actual negatives (i.e., partitions without flaws that are correctly identified). Sensitivity calculates the proportion of actual positives, i.e., partitions with flaws are correctly identified as such. Accuracy is the ratio of partitions (i.e., either with

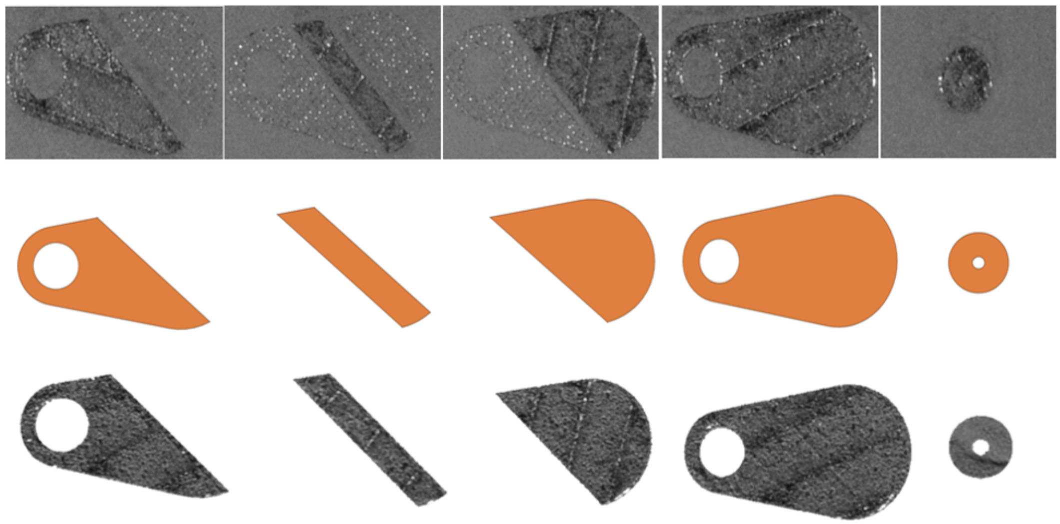

Figure 4.11. An example of cropped images (first row), CAD file (second row) and estimated ROIs (third row).

Figure 4.12. An example of hierarchical dyadic partitioning for five different layerwise images of the drag link joint part.

flaws or without flaws) that are correctly identified in the testing datasets. NPV measures the proportion of negatives in the diagnostic test that are true negatives, and PPV measures the proportion of positives in the diagnostic test that is true positives.

4.5 Experimental Results

4.5.1 Layerwise ROI Estimation and Freeform Geometry Analysis

Figure 5.7 shows an example of image registration in AM. Here, the first row shows five different layerwise images taken during the printing process. The second row presents the associated CAD file, and the last row illustrates the estimated ROIs for these five images. Note that we first perform histogram equalization to enhance edge contrast. Then, enhanced images and corresponding CAD file are utilized for the shape-to-image registration. Subsequently, we extract ROI by multiplying registered image with binarized CAD matrix. Finally, we partition the ROI into sROIs based on its relative size compared to the layer with the smallest ROI. Also, each generated sROI is bisected to provide multi-scale analysis for accurate flaw detection and to find the approximate location of flaws in AM.

Figure 4.12 illustrates an example of the hierarchical dyadic partitioning for five layerwise images with different ROIs from the drag link joint build. Here, the number of pixels for ROIs from left to right are 22916, 8946, 28723, 44257, and 4709, respectively. It is worth mentioning that extracted ROIs are further partitioned into smaller sROIs with the pixel number equal to the smallest ROI (i.e., the first shape is divided into five sROIs). Each of the sROIs is iteratively partitioned into two smaller sections for multi-scale analysis. As shown in the second row of Figure 4.12, we utilized the parallel straight lines for displaying our bisection results. A layer is defined defective when the results of first and second level localization show a flaw in at least one of the sROIs and its associated dyadic partitions.

Note that our proposed methodology guarantees that partitions of each ROI do not overlap with each other (i.e., before bisection, our algorithm trace back to find the result of the first-level partitions). This helps to perform spatial characterization in the next step independently. Also, dyadic partitioning allows to characterize and learn sROIs in different scales, which leads to an accurate estimation of defective layers and the corresponding flaw locations.

4.5.2 Spatial Characterization of sROIs

Semiparametric spatial characterization is developed to highlight the rich information hidden in multi-scale sROIs. Due to the partitioning, there are sROIs with different shapes in each layer, which pose great challenges on DNN learning. Spatial characterization circumvents the dependency on sROIs' shapes and boosts the computation speed in DNN. Note that this characterization transforms each sROI into a three-dimensional surface. Because the number of pixels in each sROI is the same as others, such characterization methods will result in images of the same size. As such, DNNs can be used to learn the images of the same dimensionality from spatial characterization, rather than the sROIs of different shapes. The contour representation of anisotropic semivariograms shows the level curves of the three-dimensional surface from spatial characterization. Figure 4.13 shows contour plot of two partitions for a characterized sROI (i.e., one with flaws and the other without flaw) which belongs to the image of the layer 51 in the drag link joint part.

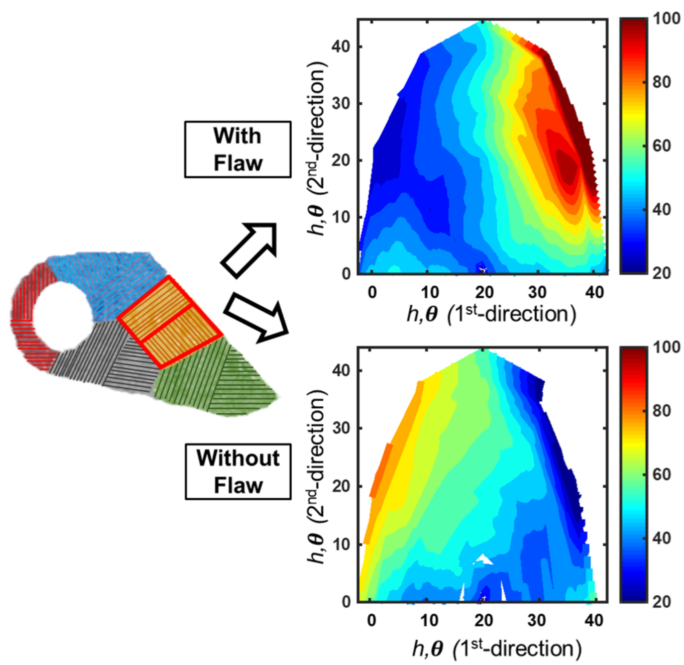

Figure 4.13. Spatial characterization of the sROI which includes partition with flaw and without flaw for layerwise image 51 in the drag link joint part.

As shown in Figure 4.13, the anisotropic semivariogram characterization and contour representation result in different patterns for the sROI. Note that dyadic partitioning splits the sROI into two regions with the same size. Here, the top partition has two flaws, while the bottom partition is flawless. The two flaws (i.e., the 750 μm cylinder and the 750 μm cube) are displayed as black holes in the image, and they lead to different anisotropic semivariogram. It is clearly shown that the location of peaks in the contour plot is in reverse directions. The contour plot at the top shows its peak at the right side with the latitude around 100, while the contour plot at the bottom has the peak on the left with the smaller latitude of 80. Furthermore, the contour has more disconnections (i.e., see the origin point) when the sROI has flaws. The anisotropic semivariogram and its contour representation also eliminate dependency on the sROI geometries and reduce the bias in DNN learning as the model would in favor of one shape that outnumbers the others. It is worth mentioning that the semivariogram characteristics in Figure 4.13 changes in different directions, which reveals the anisotropic behavior of layerwise AM images.

4.5.3 DNN Learning of sROIs in Layerwise Images for Detection of Incipient Flaws

We performed proposed DNN learning to identify layers with intentional flaws as well as their approximate locations. These sROIs are spatially characterized and used as inputs into the pre-trained DNN structure for incremental learning of incipient flaws. The result shows that DNN learning of layerwise variant geometry not only leads to the promising ACC of $92.50 \pm 1.03\%$ but also provides high SPE (i.e., $93.85 \pm 0.83\%$) and SEN (i.e., $90.01 \pm 1.56\%$), which are conducive to realize the effective flaw detection and layerwise quality control in the practice.

Table 4.2. Performance comparison of the proposed DNN (with the images of spatial characterization results as inputs), as well as KNN, logit, SVM, DT, LDA and BT methods (with the aggregated statistical features as inputs) for flaw detection in the real-world case study.

Model Input	Methodology	SPE(%)	SEN(%)	NPV(%)	PPV(%)	ACC(%)	Time(s)
sROI spatial characterization	DNN	93.85 ± 0.83	90.01 ± 1.56	93.83 ± 0.67	90.03 ± 2.34	92.50 ± 1.03	5.06 ± 0.01
ROI statistical features: mean, median, variance, skewness, kurtosis, minimum, maximum and range	KNN	45.55 ± 12.52	48.48 ± 8.78	35.44 ± 12.08	58.93 ± 13.02	47.36 ± 7.48	5.49 ± 0.18
	Logit	49.38 ± 8.72	53.18 ± 15.46	73.87 ± 12.94	27.33 ± 10.53	50.42 ± 8.54	5.07 ± 0.01
	SVM	68.06 ± 19.59	55.97 ± 7.92	30.42 ± 12.33	85.24 ± 10.70	58.17 ± 7.87	5.06 ± 0.01
	DT	57.23 ± 11.54	56.32 ± 8.80	45.37 ± 13.94	67.13 ± 11.90	56.27 ± 7.31	5.07 ± 0.01
	LDA	58.04 ± 9.54	69.41 ± 14.47	78.73 ± 11.59	44.94 ± 12.99	61.51 ± 8.58	5.62 ± 0.12
	BT	61.99 ± 10.91	61.80 ± 10.67	57.17 ± 13.68	65.79 ± 12.15	61.47 ± 8.23	5.92 ± 0.47

Pixel intensity is a single number ranging from 0 to 255 (i.e., 0 stands for black, and 255 is white), which illustrates brightness of the pixel in a grayscale image. Note that the distributions of sROIs with and without flaws are significantly different due to the presence of darker pixels in sROIs of with flaws (i.e., their values will be smaller and close to zero). We extract statistical features (i.e., mean, median, variance, skewness, kurtosis, minimum, maximum and range based on pixel intensities) from each grayscale ROIs, and further implement traditional machine learning methods (i.e., KNN, Logit, SVM, DT, LDA and BT) as benchmarks to our proposed methodology. The results are computed based on 4 fold cross-validation for 100 replications. Here, a layer is defined defective when the results of first and second level localization show a flaw in at least one of the sROIs and its associated dyadic partitions. As shown in Table 4.2, the proposed DNN leads to the high-performance measurements (i.e., SPE, SEN, NPV, PPV, and ACC) in comparison with traditional machine learning methods. In addition, the last column of Table 4.2 shows the computation time of testing dataset for the proposed DNN as well as traditional machine learning methods in this multi-scale analysis. Note that the computational cost of the proposed DNN and alternative methods is similar.

As shown in Table 4.2, it is imperative to integrate new AI methods with engineering domain knowledge. Our experimental results show that:

1. **Learn the right thing:** It is not desirable to use the AI to learn the cropped square region in an image that contains both ROIs and the unfused powder outside the ROIs. Therefore, we need to leverage engineering knowledge to perform ROI estimation before the flaw detection in AM.

2. **Image pattern vs. aggregated information:** Semivariograms consist of the rich information and patterns in layerwise optical images. If we only aggregate the information (i.e., descriptive statistics), the performance of flaw detection will not be good.

3. **DNN learning of semivariograms vs. other analytical methods with aggregated statistics:** DNNs learn complex patterns directly from layerwise images. On the other hand, traditional analytical methods utilize aggregated features and statistics.

Figure 4.14 shows the error rate for the proposed DNN and alternative methods.

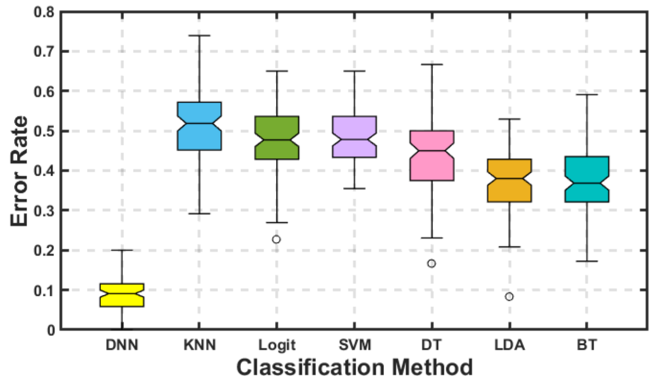

Figure 4.14. Performance comparison between the proposed DNN and off-the-shelf classification models (i.e., KNN, Logit, SVM, DT, LDA and BT) for flaw detection in the real-world case study.

As shown in Figure 4.14, the average error rate and standard deviation of the proposed methodology (i.e., DNN) are significantly smaller than traditional machine learning methods (i.e., KNN, logit, etc.) in flaw detection. Note that traditional machine learning methods utilize aggregated indicators (i.e., descriptive statistics) for image-guided flaw detection, which only provides the summary information and tends to be limited to fully exploit rich information in layerwise optical images. Also, optimal design and extraction of these features are indispensable to achieving an effective predictive model, which is however, highly dependent on engineering domain knowledge. On the other hand, the proposed methodology with unique capabilities to handle variant geometry (i.e., ROI estimation, freeform geometry analysis, spatial characterization and DNN learning of incipient flaws) leads to the accurate estimation of flaws and achieves significantly lower error rate compared to alternative methods.

This investigation provides useful insights and guidelines regarding the DNN learning of variant geometry in layerwise image profiles for AM quality management.

1. **Training data:** To prepare AM training data and build an effective predictive model, it is necessary to integrate new AI methods with engineering domain knowledge to tackle the challenges of broad geometrical diversity in layerwise AM images. To tackle this problem, We propose the following steps: 1) layerwise ROI estimation, 2) freeform geometry analysis by hierarchical dyadic partitioning, 3) spatial characterization, and 4) DNN learning of incipient flaws.

2. **Minimum number of training images:** For the purpose of manufacturing informatics, the more data the better. However, the size of data is often limited by the number of builds. In our case study, there are a total of 362 layers, which are registered to 362 ROIs. During the investigation, we had concerns on variant geometries form one layer to the next layer, as well as the size of data for training. We found that it is not a good practice to just "feed images of layers" to a neural network. The idea of freeform geometry analysis not only tackles the problem of geometrical diversity in layerwise images but also generates 1,708 sROIs that provides a larger set of data for DNN training.

3. **Open-box approaches:** It is suggested that the minimum number of training images depends on the prior knowledge in DNN models, as well as the learning tasks. If the learning task is new and the DNN model is not pre-trained for image learning, a large number of images in the magnitude of thousands or more is necessary. Otherwise, thousands of images will suffice in general. However, the success of AI for manufacturing informatics is highly dependent on engineering domain knowledge, which is known as "open-box" approaches. The practice of "black-box" learning (i.e., feed images of layers to neural networks and then let AI figure it out) is not suggested for quality management in AM.

4.6 Conclusions

Although recent AM machines are greatly ameliorated from early forms, significant challenges in quality control due to the mass customization and low-volume production are still key holding forces that prevent AM from further proliferation in the manufacturing industry. In-situ layerwise image sensing systems are recently developed to help address this key challenge in AM. However, they are still at an early age and are limited in the ability to account for different layerwise geometries to perform on-the-fly quality control. There is an urgent need to couple in-situ image data with newly developed machine learning methods, and realize the qualify-as-you-build paradigm in AM. However, due to the significant variations in layerwise geometries in the build of customized products, image-guided learning methods such as DNNs are limited in the ability to learn incipient flaws directly from layerwise images. In this paper, we develop a novel methodology that leverages the CAD file to register the ROI in each layerwise image. Next, we propose a dyadic partitioning method to delineate variant ROI into distinctive regions with the same size and in multiple scales. Then, we develop the semiparametric spatial model to characterize the complex spatial patterns in subregion ROIs. Finally, a DNN is designed to learn incipient flaws from spatial characterization images. Experimental results show that our proposed deep learning methodology detects flaws in real-time with specificity $93.85 \pm 0.83\%$, sensitivity $90.01 \pm 1.56\%$, negative predictive value $93.83 \pm 0.67\%$, positive predictive value $90.03 \pm 2.34\%$ and accuracy of $92.50 \pm 1.03\%$. This provides a significant opportunity to counteract and repair incipient defects in AM prior to completion of the build, and thereby mitigate scrap and rework rates and further ensure the economic viability of AM. The proposed methodology can also be generally applicable in a variety of engineering and medical domains that entail customized designs and image-guided process control.

Chapter 5 Spatiotemporal Gaussian Process Modeling and Monitoring

Spatiotemporal Gaussian Process Monitoring of Layerwise Builds in Additive Manufacturing

Abstract

Advanced imaging is increasingly invested in additive manufacturing to improve the information visibility and cope with the process complexity. This leads to the plethora of in-situ images with complex spatiotemporal correlations (i.e., spatial represents regional dependency within a layer and temporal stands for perpetuation of flaws on subsequent layers at the same location) and layer-to-layer geometry variations. However, current AM monitoring of variant geometry focuses more on key characteristics of layerwise imaging profiles and is rather limited in the ability to handle spatial and temporal effects. On the other hand, most of existing works on image monitoring are tailored for regular data structure (i.e., the same dimensionality for each image), instead of variant geometry with dimensionality variations from one layer to another. This paper presents a novel spatiotemporal Gaussian process (STGP) for image-guided monitoring of AM processes. Specifically, we introduce the first GP module to model the standard geometric profile within region of interests, and the second GP module to capture spatiotemporal deviations in the AM processes. The STGP is designed with the online

update and sparse structure to deal with the multi-layer production process and tackle the high-dimensionality of layerwise AM images. Finally, we leverage the STGP model to develop new monitoring charts, namely, the spatiotemporal T-squared (STT^2) and spatiotemporal likelihood ratio (STLR) tests, for the anomaly detection in AM processes. The developed methodology is evaluated and validated with both simulation and real-world case studies. Experimental results demonstrate the effectiveness of the STGP model for layerwise AM quality control.

5.1 Introduction

With rapid advances of sensing technology, AM is shifting from post-build quality inspection to in-process and high-resolution imaging measurement. As such, high-dimensional images become readily available and bring a data-rich environment in AM [121]. This provides an unprecedented opportunity to improve AM process control and cope with the design complexity.

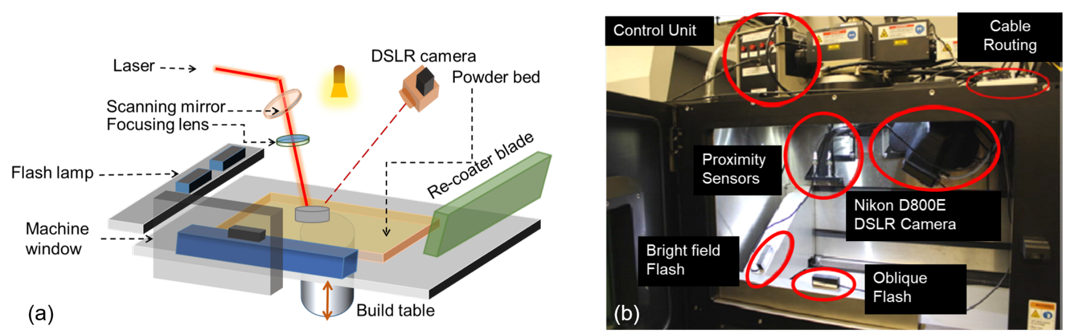

Figure 5.1. (a) The schematic view of optical system integrated with the LPBF machine, and (b) The advanced imaging system.

Figure 5.1 (a) and (b) show an LPBF process that fabricates metal builds with complex geometries directly from digital designs. The LPBF process broadens range of designs that can be considered for fabrication [149]. An optical camera is integrated with the LPBF machine to measure layerwise finishes of an AM build.

Because metal powders are deposited and sintered or melted in the layer-by-layer fashion, there exist complex spatial (i.e., within a layer) and temporal (i.e., across layers) correlations in layerwise images. In other words, heat transfer in the melt pool during fabrication process causes the region to experience similar conditions, which in turn, leads to the spatial correlations among pixels of a layerwise image. Also, the melt pool evolves as layers are accumulated and results in dependency between layerwise images, which is called the temporal effect. As shown in Figure 5.2, during processing, melting and solidification are influenced by and impact adjacent regions with the same layer, as well as adjacent layers. Such spatiotemporal correlations are critical to gaining an in-depth understanding of defect formation and propagation. In addition, AM fabrication of customized build involves a high degree of geometry changes across layers. Although layerwise images can be cropped into a squared region for all layers, some layers may have small ROIs and large powder areas, while others have large ROIs and small powder areas. As a result, cropped squared regions are highly biased due to inconsistent ROIs from one layer to another.

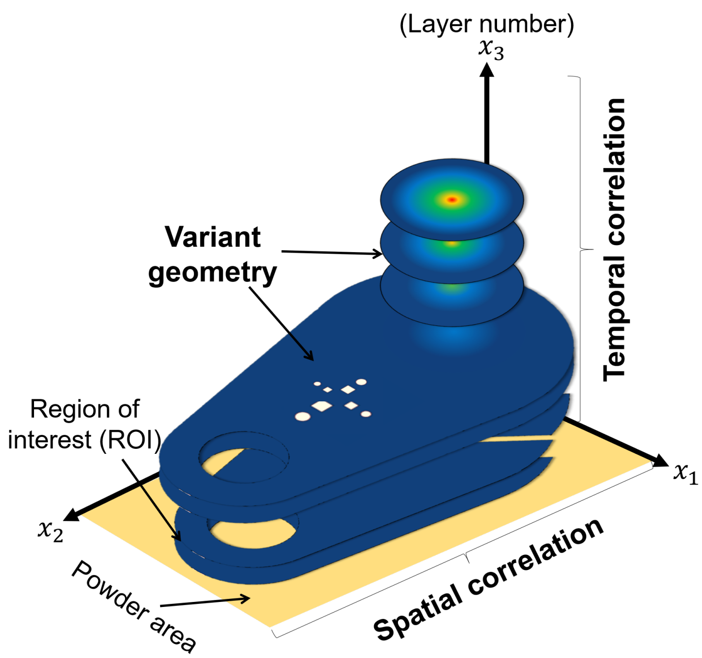

Figure 5.2. An illustration of spatiotemporal correlation and variant geometry in AM layerwise images.

Most of existing works focus more on key characteristics of layerwise imaging profiles for defect characterization and detection [7,150], but are less concerned about spatiotemporal process modeling. As such, traditional methods tend to be limited in the ability to model the formation and propagation of the underlying defects in AM processes. Furthermore, conventional image-based monitoring methods are not designed to work with dimensionality variations from one layer to another. For instance, principal component analysis (PCA) and singular value decomposition (SVD) have been used for monitoring images with the same size in rolling process [151]. Also, multivariate monitoring was utilized to detect anomaly in the forging process from the stream image data with the same dimensionality [152]. However, very little has been done to consider both spatiotemporal correlations and layer-to-layer geometry variations for AM process monitoring and control.

This paper presents a novel spatiotemporal Gaussian process (STGP) to model correlations within ROIs of layerwise images for statistical quality control of AM processes. The STGP model consists of two GP modules, where the first one approximates the standard spatial profile and the second one models spatiotemporal deviations in the AM process. Also, a sparse algorithm is designed to boost the computational efficiency in STGP modeling of large amounts of layerwise images. An online update of STGP is developed to cope with the bottom-up fabrication procedure in AM. In other words, we sequentially update the set of layerwise images and covariance matrices to estimate distribution of pixel intensities in upcoming layers. Based on the model predictions, we further design the spatiotemporal T-squared (STT^2) and spatiotemporal likelihood ratio (STLR) control charts to detect the anomaly of a new layer and analyze the root causes. It is worth mentioning that the STT^2 test does not require prior knowledge on possible shift patterns, while the STLR test is conducive to detect different types of anomaly patterns (e.g., a shift in standard geometric profile or a change in geometric correlation) within the ROI of layerwise images. For example, a change in the laser power in LPBF results in a build with a high level of porosity, which can be represented as a shift in geometric variance in layerwise images. As a result, by finding shift patterns we are capable of performing root-cause analysis.

The proposed methodology is evaluated and validated with both simulation experiments and a real-world case study on the drag link joint build fabricated by an LPBF machine. Experimental results show the effectiveness of the proposed STGP method on real-time monitoring of LPBF process using layerwise images. Image-guided AM is critical to reducing the scrap rate and move forward to the industrial-scale production. The remainder of this paper is organized as follows: Section 2 provides a literature review on the relevant methods of image-based process monitoring. Section 3 presents the proposed STGP methodology. Experimental design and materials are given in Section 4. Section 5 shows experimental results for the simulation study as well as the real-world case study. In the end, we conclude this paper by highlighting gaps of existing quality monitoring methods for spatiotemporal modeling of layerwise images, then provide an overview of the proposed methodology.

5.2 Research Background

The wide application of AM imaging technology brings the proliferation of image data in the layerwise fabrication processes. This, in turn, fuels increasing interest to develop new image-guided methods and tools for process monitoring and quality control.

5.2.1 Image-guided AM Monitoring of Variant Geometry

Image-guided AM becomes a prevalent way of monitoring variant geometry with dimensionality variations from one layer to another. High-resolution cameras with visible wavelength play an important role in monitoring and detection of flaws in AM layers so as to detect process errors and material discontinuities. Imani et al. [34] and Yao et al. [93] developed a multifractal methodology to investigate the irregular and nonlinear patterns of AM layerwise images for the characterization and detection of defects. Image thresholding was also implemented to determine ROIs and then coordinate transformation was adopted to extract features for real-time monitoring of defect [1, 13]. Foster et al. [15] investigated images taken under oblique illuminations of fused and pre-placed powder layers to find porosity, poor surface finish, and thermal deformation. Grasso et al. [27] studied a PCA-based statistical model to identify defective areas of a layer using a high-speed camera (i.e., an Olympus I-speed 3 camera) placed outside the build chamber. AM layerwise images have also been utilized to investigate the impact of process and design parameters on the formation of various defects in AM builds. For example, Gaikwad et al. [153, 154] and Chen et al. [149] introduced process monitoring of layerwise images to quantify the impact of design parameters (i.e., geometry and orientation) on the quality of thin-wall builds. Imani et al. [2] quantified the impact of process parameters (i.e., hatch spacing, laser velocity, and laser power) on the quality of AM build. Spectral graph theory was studied to analyze in-process layerwise images and identify process conditions that are liable to cause porosity. Also, a deep neural network approach was developed to learn the variant geometry in each layer of the AM build for incipient flaw detection [155, 156]. Yao et al. [35] designed Markov decision process and utilized the layerwise imaging data to find an optimal control policy. The proposed method has the potential to determine optimal corrective actions to counteract and repair incipient defects in AM prior to completion of the build. However, most of previous methods focus more on defect formation and surface characterization and are less concerned about spatiotemporal AM correlations for process monitoring.

5.2.2 Image-based Process Monitoring

Image-based process monitoring can be categorized into two main groups. The first group includes dimension-reduction methods that utilize the function decomposition to map images into a lower dimension space. Lin et al. [157] investigated the wavelet-based PCA approach to detect surface flaws in light-emitting diode chips through images. Yan et al. [158] developed a tensor-based monitoring approach that models spatial and time-varying images using the PCA. Lu and Tsai [159] introduced automatic visual inspection of micro defects on thin-film transistor liquid crystal displays. They designed SVD as a global image reconstruction scheme to decompose images of a liquid crystal display panel into a low-rank background texture and sparse spatial flaws. Wood et al. [160] developed a three-dimensional multivariate Fourier transformation to study the shape and penetration of important anatomical and histopathological features based on the underlying macromolecular chemistry. Mei [161] introduced local CUSUM statistic for monitoring individual images with spatiotemporal correlation. Megahed et al. [162] introduced a spatiotemporal GLR control charting scheme for monitoring grayscale images of industrial parts, which are characterized by uniformity within the image or by a specific desired pattern. Note that most of dimension-reduction methods used linear transformation to represent and decompose image profiles into low-dimensional extracted features, and tend to be limited in the ability to handle nonlinear patterns and correlations. Most importantly, these methods are designed to work with regular images structures (i.e., rectangular images that have a fixed size over time) and are not designed to monitor the quality in AM images that manifest layer-to-layer geometry variations.

The second group is spatial profile monitoring where nonparametric functions are used to model spatial profiles in images including splines monitoring, kernel smoother, radial basis functions, mixed-effect model, ANOVA, and GP methods [163–166]. GP has received notable attention as a popular nonparametric method for modeling and monitoring image profiles with complex patterns [167]. Also, compared to other nonparametric methods such as B-splines or kernel smoother, GP provides more flexibility to be extended to higher dimensions [168, 169]. Liu et al. [170] implemented an augmented layerwise spatial log Gaussian Cox process (ALS-LGCP) model to quantify the distribution of pores within each layer of the AM part and tracks their evolution across layers based on post-build images. Zhang et al. [171] designed an additive GP model to monitor the wafer quality with the assumption that spatial profiles are only correlated within a wafer, but are independent among different wafers. However, both additive GP and ALS-LGCP models are not designed for monitoring the AM process with a high degree of layer-to-layer correlation and geometry variation.

There is an urgent need to develop new analytical methods and tools that consider both layer-to-layer geometry variation a spatiotemporal correlation for process monitoring and control in AM.

5.3 Research Methodology

The proposed methodology consists of three main steps: 1) layerwise ROI estimation, 2) spatiotemporal Gaussian process modeling, and 3) statistical monitoring of layerwise ROIs. As shown in Figure 5.3, the ROI of a newly produced layer (i.e., $\boldsymbol{X}_{L+1}$) enters the STGP model. Then, the proposed methodology estimates distribution of pixel intensities for this new ROI by considering both within-a-layer and across-layer correlations. Then, STT^2 chart test the conformity of the ROI based on the spatiotemporal correlations of AM and detect the anomaly in the layerwise image. Note that for STT^2 statistic, we do not need to have prior knowledge on types of possible shifts due to the fact that there is no specification of pixel distribution in the ROI of a newly fabricated layer. On the other hand, the STLR test is designed to identify particular types of root causes. If the ROI is within control limits of both charts, then it will be integrated with the in-control set to evaluate upcoming layers. Otherwise, the null hypothesis will be rejected and it will be marked as an anomaly.

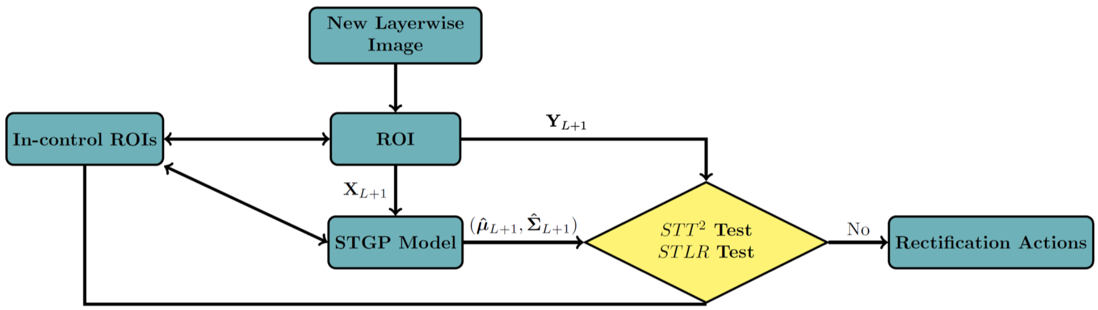

Figure 5.3. The flow diagram of STGP methodology for real-time monitoring of ROIs in layerwise images.

5.3.1 Layerwise ROI Estimation

The image registration finds the point-to-point correspondence between a sliced CAD file and an optical image of an AM layer. Note that this paper focuses on the STGP modeling and does not preclude others to use a different ROI estimation approach. We used a standard registration process that includes four components, namely similarity metric, optimizer, moving transformation, and interpolator. The similarity metric evaluates the accuracy of image registration by returning a scalar value that demonstrates the similarity between these two images based on the average square differences in pixel intensities. The optimizer defines the search strategy, and the interpolator takes the pixel intensities to the new coordinate system based on the moving transformation and then measures the difference among intensity values. This iterative process is continued to obtain the moving transformation that optimizes the similarity metric. Then, we isolate the ROI from the background in the registered image via multiplication of optimally transformed image and binarized CAD file. This investigation focuses on the ROIs with variant layerwise geometry, instead of the powder areas outside the ROIs. The detail of the ROI estimation method is provided in Section 4.3.1.

Table 5.1. Summary of Notations

Notation	Definition
$\boldsymbol{X}_{[1:L]}$	Pixel coordinates of in-control set
$\boldsymbol{X}_{L+1}$	Pixel coordinates in ROI of newly fabricated layer
$\boldsymbol{X}_U$	Pixel coordinates of inducing points
$\boldsymbol{X}_l$	Pixel coordinates of ROI in layer l
$\boldsymbol{x}_j$	Coordinates of pixel j
$x_i^{(j)}$	The i^{th} element of coordinate of pixel j
$\boldsymbol{X}_{u_i}$	Coordinates of inducing points in layer i
$\boldsymbol{Y}_{[1:L]}$	Pixel intensities of in-control set
$\boldsymbol{Y}_{L+1}$	Pixel intensities in ROI of newly fabricated layer
$\boldsymbol{Y}_U$	Pixel intensities of inducing points
$\boldsymbol{Y}_l$	Pixel intensities in layer l
y_j	Intensity of pixel j
$\boldsymbol{Y}_{u_i}$	Pixel intensities of inducing points in layer i
$J_{[1:L]}$	Number of pixels in ROI of in-control set l
J_l	Number of pixels in ROI of layer l
J_{L+1}	Number of pixels in ROI of newly fabricated layer
J_U	Number of pixels in ROI of inducing points set
$f(.)$	Mapping function for modeling standard surface profile
$\epsilon(.)$	Deviation function from the standard surface profile
$\eta(.)$	Assignable causes function
m_f	Mean function of GP for the standard surface profile
m_η	Mean function of GP for the root-causes model
$\hat{\boldsymbol{\mu}}_{L+1}$	Posterior mean function of new fabricated layer
$\hat{\boldsymbol{\mu}}_U$	Posterior mean function of inducing points
$\hat{\boldsymbol{\mu}}_U^+$	updated posterior mean function of inducing points
$\boldsymbol{K}$	Prior covariance matrix
$\boldsymbol{Q}$	Low-rank covariance matrix representing information flow using inducing points
$\boldsymbol{\Lambda}$	Block diagonal covariance matrix used for estimation of $\boldsymbol{K}$
$\tilde{\boldsymbol{\Lambda}}$	Block diagonal covariance matrix with the ridge term
k_f	Covariance function of GP for the standard surface profile
k_ϵ	Spatiotemporal covariance of deviation function
k_{ϵ_s}	Within-a-layer covariance of deviation function
k_{ϵ_l}	Across-layers covariance of deviation function
k_η	Covariance function of the root cause model
$\hat{\boldsymbol{\Sigma}}_{L+1}$	Posterior covariance function of newly fabricated layer
$\hat{\boldsymbol{\Sigma}}_U$	Posterior covariance function of inducing points
$\hat{\boldsymbol{\Sigma}}_U^+$	Updated variance of inducing points
σ_ϵ^2	Signal variance hyperparamters for the covariance function of deviation GP
σ_f^2	Signal variance hyperparamters for the covariance function of standard GP
σ_η^2	Signal variance hyperparamters for the covariance function of root-cause GP
σ_{noise}^2	Ridge term representing Gaussian noise in in-control set
$\boldsymbol{\theta}_1$	Correlation hyperparameters for the covariance function of standard GP
$\boldsymbol{\theta}_2$	Hyperparameters for the covariance function of deviation GP
$\boldsymbol{\theta}_3$	Hyperparameters for the covariance function of root-cause GP
Γ	Set of hyperparameters in STGP model
l	In-control layer number $\forall\, l = 1, ..., L$
$L+1$	Newly fabricated layer
j	Index of Pixel coordinates $\forall\, j = 1, ..., J_l$

5.3.2 Statistical Modeling with STGP

5.3.2.1 Problem formulation

The stream of image profiles is modeled as the addition of two independent functions. The first function models the standard spatial profile, while the second function represents the within-a-layer and across-layers deviations.

$$y_j = f(\boldsymbol{x}_j) + \epsilon(\boldsymbol{x}_j) \qquad \begin{array}{r} \forall\ j = 1, ..., J_l \\ l = 1, ..., L \end{array} \tag{5.1}$$

where $f(.)$ is a mapping function that models the standard surface profile (i.e., desired or designed pixel intensities in ROIs from the AM process). More specifically, standard surface profile is defined as the pixel intensities of ROIs in a build when there is no correlation between layers. However, exact function is often unknown and needs to be estimated from data. Also, ϵ is the second function that represents the deviation from the standard profile. Note that $\epsilon(.)$ denotes the deviation function in this model and is different from Gaussian noise. Similar AM process conditions for a layer and across layers lead to the decomposition of deviation model ϵ into two main parts: the first part estimates the spatial correlation among pixels within a same layer and the second one simultaneously approximates spatial and temporal correlations for the pixels that are located in different layers. Suppose L layers have been fabricated and their ROIs have been estimated when the process is in control. We denote $\boldsymbol{x}_j = [x_1^{(j)}, x_2^{(j)}, x_3^{(j)}]^T$ as a three-dimensional coordinates of pixel j. The $x_i^{(j)}$ $\forall i = 1, ..., 3$, represents the pixel's coordinate in the i^{th} dimension (e.g., $x_3^{(j)}$ is the z-axis that is layer number). The set of pixels in ROI of layer l and their intensities can be expressed as $\boldsymbol{X}_l = [\boldsymbol{x}_1, ..., \boldsymbol{x}_{J_l}]$ and $\boldsymbol{Y}_l = [y_1, ..., y_{J_l}]$, respectively. Furthermore, $\boldsymbol{X}_{[1:L]} = [\boldsymbol{X}_1, ..., \boldsymbol{X}_L]^T$ is the coordinates of pixels for in-control set with the size $J_{[1:L]} \times 3$ where $J_{[1:L]} = \sum_{j,l} |\boldsymbol{x}_{j_l}|$. It is worth mentioning that the customized geometry of an AM build causes unbalanced number of pixels in ROIs of layerwise AM images. Therefore, $J_1, ..., J_L$ denote the varying number of pixels in ROI of layer $1, ..., L$, respectively. Also, $\boldsymbol{Y}_{[1:L]} = [\boldsymbol{Y}_1, ..., \boldsymbol{Y}_L]^T$ shows pixels intensity of layerwise ROIs with variant geometry in the set of in-control layers, which has the size $J_{[1:L]} \times 1$.

5.3.2.2 STGP

To account for spatiotemporal correlations in high-dimensional layerwise AM images, we design the STGP to model standard pixel intensities and quantify variation in ROIs of AM images with layer-to-layer geometry variation in real-time. In Eq. (5.1), f as a standard pixel distribution in the AM process is usually unknown. We assume that f is a realization of a GP.

$$f \sim \mathcal{GP}(m_f, k_f) \tag{5.2}$$

where m_f is the mean function and k_f is the squared exponential covariance function:

$$k_f(\boldsymbol{x}_j, \boldsymbol{x}_{j'}) = \sigma_f^2 \exp\Big[-(\boldsymbol{x}_{j[1:2]} - \boldsymbol{x}_{j'[1:2]})^T \times \mathrm{diag}(\boldsymbol{\theta}_1) \times (\boldsymbol{x}_{j[1:2]} - \boldsymbol{x}_{j'[1:2]})\Big] \tag{5.3}$$

In Eq. (5.3), σ_f^2 and $\boldsymbol{\theta}_1$ are the signal variance and correlation hyperparameters, and $\mathrm{diag}(\boldsymbol{\theta}_1)$ is the diagonal matrix with vector $\boldsymbol{\theta}_1$ in the squared exponential covariance function. Also, $\boldsymbol{x}_{j[1:2]}$ denotes the pixel coordinates in the first and second dimensional directions (i.e., within a layer). Furthermore, we utilize another realization of an independent GP with zero mean and following covariacne to capture the within a layer and across layers deviations for layerwise ROIs of AM process.

$$\epsilon \sim \mathcal{GP}(0, k_\epsilon) \tag{5.4}$$

$$k_\epsilon = k_{\epsilon_s} + k_{\epsilon_l} \tag{5.5}$$

where k_ϵ is the covariance of deviation function ϵ, which is decomposed to within a layer covariance k_{ϵ_s} and across layers covariance k_{ϵ_l}. The k_ϵ takes the form:

$$k_\epsilon(\boldsymbol{x}_j, \boldsymbol{x}_{j'}) = \sigma_\epsilon^2 \exp\Big[-(\boldsymbol{x}_j - \boldsymbol{x}_{j'})^T \times \mathrm{diag}(\boldsymbol{\theta}_2) \times (\boldsymbol{x}_j - \boldsymbol{x}_{j'})\Big] \tag{5.6}$$

where $k_\epsilon(\boldsymbol{x}_j, \boldsymbol{x}_{j'})$ estimate the covariance between pixels $\boldsymbol{x}_j$ and $\boldsymbol{x}_{j'}$, σ_ϵ^2 and $\boldsymbol{\theta}_2$ are the signal variance and spatial correlation hyperparameters of k_ϵ. Note that if these two pixels are located on ROIs of different layers (i.e., $x_3^{(j)} \neq x_3^{(j')}$), then within a layer and across layers dependencies are captured by Eq. (5.6). On the other hand, for two pixels that are positioned in a same ROI (i.e., $x_3^{(j)} = x_3^{(j')}$), only within a layer dependency are estimated through the covariance function. Figure 5.4

illustrates the covariance structure of the standard and deviation functions. Each image profile is modeled as the addition of two realizations of GP, which is the proposed STGP model. As a result, the covariance matrix has the following structure:

$$\mathrm{cov}(y_j, y_{j'}) = \begin{cases} k_f + k_{\epsilon_s} & \forall\ x_3^{(j)} = x_3^{(j')} \\ k_f + k_{\epsilon_s} + k_{\epsilon_l} & \forall\ x_3^{(j)} \neq x_3^{(j')} \end{cases} \tag{5.7}$$

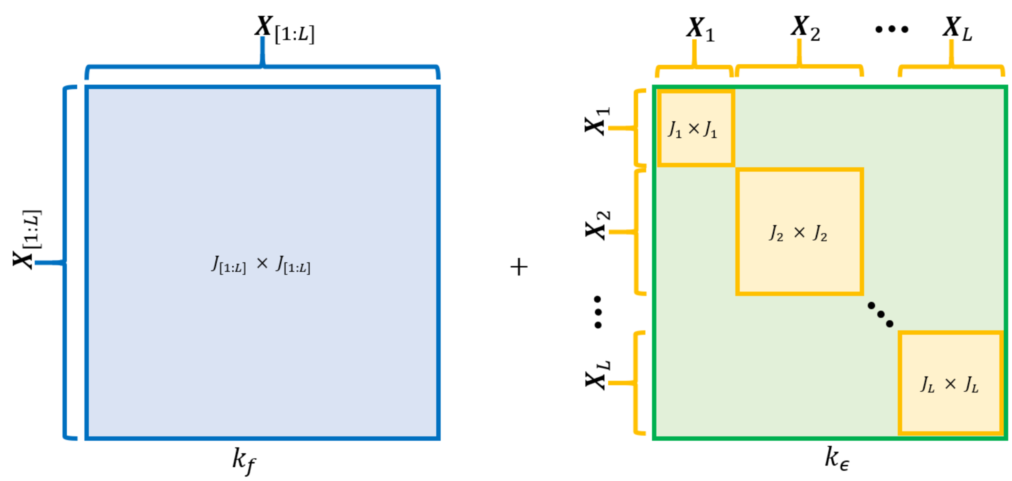

Figure 5.4. The covariance structure of STGP model. The blue, green and yellow areas are the non-zero matrix blocks with corresponding dimensions.

Note that the occurrence of flaws is not independent; rather, there is a spatial correlation in the distribution of flaws within each layer as well as directional correlation in the distribution of flaws across layers. Therefore, most of previous methods relying on the i.i.d. assumption for errors are not suitable for layerwise quality monitoring in AM.

Using the data from in-control ROIs over different layers, we can approximate the desired surface f and quantify variations which provide a baseline to monitor newly fabricated layer. In addition, we denote the $\boldsymbol{\Gamma} = [m_f, \sigma_f^2, \boldsymbol{\theta}_1, \sigma_\epsilon^2, \boldsymbol{\theta}_2]$ as a hyperparameter set in STGP model. Based on the property of GP and by knowing the $\boldsymbol{\Gamma}$, $\boldsymbol{Y}_{[1:L]}$ follows a multivariate Gaussian distribution with the following joint density function:

$$f(\mathbf{Y}_{[1:L]}|\boldsymbol{\Gamma}) = (2\pi)^{\frac{-J_{[1:L]}}{2}} (\det \boldsymbol{K}_{[1:L][1:L]}) \times \exp[-\frac{(\mathbf{Y}_{[1:L]} - m\mathbf{1}_{J_{[1:L]}})^T \boldsymbol{K}^{-1}_{[1:L][1:L]} (\mathbf{Y}_{[1:L]} - m\mathbf{1}_{J_{[1:L]}})}{2}] \tag{5.8}$$

where $\boldsymbol{K}_{[1:L][1:L]}$ is the prior covariance matrix for pixels in ROIs of in-control set, and its elements are calculated based on the structure illustrated in Figure 5.4. For the ROI of newly fabricated layer (i.e., $L+1$), we have pixel coordinates $\boldsymbol{X}_{L+1} = [\boldsymbol{x}_1, ..., \boldsymbol{x}_{J_{L+1}}]$ with intensity values $\boldsymbol{Y}_{L+1} = [y_1, ..., y_{J_{L+1}}]$. However, finding the inverse of the matrix with the size $J_{[1:L]} \times J_{[1:L]}$ has the computational cost of $O({J_{[1:L]}}^3)$ [172, 173]. Due to a number of layers with a large amount of pixels, we introduce the sparse algorithm for online update and computation of STGP model. We consider the common inducing assumption for sparse GP, which leverages the partial information of pixels in ROIs of in-control set. Inducing points is a small subset of the in-control set that is aimed at construction an approximation allowing the reduction of the time complexity. This approach derive such approximations by modifying the GP prior and then computing the marginal likelihood of the modified model. Let $\boldsymbol{X}_U = [\boldsymbol{X}_{u_1}, ..., \boldsymbol{X}_{u_L}]^T$ with the size $J_U \times 3$ be the set of all inducing pixels with intensities of $\boldsymbol{Y}_U = [\boldsymbol{Y}_{u_1}, ..., \boldsymbol{Y}_{u_L}]^T$. We denote $\boldsymbol{X}_{u_l}\ \forall\ l = 1, ..., L$ and $\boldsymbol{Y}_{u_l}\ \forall\ l = 1, ..., L$ as sets of pixel locations and intensities in layer l that include in corresponding inducing sets, respectively. We assume that $\boldsymbol{Y}_{[1:L]}$ and $\boldsymbol{Y}_{L+1}$ are conditionally independent given $\boldsymbol{Y}_U$.

$$p(\boldsymbol{Y}_{[1:L]}, \boldsymbol{Y}_{L+1} | \boldsymbol{Y}_U) = p(\boldsymbol{Y}_{[1:L]} | \boldsymbol{Y}_U) \times p(\boldsymbol{Y}_{L+1} | \boldsymbol{Y}_U) \tag{5.9}$$

Inducing assumption adjusts prior distribution as follows:

$$p(\boldsymbol{Y}_{[1:L]}, \boldsymbol{Y}_{L+1}, \boldsymbol{Y}_U) = p(\boldsymbol{Y}_{[1:L]} | \boldsymbol{Y}_U) \times p(\boldsymbol{Y}_{L+1} | \boldsymbol{Y}_U) \times p(\boldsymbol{Y}_U) \tag{5.10}$$

$$p(\boldsymbol{Y}_{[1:L]}, \boldsymbol{Y}_{L+1}, \boldsymbol{Y}_U) \sim \mathcal{N}\Bigg(\begin{bmatrix} m\mathbf{1}_{J_1} \\ \vdots \\ m\mathbf{1}_{J_L} \\ m\mathbf{1}_{J_{L+1}} \\ m\mathbf{1}_{J_U} \end{bmatrix}, \begin{bmatrix} \boldsymbol{K}_{1\,1} & \cdots & \boldsymbol{Q}_{1\,L} & \boldsymbol{Q}_{1\,L+1} & \boldsymbol{K}_{1\,U} \\ \vdots & \ddots & \vdots & \vdots & \vdots \\ \boldsymbol{Q}_{L\,1} & \cdots & \boldsymbol{K}_{L\,L} & \boldsymbol{Q}_{L\,L+1} & \boldsymbol{K}_{L\,U} \\ \boldsymbol{Q}_{L+1\,1} & \cdots & \boldsymbol{Q}_{L+1\,L} & \boldsymbol{K}_{L+1\,L+1} & \boldsymbol{K}_{L+1\,U} \\ \boldsymbol{K}_{U\,1} & \cdots & \boldsymbol{K}_{U\,L} & \boldsymbol{K}_{U\,L+1} & \boldsymbol{K}_{U\,U} \end{bmatrix} \Bigg) \tag{5.11}$$

where $\boldsymbol{Q}_{l\,l'} = \boldsymbol{K}_{l\,U} \boldsymbol{K}_{U\,U} \boldsymbol{K}_{U\,l'}$ and it shows that pixels in layers $[1:L]$ and $L+1$ communicate via U. The covariance for each element in Eq. (5.11) is calculated based on the structure represented in Eq. (5.7). For example, $\boldsymbol{K}_{L+1\,L+1}$ is the $J_{L+1} \times J_{L+1}$ covariance matrix between pixels of a newly fabricated layer where elements of the matrix are calculated through $k_f + k_{\epsilon_s}$. We replace $\boldsymbol{K}_{[1:L][1:L]}$ with $\boldsymbol{Q}$ and $\boldsymbol{\Lambda}$ as follows:

$$\boldsymbol{K}_{[1:L]\,[1:L]} = \boldsymbol{Q}_{[1:L]\,[1:L]} + \boldsymbol{\Lambda}_{[1:L]\,[1:L]} \tag{5.12}$$

where $\boldsymbol{\Lambda}_{[1:L]\,[1:L]} = \text{Blockdiag}(\boldsymbol{K}_{[1:L]\,[1:L]} - \boldsymbol{Q}_{[1:L]\,[1:L]})$. This matrix includes L diagonal matrices $\boldsymbol{\Lambda}_{l\,l}$ as:

$$\boldsymbol{\Lambda}_{l\,l} = \boldsymbol{K}_{l\,l} - \boldsymbol{K}_{l\,U}\boldsymbol{K}_{U\,U}^{-1}\boldsymbol{K}_{U\,l} \tag{5.13}$$

Note that the (positive semi-definite) covariance matrices in Eq. (5.12) have the following interpretation: the prior covariance $\boldsymbol{K}$ minus a (non-negative definite) matrix $\boldsymbol{Q}$ quantifying how much information $\boldsymbol{X}_U$ provides about the variables $\boldsymbol{Y}_{L+1}$. The distribution for $p(\boldsymbol{Y}_U|\boldsymbol{Y}_{[1:L]}) = \mathcal{N}(\hat{\boldsymbol{\mu}}_U, \hat{\boldsymbol{\Sigma}}_U)$ is given by:

$$\begin{aligned} \hat{\boldsymbol{\mu}}_U &= m\mathbf{1}_{J_U} + \hat{\boldsymbol{\Sigma}}_U\boldsymbol{K}_{U\,U}^{-1}\boldsymbol{K}_{U\,[1:L]}\boldsymbol{\Lambda}_{[1:L]\,[1:L]}^{-1}(\boldsymbol{Y}_{[1:L]} - m\mathbf{1}_{J_{[1:L]}}) \\ \hat{\boldsymbol{\Sigma}}_U &= \boldsymbol{K}_{U\,U}(\boldsymbol{K}_{U\,U} + \boldsymbol{K}_{U\,[1:L]} + \boldsymbol{\Lambda}_{[1:L]\,[1:L]}^{-1})^{-1}\boldsymbol{K}_{U\,U} \end{aligned} \tag{5.14}$$

Therefore, the posterior distribution of $\boldsymbol{Y}_{L+1}$ follows the Gaussian distribution with mean $\hat{\boldsymbol{\mu}}_{L+1}$ and covariance $\hat{\boldsymbol{\Sigma}}_{L+1}$:

$$\begin{aligned} \hat{\boldsymbol{\mu}}_{L+1} &= m\mathbf{1}_{J_{L+1}} + \boldsymbol{K}_{L+1\,U}^{-1}(\hat{\boldsymbol{\mu}}_U - m\mathbf{1}_{J_U}) \\ \hat{\boldsymbol{\Sigma}}_{L+1} &= \boldsymbol{K}_{L+1\,L+1} - \boldsymbol{K}_{L+1\,U}\boldsymbol{K}_{U\,U}^{-1}(\boldsymbol{K}_{U\,U} - \hat{\boldsymbol{\Sigma}}_U)\boldsymbol{K}_{U\,U}^{-1}\boldsymbol{K}_{U\,L+1} \end{aligned} \tag{5.15}$$

Eq. (5.15) provides the confidence limit of pixel intensities at the ROI of a newly fabricated layer if the process is in control. Note that sparse algorithms help reduce the computational complexity of the STGP model from $O({J_{[1:L]}}^3)$ to $O(J_{[1:L]}{J_U}^2)$.

The performance of STGP depends on the hyperparameters set $\boldsymbol{\Gamma}$, which can be learned from in-control measurements using maximum marginal likelihood. We include inducing points as hyperparameters into the marginal likelihood function. Also, a ridge term $\sigma_{noise}^2\mathbf{1}_{J_{[1:L]}}$ is added from the likelihood to the covariance of prior to improve the effectiveness of the estimation:

$$\begin{aligned} \log p(\boldsymbol{Y}_{L+1}|\boldsymbol{X}_U, \boldsymbol{\Gamma}) = -\frac{1}{2}(\boldsymbol{Y}_{[1:L]} - m\mathbf{1}_{J_{[1:L]}})^T(\boldsymbol{Q}_{[1:L]\,[1:L]} + \tilde{\boldsymbol{\Lambda}}_{[1:L]\,[1:L]})^{-1} \\ (\boldsymbol{Y}_{[1:L]} - m\mathbf{1}_{J_{[1:L]}}) - \frac{1}{2}\log|\boldsymbol{Q}_{[1:L]\,[1:L]} + \tilde{\boldsymbol{\Lambda}}_{[1:L]\,[1:L]}| - \frac{J_{[1:L]}}{2}\log(2\pi) \end{aligned} \tag{5.16}$$

$$\mathbf{\Gamma}^* = \text{argmax}[\log p(\boldsymbol{Y}_{L+1}|\boldsymbol{X}_U, \mathbf{\Gamma})] \tag{5.17}$$

where $\tilde{\mathbf{\Lambda}} = \mathbf{\Lambda} + \sigma^2_{noise}\mathbf{1}_{J_{[1:L]}}$. Once we have this marginal likelihood function and its derivatives, the gradient ascent algorithm is utilized to find a local optimal of function by taking iterative steps proportional to the positive local gradient.

5.3.2.3 Online update of STGP

In real-time AM process monitoring, we sequentially receive image data from a newly fabricated layer. Therefore, we introduce an online update algorithm for the sparse STGP model. Here, the layer is added to the set of in-control images if within control limits of STT^2 and STLR tests. Assume $(\boldsymbol{X}_{L+1}, \boldsymbol{Y}_{L+1})$ denotes the pixels coordinates and intensities in ROI of layer $L+1$, respectively. With the availability of the matrix inverse $\boldsymbol{K}^{-1}_{[1:L]\,[1:L]}$ and the data of a new layer, we leverage the block matrix inversion theory to perform the online update as:

$$\begin{bmatrix} \boldsymbol{K}_{[1:L]\,[1:L]} & \boldsymbol{K}_{[1:L]\,L+1} \\ \boldsymbol{K}_{L+1\,[1:L]} & \boldsymbol{K}_{L+1\,L+1} \end{bmatrix}^{-1} = \\ \begin{bmatrix} \boldsymbol{K}^{-1}_{[1:L]\,[1:L]} + \boldsymbol{K}^{-1}_{[1:L]\,[1:L]}\boldsymbol{K}_{[1:L]\,L+1}\Delta^{-1}\boldsymbol{K}_{L+1\,[1:L]}\boldsymbol{K}^{-1}_{[1:L]\,[1:L]} & {\boldsymbol{K}_{[1:L]\,[1:L]}}^{-1}\boldsymbol{K}_{[1:L]\,L+1}\Delta^{-1} \\ \Delta^{-1}\boldsymbol{K}_{L+1\,[1:L]}\ \boldsymbol{K}^{-1}_{[1:L]\,[1:L]} & \Delta^{-1} \end{bmatrix} \tag{5.18}$$

where $\Delta = (\boldsymbol{K}_{L+1\,L+1} - \boldsymbol{K}_{L+1\,[1:L]}\,\boldsymbol{K}^{-1}_{[1:L]\,[1:L]}\,\boldsymbol{K}_{[1:L]\,L+1})$. Based on the Eq. (5.14), we update the variance of inducing points $\hat{\mathbf{\Sigma}}^+_U$ as:

$$\begin{aligned} \hat{\mathbf{\Sigma}}^+_U = \hat{\mathbf{\Sigma}}_U - (&\boldsymbol{K}_{U\,L+1} - \boldsymbol{K}_{U\,[1:L]}\,\boldsymbol{K}^{-1}_{[1:L]\,[1:L]}\,\boldsymbol{K}_{[1:L]\,L+1}) \\ &(\boldsymbol{K}_{L+1\,L+1} - \boldsymbol{K}_{L+1\,[1:L]}\,{\boldsymbol{K}_{[1:L]\,[1:L]}}^{-1}\boldsymbol{K}_{[1:L]\,L+1})^{-1} \\ &(\boldsymbol{K}_{L+1\,U} - \boldsymbol{K}_{L+1\,[1:L]}\,{\boldsymbol{K}_{[1:L]\,[1:L]}}^{-1}\boldsymbol{K}_{[1:L]\,U}) \end{aligned} \tag{5.19}$$

We also update the mean for inducing points as:

$$\begin{aligned} \hat{\boldsymbol{\mu}}^+_U = (\hat{\boldsymbol{\mu}}_U - m\mathbf{1}_{J_U}) + (&\boldsymbol{K}_{U\,L+1} - \boldsymbol{K}_{U\,[1:L]}{\boldsymbol{K}_{[1:L]\,[1:L]}}^{-1}\boldsymbol{K}_{[1:L]\,L+1}) \\ &(\boldsymbol{K}_{L+1\,L+1} - \boldsymbol{K}_{L+1\,[1:L]}\,{\boldsymbol{K}_{[1:L]\,[1:L]}}^{-1}\boldsymbol{K}_{[1:L]\,L+1})^{-1} \\ &(\boldsymbol{Y}_{L+1} - \boldsymbol{K}_{L+1\,[1:L]}\,\boldsymbol{K}^{-1}_{[1:L]\,[1:L]}\,(\boldsymbol{Y}_{[1:L]} - m\mathbf{1}_{J_{[1:L]}})) \end{aligned} \tag{5.20}$$

5.3.3 Statistical monitoring of layerwise ROI

STGP model provides real-time and image-guided quantification of the ROI in a newly fabricated layer in AM. The hypothesis test of whether or not $\boldsymbol{Y}_{L+1}$ conforms to the predicted distribution can be written as:

$$H_0 : \boldsymbol{Y}_{L+1} \sim \mathcal{N}(\hat{\boldsymbol{\mu}}_{L+1}, \hat{\boldsymbol{\Sigma}}_{L+1}) \qquad H_1 : \boldsymbol{Y}_{L+1} \nsim \mathcal{N}(\hat{\boldsymbol{\mu}}_{L+1}, \hat{\boldsymbol{\Sigma}}_{L+1}) \tag{5.21}$$

where H_0 and H_1 are the null and alternative hypothesis, respectively. The STT^2 statistic is used to test the conformance of newly fabricated layer $L + 1$:

$$STT^2_{L+1} = (\boldsymbol{Y}_{L+1} - \hat{\boldsymbol{\mu}}_{L+1})^T \hat{\boldsymbol{\Sigma}}^{-1}_{L+1} (\boldsymbol{Y}_{L+1} - \hat{\boldsymbol{\mu}}_{L+1}) \tag{5.22}$$

Due to the change in ROI size in each layer, distribution of STT^2_{L+1} varies based on J_{L+1}. Therefore, we use p-value of the test statistic as the monitoring statistic.

$$p_{L+1} = 1 - F_{\chi^2}(STT^2_{L+1} | J_{L+1}) \tag{5.23}$$

The STT^2 statistic is conducive to detect an anomaly. However, the root cause analysis of changes is vital to control variations in the AM process. There are potentially three types of scenarios in layerwise AM images: shift in standard geometric profile, change in geometric variance, and shift in geometric correlation. Figure 5.5 illustrates these three types of changes in two-dimensional simulated surfaces. We also propose to design the STLR test, which provides a viable approach for root cause analysis. If we assume that when the process is out-of-control, root cause model is added to the STGP formulation, leading to:

$$y_j = f(\boldsymbol{x}_j) + \epsilon(\boldsymbol{x}_j) + \eta(\boldsymbol{x}_j) \ \forall \ j = 1, ..., J_{L+1} \tag{5.24}$$

where $\eta(.)$ denotes the added spatiotemporal deviation due to root causes. We assume this deviation is a realization of another GP with mean m_η and covariance $\boldsymbol{K}_\eta$ similar to Eq. (5.6):

$$k_\eta(\boldsymbol{x}_j, \boldsymbol{x}_{j'}) = \sigma^2_\eta \exp\Big[- (\boldsymbol{x}_j - \boldsymbol{x}_{j'})^T \times \mathrm{diag}(\boldsymbol{\theta}_3) \times (\boldsymbol{x}_j - \boldsymbol{x}_{j'}) \Big] \tag{5.25}$$

where σ^2_η and $\boldsymbol{\theta}_3$ denote variance and correlation hyperparameters, respectively. It

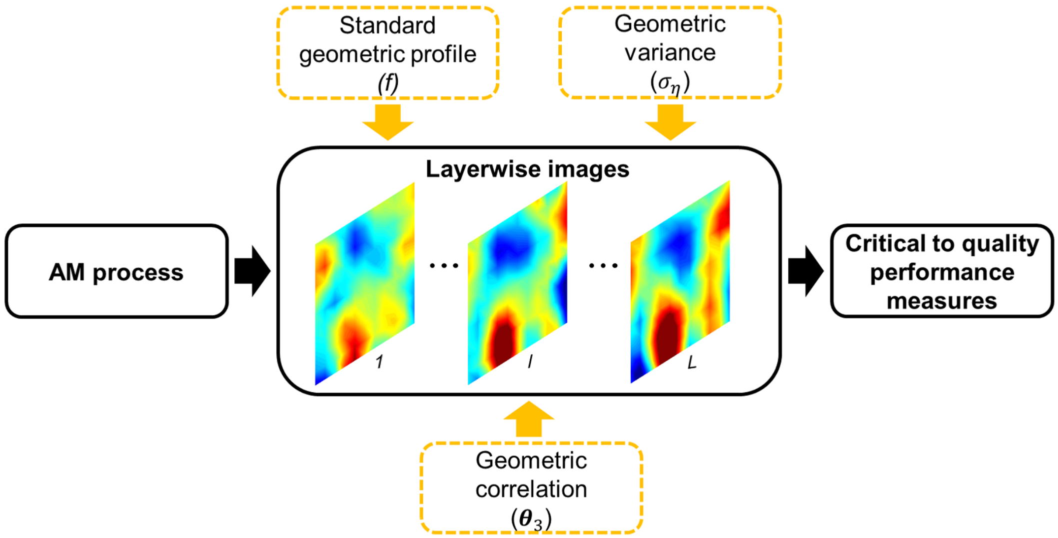

Figure 5.5. An illustration of simulated layerwise images with following types of changes: shift in standard geometric profile, shift in geometric variance, and shift in geometric correlation.

is worth mentioning that the hyperparameters of this GP correspond to different types of shift in the process. For instance, shift in geometric variance is associated with change in σ_η^2, increased in geometric correlation leads to larger elements of correlation hyperparameters (i.e., $\boldsymbol{\theta}_3$). Therefore, to test the conformance of a new layer, we can check whether the η is different from zero. The hypothesis and the STLR statistic are formulated as:

$$H_0 : \boldsymbol{Y}_{L+1} \sim \mathcal{N}(\hat{\boldsymbol{\mu}}_{L+1}, \hat{\boldsymbol{\Sigma}}_{L+1}) \quad H_1 : \boldsymbol{Y}_{L+1} \sim \mathcal{N}(\hat{\boldsymbol{\mu}}_{L+1} + m_\eta \mathbf{1}_{J_{L+1}}, \hat{\boldsymbol{\Sigma}}_{L+1} + \boldsymbol{K}_\eta) \quad (5.26)$$

$$STLR_{L+1} = 2\ln\Big[\sup_{m_\eta, \sigma_\eta^2, \boldsymbol{\theta}_3} \det(\hat{\boldsymbol{\Sigma}}_{L+1} + \boldsymbol{K}_\eta)^{-\frac{1}{2}} \exp[-(\boldsymbol{Y}_{L+1} - \hat{\boldsymbol{\mu}}_{L+1} - m_\eta \mathbf{1}_{J_{L+1}})^T (\hat{\boldsymbol{\Sigma}}_{L+1} + \boldsymbol{K}_\eta)^{-1} (\boldsymbol{Y}_{L+1} - \hat{\boldsymbol{\mu}}_{L+1} - m_\eta \mathbf{1}_{J_{L+1}})/2]\Big] - 2\ln\Big[\det(\hat{\boldsymbol{\Sigma}}_{L+1})^{-\frac{1}{2}} \exp[-(\boldsymbol{Y}_{L+1} - \hat{\boldsymbol{\mu}}_{L+1})^T \hat{\boldsymbol{\Sigma}}_{L+1}^{-1} (\boldsymbol{Y}_{L+1} - \hat{\boldsymbol{\mu}}_{L+1})/2]\Big] \quad (5.27)$$

where H_0 is the boundary of the hyperparameters space when the $\sigma_\eta^2 = 0$. As a result, the STLR statistic approximately follows 50% mixture of χ_1^2 and χ_2^2 distributions when J_s is large. When STLR statistic is larger than the control limit,

H_0 will be rejected.

$$p(STLR_{L+1} \leq z) = \frac{1}{2} \times [F_{\chi^2}(z|1) + F_{\chi^2}(z|2)] \tag{5.28}$$

Note that for STT^2 statistic, we do not need to have prior knowledge on types of possible shifts due to the fact that there is no specification of pixel distribution in the ROI of a newly fabricated layer in alternative hypothesis (i.e., $H_1 : \boldsymbol{Y}_{L+1} \nsim \mathcal{N}(\hat{\boldsymbol{\mu}}_{L+1}, \hat{\boldsymbol{\Sigma}}_{L+1})$). On the other hand, the STLR test is designed to identify particular types of root causes defined via the alternative hypothesis (i.e., $H_1 : \boldsymbol{Y}_{L+1} \sim \mathcal{N}(\hat{\boldsymbol{\mu}}_{L+1} + m_\eta \mathbf{1}_{J_{L+1}}, \hat{\boldsymbol{\Sigma}}_{L+1} + \boldsymbol{K}_\eta)$).

5.4 Experimental Design and Materials

5.4.1 Simulation Study

To demonstrate the effectiveness of our proposed method, a series of simulation studies are performed. We first show that the proposed STGP model is effective in approximating complex profiles, and then investigate the performance of different statistical monitoring tests based on the STGP model.

First, a two-dimensional sinusoid function is used to produce the desired surface of a topological representation of pixel intensities:

$$f(\boldsymbol{x}_j) = a \, \left(\sin(k_1 \, x_1^{(j)}) \cos(k_2 \, x_2^{(j)}) + \sin(k_3 \, x_1^{(j)}) \cos(k_4 \, x_2^{(j)}) \right) \tag{5.29}$$

Here, a denotes the signal amplitude and k_1, k_2, k_3, and k_4 represent the signal periods. After the simulation of a standard surface profile, we concatenate $L+1$ number of layers and construct a tensor. The spatiotemporal correlated error ϵ is generated from a GP with zero mean and covariance function with hyperparameters $\sigma_\epsilon^2 = 0.1$ and $\boldsymbol{\theta}_2 = [1, 1, 1]^T$. Also, we design an additional GP to incorporate different shift patterns into the last layer. Note that this function has the mean hyperparameter $m_\eta = 0$ and covariacne hyperparameters $\sigma_\eta^2 = 0.1$ and $\boldsymbol{\theta}_3 = [1, 1, 1]^T$.

The data of L layers are utilized for training, and the last layer (i.e., $L+1$) is implemented for estimation of uncertainty bound. We replicated this procedure for 20 times on a different number of layers, various numbers of pixels in each layer

Algorithm 2 Data generation in the simulation study

input: $J_l \quad \forall\, l \in 1, ..., L+1$ $\leftarrow$ choose the number of pixels and number of layers
$\boldsymbol{\Gamma} = [\sigma_\epsilon^2, \boldsymbol{\theta}_2]$ $\leftarrow$ initialize hyperparameters
$\boldsymbol{\Gamma}_\eta = [\sigma_\eta^2, \boldsymbol{\theta}_3]$ $\leftarrow$ initialize hyperparameters of the assignable causes

$\boldsymbol{F} \leftarrow a \left(\sin(k_1\, x_1^{(j)}) \cos(k_2\, x_2^{(j)}) + \sin(k_3\, x_1^{(j)}) \cos(k_4\, x_2^{(j)})\right) \quad \forall j = 1, ..., J_l \;\&\; l = 1, ..., L+1$ // build a tensor based on standard values
$m, m_\eta \leftarrow$ evaluate the mean functions based on hyperparameters
$\boldsymbol{K}_\epsilon, \boldsymbol{K}_\eta \leftarrow$ evaluate the covariance functions based on hyperparameters
$\boldsymbol{\zeta}_1, \boldsymbol{\zeta}_2 \leftarrow$ generate pseudo-random numbers
$[\boldsymbol{V}_1, \boldsymbol{G}_1, \boldsymbol{V}_1^T] = \mathrm{SVD}(\boldsymbol{K}_\epsilon)$ // singular value decomposition
$[\boldsymbol{V}_2, \boldsymbol{G}_2, \boldsymbol{V}_2^T] = \mathrm{SVD}(\boldsymbol{K}_\eta)$
$\boldsymbol{\epsilon} = \boldsymbol{V}_1 \times \mathrm{sqrt}(\boldsymbol{G}_1) \times \boldsymbol{\zeta}_1 + m\mathbf{1}_{J_{l[1:L+1]}}$
$\boldsymbol{\eta} = \boldsymbol{V}_2 \times \mathrm{sqrt}(\boldsymbol{G}_2) \times \boldsymbol{\zeta}_2 + m\mathbf{1}_{J_{[L+1]}}$
$\boldsymbol{Y}_{[1:L+1]} = \boldsymbol{F} + reshape(\boldsymbol{\epsilon})$
$\boldsymbol{Y}_{[L+1]} = \boldsymbol{Y}_{[L+1]} + reshape(\boldsymbol{\eta})$

Output: $\boldsymbol{Y}_{[1:L+1]}$

and different percentage of inducing points, and estimated the root mean squared error (RMSE) as the performance measurement. We also perform a comparison study with a fully independent training condition (FITC) as a popular sparse GP method [174]. The FITC model assumes $y_j = f(\boldsymbol{x}_j) + \xi \;\forall j = 1, ..., J_l\,;\; l = 1, ..., L$. Particularly, a sparse GP is still utilized to estimate the standard profile and deviation functions $f(\boldsymbol{x}_j)$ simultaneously and an i.i.d. noise (i.e., ξ) is employed to characterize the randomness in each point of surface. In other words, the FITC model assumes the constant standard surface is mixed with the variability of the process. However, the non-constant standard surface with the spatiotemporal correlations can lead to a significant change in intensity of pixels over layers.

As shown in Figure 5.6, we examine different shift patterns with various magnitudes using STT^2 and STLR tests to find the capability of the proposed model. Here, the shift in standard geometric profile is related to a change in signal amplitude of the standard surface profile. Geometric variance and geometric correlation correspond to changes in values of variance and correlation hyperparameters (i.e., σ_η^2 and $\boldsymbol{\theta}_3$) in the function of assignable causes (i.e., $\eta(.)$). We also compare the monitoring results of the STGP with FITC under different sparsity levels, various sizes of pixels, and number of layers.

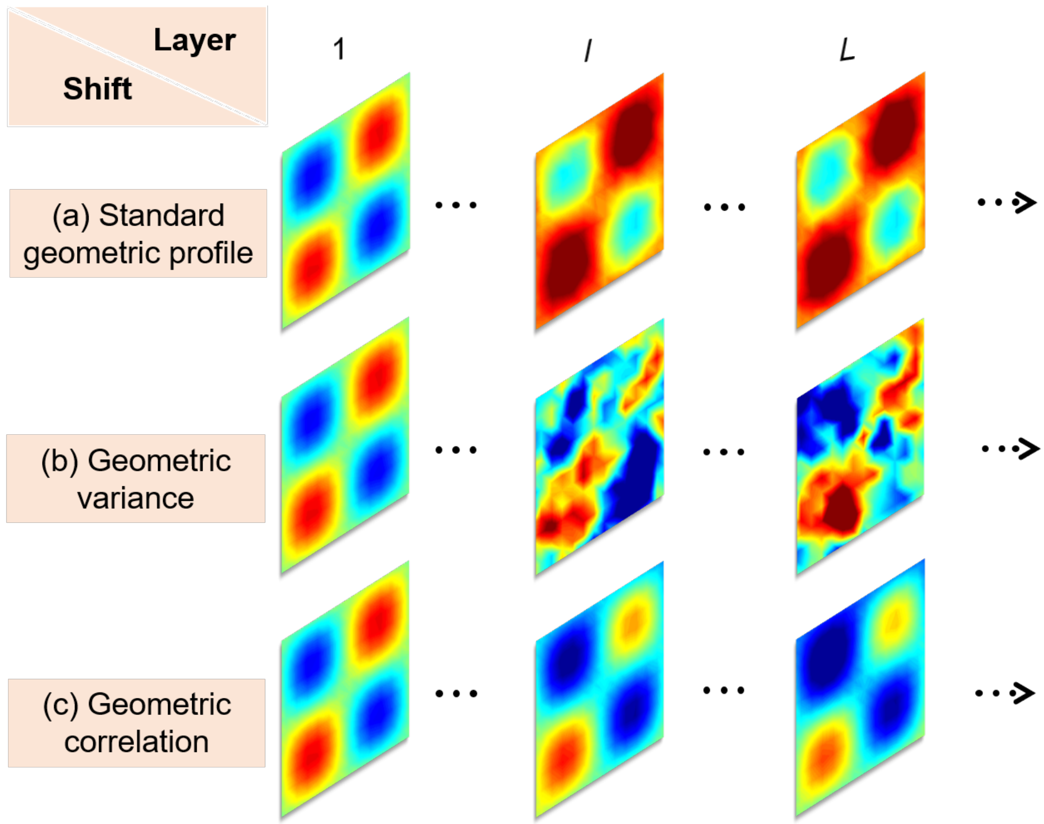

Figure 5.6. Simulated layerwise images with (a) standard geometric profile shift, (b) geometric variance shift, and (c) geometric correlation shift.

5.4.2 Real-world Case Study

A real-world case study is performed on an EOSINT M 280 LPBF machine. The input material was a Titanium alloy, Ti-6Al-4V, also known as ASTM B348 Grade 23 powder material, which has a particle size between 14 μm to 45 μm. The parameter settings of the machine are as follows: laser power 340 W, laser velocity 1250 mm/s, and hatching spacing 0.12 mm. The advanced imaging system that is integrated with the LPBF machine is shown in Figure 5.1(b).

Figure 5.7 shows the geometry of drag link joint build, which has an enclosing box dimension of 23.7 mm $\times$ 13.3 mm $\times$ 27.3 mm, with the 60 μm layer thickness. Intentional flaws are embedded in the build at four different locations along the build-up direction by eliminating material that intersected with cubical and cylindrical patterns. Flaw patterns consist of 50 μm, 250 μm, 500 μm, and 750 μm cubical and cylindrical shapes, which are centered in the z plane direction. Cylindrical

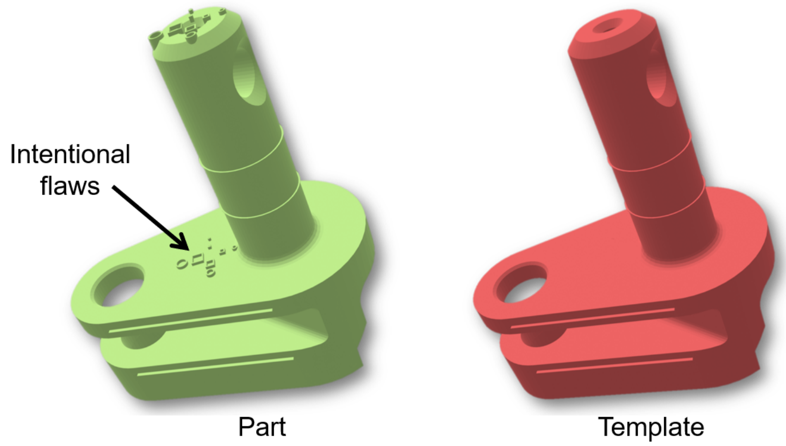

Figure 5.7. Locations of intentional flaws in 3D digital design of the drag link joint build.

flaws with the diameter of 50 μm, 250 μm, 500 μm, and 750 μm are also placed in the part. These intentionally embedded flaws represent the lack-of-fusion flaws that happen in the LPBF process, i.e., small zones of infused material placed in a component. A DSLR camera (i.e., Nikon D800E) with a resolution of 36.3 megapixels captures layerwise image profiles of the powder bed.

5.5 Experimental Results

5.5.1 Simulation Study

5.5.1.1 Performance of STGP estimation

As shown in Figure 5.8, the STGP model is effective to approximate the complex standard profile and quantify in-control variations from a group of layerwise surfaces with spatiotemporally correlated errors. The STGP model leverages the previous layerwise images (i.e., L layers) to estimate the distribution (i.e., mean and variance) of the newly fabricated layer (i.e., $L+1$). The STGP model has a sparse and online structure to deal with the multi-layer production process and tackle the high-dimensionality of layerwise AM images. Note that STGP provides confidence bound for the newly fabricated layer and is conducive to process monitoring of a stream of layerwise and correlated images. Based on Algorithm 1, we generate 10 layerwise surfaces with the size 20×20. The first 9 layers are utilized to approximate the last layer.

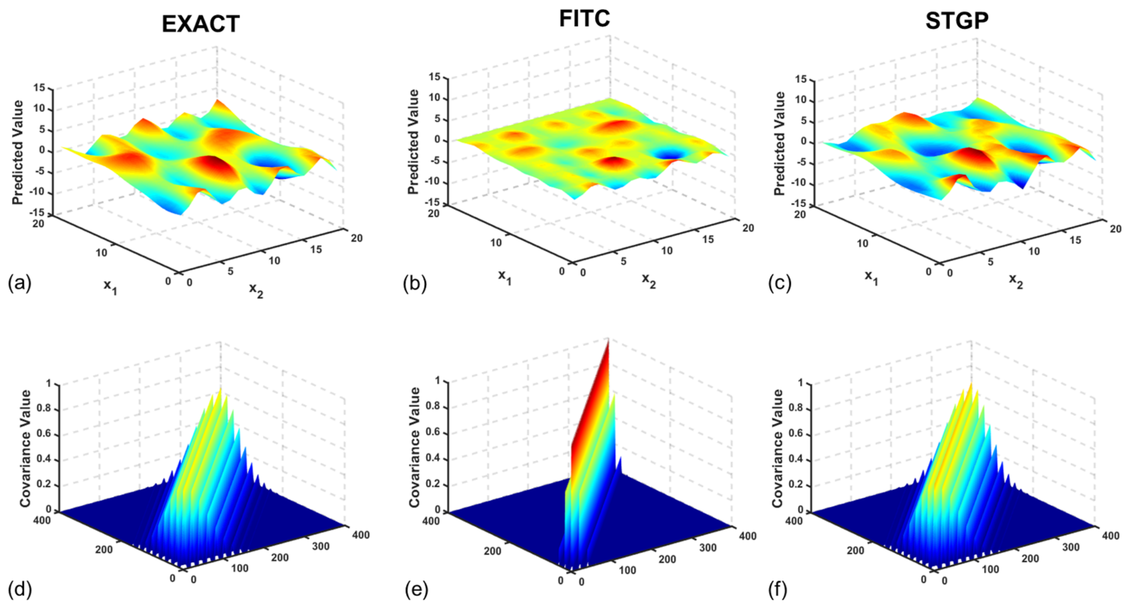

Figure 5.8. Predicted means and covariances using STGP and FITC models: (a) Exact profile, (b) Predicted profile using FITC, (c) Predicted profile using STGP, (d) Exact covariance, (e) Predicted covariance using FITC, and (f) Predicted covariance with the STGP.

As shown in Figure 5.8(a)-(c), the difference between mean estimation from STGP and FITC is significant. Note that the mean distribution of STGP is very close to the exact function. More quantitatively, the mean prediction from the STGP model has an RMSE of 0.79, whereas the RMSE of FITC is 1.10. Also, in terms of covariance structure, Figure 5.8(e) clearly shows that the FITC model failed to predict the correct structure. This is simply because our simulation model includes a correlated noise, whereas the FITC model with i.i.d. noise assumption is no longer valid for the simulated data. In contrast, covariance prediction from STGP (Figure 5.8(f)) is much closer to the exact case (Figure 5.8(d)). This comparison demonstrates that STGP is effective in the prediction of both mean and covariance functions. Therefore, the proposed methodology effectively handle complex profiles with spatiotemporally correlated deviation.

As shown in Table 5.2, RMSE decreases when the sample size increases. Note that RMSE is smaller for a larger number of pixels or a higher percentage of

Table 5.2. The performance comparison of FITC and STGP in the simulation study under different number of pixels and percentage of inducing points in each layer.

Number of pixels	Percentage of inducing points	RSME	
		FITC	STGP
10 ×10	6%	1.37 (±0.42)	1.32 (±0.57)
	25%	1.19 (±0.29)	1.10 (±0.56)
	56%	1.17 (±0.30)	0.88 (±0.71)
20 ×20	6%	1.34 (±0.10)	1.28 (±0.10)
	25%	1.19 (±0.38)	1.01 (±0.67)
	56%	1.17 (±0.47)	0.78 (±0.61)
30 ×30	6%	1.37 (±0.71)	1.20 (±0.96)
	25%	1.19 (±0.34)	0.99 (±0.19)
	56%	1.10 (±0.38)	0.74 (±0.10)

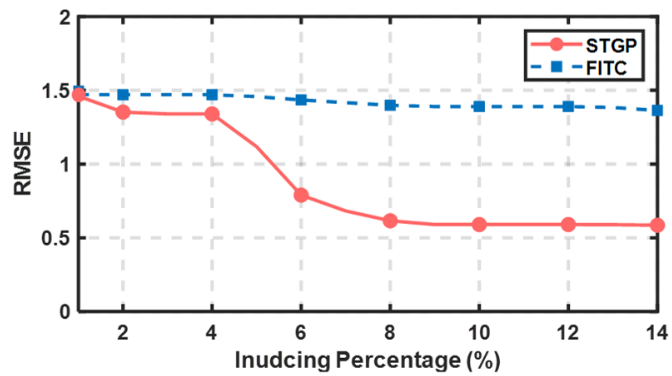

Figure 5.9. The variations of RMSE for STGP and FITC with different percentages of inducing points in estimation of pixel distribution of the new layer.

inducing points. Also, a larger percentage of U leads to more accurate estimation of a layer in comparison with a larger number of pixels. Results show that the prediction performance of STGP improves as the size of layers increases, while the performance level of FITC stays the same. Note that the proposed STGP incorporates the layerwise dependencies into the estimation, thereby providing a better prediction about the distribution of pixels in a new layer.

As shown in Figure 5.9, the error rate of the STGP drastically drops as the percentage of inducing points in each layer increases. However, the RMSE of FITC does not significantly change as we use more pixels information as inducing points. The result shows that 9% of pixel information in the set of in-control layers leads to the low RMSE for the estimation of a newly added layer.

5.5.1.2 Performance of statistical monitoring

The simulation study is performed under the condition that statistical tests for the ideal case when the hyperparameters of STGP (i.e., both for $f(x)$ and $\epsilon(x)$) are unknown. We conduct an experiment to test the performance of two monitoring methods in detecting different types of change, including shift in standard geometric profile, geometric variance, and geometric correlation. We utilize the same standard profile and spatiotemporal process, as developed in Section 5.3.2. Note that 10 layers with the size of 20×20 are generated, where the first 9 layers are assigned to the in-control set. Also, 9% of pixels in each layer of the in-control set are selected as inducing points. The control limits for STT^2 and STLR tests are obtained from the $\chi^2_{J_{L+1}}$ and 50% mixture of χ^2_1 and χ^2_2, respectively. The control limits of statistical tests are calculated with the type I error $\alpha = 0.05$.

To perform a comparison of the capability of different testing methods, we consider the intensity range in a layerwise profile (i.e., the difference between the maximum and minimum response values) as another statistical method. When the range value passes specific control limit value (i.e., average variations in a pixel/point in the set of in-control layers), the process is defined as out of control. We compare the performance of these three tests for the shift in geometric profile, geometric variance, and geometric correlation using the defined control limits. The type II error is calculated for each shift scenario. Figure 5.10 shows the operation characteristic (OC) curves of different types of shifts under three statistical monitoring tests.

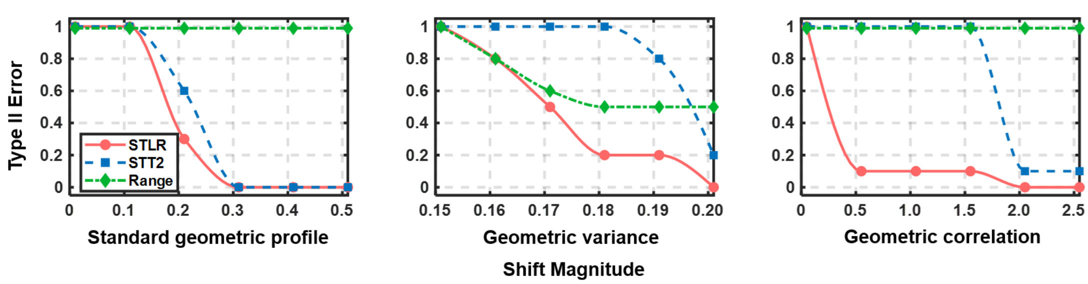

Figure 5.10. Performance comparisons of type II error for STT^2, STLR and Range tests in detecting the shift of geometric profile, geometric variance and geometric correlation with different magnitudes.

As shown in Figure 5.10, both STT^2 and STLR tests are able to detect the geometric profile shift better than the Range test. This is related to the significant change in the response values in the test layer, which is not difficult to detect by

STT^2 and STLR. However, the STLR test shows higher sensitivity than STT^2 in detecting geometric variance and geometric correlation changes especially when the shift magnitude is small. The range test is not capable of finding the geometric variance and geometric correlation shifts due to the fact that the difference between the largest and smallest indecencies remain the same when σ_η^2 and $\boldsymbol{\theta}_3$ change (see Algorithm 1).

We further investigate the performance of the statistical monitoring by studying the EXACT model (i.e., when the standard function $f(x)$ and parameters of $\epsilon(x)$ are known). Note that under this condition, measurements $\boldsymbol{Y}_{L+1}$ at locations $\boldsymbol{X}_{L+1}$ follow the Gaussian distribution with mean and covariance $\boldsymbol{f}_{L+1} = [f(\boldsymbol{x}_1), ..., f(\boldsymbol{x}_{J_{L+1}})]$ and $\boldsymbol{\Sigma}_{L+1} = [k_f(\boldsymbol{x}_j, \boldsymbol{x}_{j'})]_{J_{L+1}\times J_{L+1}}$, respectively. Also, the STT^2 statistic is denoted as $STT^2_{L+1} = (\boldsymbol{Y}_{L+1} - \boldsymbol{f}_{L+1})^T \boldsymbol{\Sigma}_{L+1}{}^{-1}(\boldsymbol{Y}_{L+1} - \boldsymbol{f}_{L+1})$. The STLR statistic can be rewritten as follows:

$$
\begin{aligned}
STLR_{L+1} = 2 \ln\Big[\sup\nolimits_{m_\eta, \sigma_\eta^2, \boldsymbol{\theta}_3} \det(\hat{\boldsymbol{\Sigma}}_s + \boldsymbol{K}_\eta)^{-\frac{1}{2}} \exp[-(\boldsymbol{Y}_{L+1} - \boldsymbol{f}_{L+1} - m_\eta \mathbf{1}_{J_{L+1}})^T \\
(\hat{\boldsymbol{\Sigma}}_{J_{L+1}} + \boldsymbol{K}_\eta)^{-1}(\boldsymbol{Y}_{L+1} - \boldsymbol{f}_{L+1} - m_\eta \mathbf{1}_{J_{L+1}})/2] - 2 \ln\Big[\det(\hat{\boldsymbol{\Sigma}}_{L+1})^{-\frac{1}{2}} \\
\exp[-(\boldsymbol{Y}_{L+1} - \boldsymbol{f}_{L+1})^T \hat{\boldsymbol{\Sigma}}_{L+1}^{-1}(\boldsymbol{Y}_{L+1} - \boldsymbol{\mu}_{L+1})/2]\Big]
\end{aligned} \tag{5.30}
$$

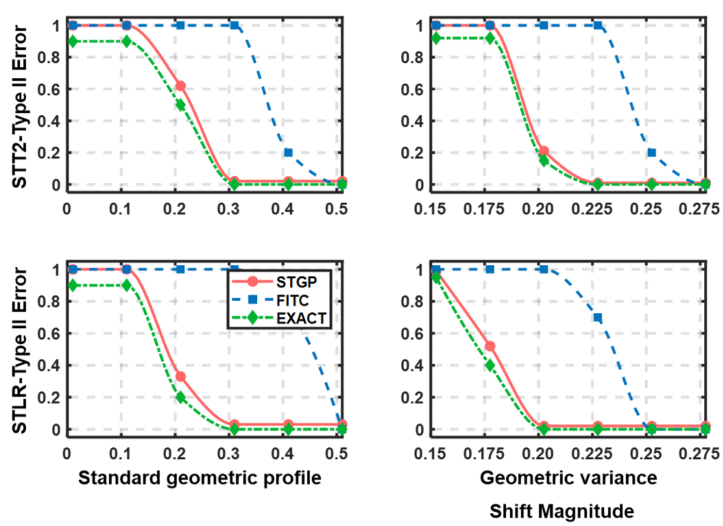

Figure 5.11. OC curves of STT^2 and STLR tests when EXACT, STGP, and FITC models are utilized.

As shown in Figure 5.11, the average differences in type II error between STGP and EXACT for STT^2 and STLR tests are 0.08 and 0.05, respectively. On the other hand, the type II error for FITC is significantly larger than the EXACT case. The differences between the EXACT and FITC for the STT^2 and STLR are 0.43 and 0.36, respectively. Simulation results show that the STGP model has a higher capability to estimate complex profiles with spatiotemporal dependency. Therefore, STT^2 and STLR control charts yield a superior monitoring performance of various changes such as in standard geometric profile and geometric variance.

5.5.2 Real-world Case Study

Further, we implement the online STGP methodology to monitor the quality of ROIs in layerwise images from the real-world case study in the LPBF process. It is worth mentioning that ROIs of 60 layerwise images are utilized in this experiment, which includes 16 out of control ROIs. For process monitoring of an ROI, the previous 7 in-control ROIs are identified and are used as training samples. Then, the conformity of the newly added ROI is tested based on the proposed STGP using STT^2 and STLR tests. If the ROI is defined as in control, then this new layer is added to the in-control set. The number of in-control layers is set to be 7 because of the layerwise correlation tends to be smaller if beyond 7 layers, compared to the spatial correlation within an ROI. This smaller layer-to-layer dependency is due to the cooling phenomena during spreading powder for fabricating the next layer in the LPBF process [175]. Although we chose 7 layers for the in-control set (i.e., $7 \times 60\,\mu\text{m} = 0.42$ mm in the z-direction), the proposed STGP is capable of adjusting the temporal correlations and defining an optimal number of dependent layers using hyperparameter optimization. Note that the number of pixels in ROIs of drag link joint build has one of the following values: 22916, 8946, 28723, 44257, to 4709. Also, 9% of pixels in each layer of the in-control set is used as inducing points. The data are utilized to learn the hyperparameters of the STGP model.

The standard surface for ROIs is complex because the presence of various factors (e.g., machine, process, design, and material) results in variations in the AM process and cause non-homogeneity in the distribution of pixels. Furthermore, time-varying temperature distributions on the surface and internal structure of AM build creates spatiotemporal dependencies and leads to the propagation of flaws from previous layers into the new layer. However, if the deviation from the standard surface profile is acceptable, then the ROI can be presumed in control. Note that the first GP module captures the standard surface profile and the second GP module estimates spatiotemporal deviations between in-control ROIs and the standard surface profile to quantify variations in the process. Results show that patterns in ROIs images are consistent with the spatiotemporal assumption in the STGP model.

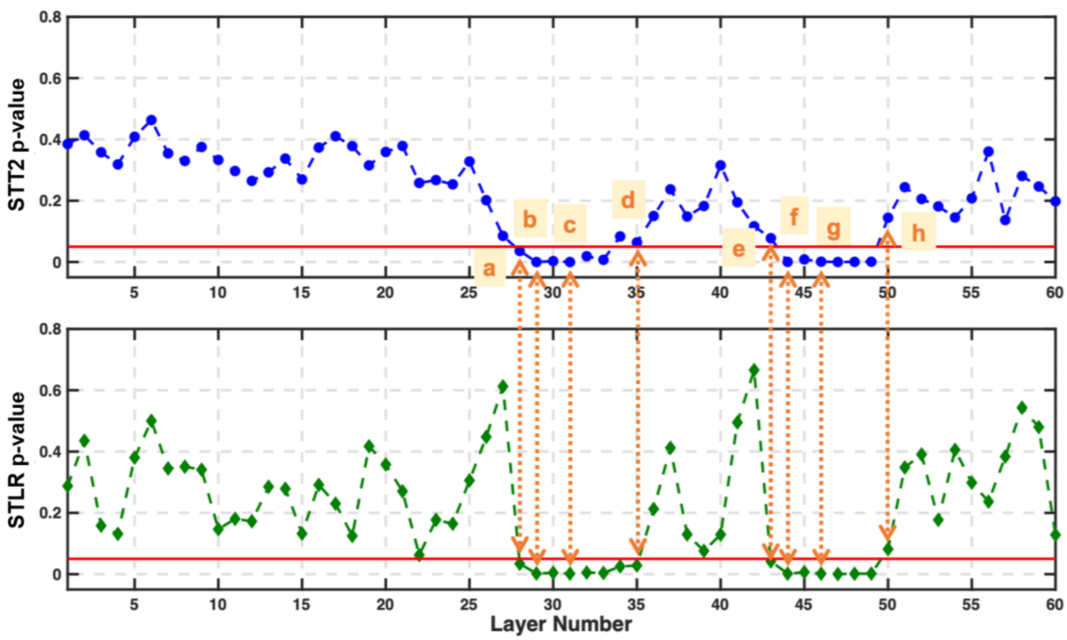

Figure 5.12. The p-values of (a) STT^2, and (b) STLR tests on the sequence of 60 layerwise images with variant geometry and spatiotemporal correlations in the drag link joint build.

As shown in Figure 5.12, a pixel value in the newly fabricated layer is not only influenced by spatially correlated pixels in the same layer, but also by pixels in adjacent layers. Here, most of ROIs follow the standard surface profile with acceptable variations. However, there are a few ROIs that both STT^2 and STLR tests detect nonconformity due to the presence of flaws (e.g., cubic or cylindrical areas with the lack of fusion).

As shown in Figure 5.13 (a)-(g), the proposed STGP detects ROIs with flaws. We observe that the value of the STLR test for ROI of layer 28 (see Figure 5.12) is close to the control limit, while this ROI passes the STT^2 test. The result shows that there is a spatial-layerwise shift that leads the STLR test to generate the value close to its control limit. In Figure 5.13 (d), the pixel distribution for out-of-control

ROIs are different than in-control ROIs. In other words, the spatial correlation within a layer generates regions with a flaw, which have a lower pixel intensity in comparison with the other regions in an ROI. Also, the temporal dependency of ROIs causes the propagation of flaws from a defective layer to the antecedent layers. The spatiotemporal dependency poses a challenge on the layerwise quality monitoring using existing methods. For example, the FITC model does not account for the spatiotemporal correlations of the data, which creates a considerable number of false alarms.

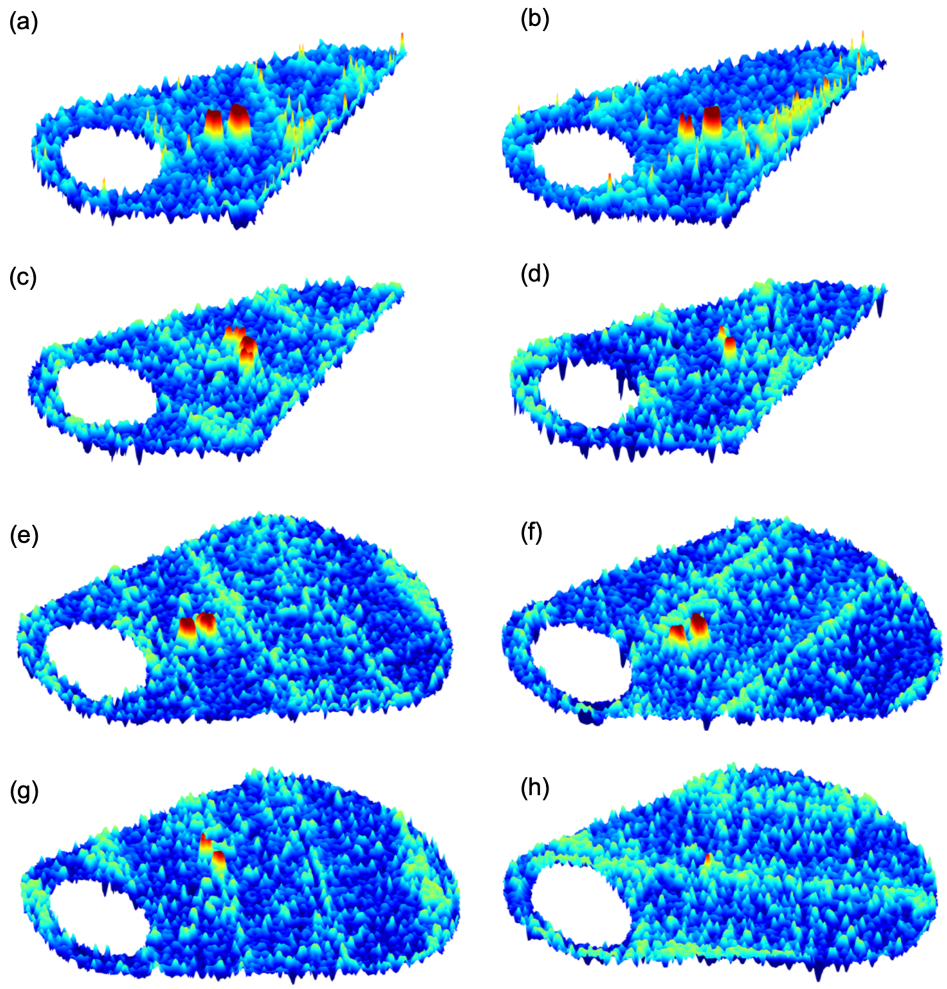

Figure 5.13. Image ROIs that failed the tests in the layer number: (a) 28, (b) 29, (c) 31, (d) 35, (e) 43, (f) 44, (g) 46, and (h) 50.

5.6 Conclusions

Large amounts of imaging data collected during AM fabrication have motivated a thorough study for image-guided AM process monitoring and control. However, most of previous investigations in AM monitoring of variant geometry are less concerned about the spatiotemporal correlation among layerwise images. Also, conventional methods in image monitoring are not designed to cope with layer to layer geometry variations. This study presents a new STGP methodology to model the correlations within ROIs of layerwise images for AM process monitoring and control. The STGP consists of two GP modules that simultaneously models the standard spatial profile and spatiotemporal AM deviations. Further, sparse algorithms and online updating are designed to tackle the curse of dimensionality in high-dimensional layerwise AM images and cope with the complexity in the manufacturing process. Based on STGP predictions, STT^2 and STLR charts are developed to test the conformity of the ROI of a newly produced layer. Numerical simulations demonstrated that the proposed methodology is effective in capturing different process shifts, including standard geometric profile, geometric variance, and geometric correlation. Also, experimental results of real-world case study show the strong potential of STGP for image-guided monitoring of variant geometry in the LPBF process. The proposed methodology can also be generally applicable to a variety of engineering and medical domains that entail imaging profiles with variant geometry.

Chapter 6
Conclusions and Future Research

6.1 Research Summary

Advanced sensing provides unprecedented opportunities for data-driven monitoring, modeling, and control of complex manufacturing systems for quality improvements. Realizing full potentials of sensing data depends to a great extent on developing novel analytical methods and tools for effective system informatics and control.

- Advanced imaging brings a large amount of data with nonlinear and nonhomogeneous patterns, which calls for effective analytical methods to exploit knowledge and extract sensitive features for process monitoring and control.
- Image data provide a unique opportunity to quantify the effect of process conditions on part quality in manufacturing processes. New statistical approaches are urgently needed to quantify the effect of process conditions on quality of final builds in complex manufacturing systems.
- Current sensor-based learning methodologies are not designed to leverage generated data in manufacturing environments (e.g., the dearth of training data due to the one-of-a-kind manufacturing or complex geometry of build). There is a dire need for new analytical methods customized for advanced manufacturing environments to perform real-time anomaly detection.
- In-situ sensing leads to the proliferation of spatiotemporal data. Both spatial and temporal correlations need to be efficiently addressed for high-dimensional predictive modeling.

My research goal is to develop innovative methodologies for real-time modeling, monitoring, and control of advanced manufacturing systems using generated sensing data. As shown in Figure 6.1, my research objective is to integrate process knowledge with learning models and create enabling methodologies for process optimization, surface characterization, flaw detection, and quality monitoring. **Contributions** of this dissertation are summarized as follows:

- In chapter 2, we investigated the effect of process conditions on lack of fusion porosity in parts made using LPBF process. In pursuit of this goal, the objectives of this work are twofold: 1) quantify the count (number), size and location of pores as a function of three LPBF process parameters, namely, the hatch spacing, laser velocity, and laser power; 2) monitor and identify process conditions that are liable to cause porosity through analysis of in-process layer-by-layer optical images of the build invoking multifractal and spectral graph theoretic features.

- In Chapter 3, the joint multifractal and lacunarity methodology is developed to characterize and identify the defects in UPM and AM processes from images. 1) multifractal analysis captures nonlinear and irregular patterns of UPM images, which is further represented in the form of multifractal and lacunarity spectrum; 2) we also investigate the effect of LPBF process printing conditions on the multifractal and lacunarity characterization results of defect patterns in AM images.

- In Chapter 4, a new image-based learning approach is developed for real-time flaw detection in customized AM builds, which have a high level of layer-to-layer geometry variation. 1) we leverage the computer-aided design (CAD) file to perform shape-to-image registration and delineate the regions of interests in layerwise images; 2) a hierarchical dyadic partitioning methodology is developed to split layer-to-layer regions of interest into subregions with the same number of pixels to provide freeform geometry analysis; 3) a semiparametric model is designed to characterize the complex spatial patterns in each customized subregion and boost the computational speed; 4) a DNN model is designed to learn and detect fine-grained information of flaws.

- In Chapter 5, a new STGP methodology is introduced to model the evolving dynamics within ROIs of layerwise images for AM process monitoring and control. 1) the STGP consists of two GP modules that simultaneously models the standard spatial profile and spatiotemporal AM dynamics; 2) sparse algorithms and online updating are designed to tackle the curse of dimensionality in high-dimensional layerwise AM images and cope with the complexity in the manufacturing process; 3) based on STGP predictions, STT^2 and STLR charts are developed to test the conformity of the ROI of a newly produced layer.

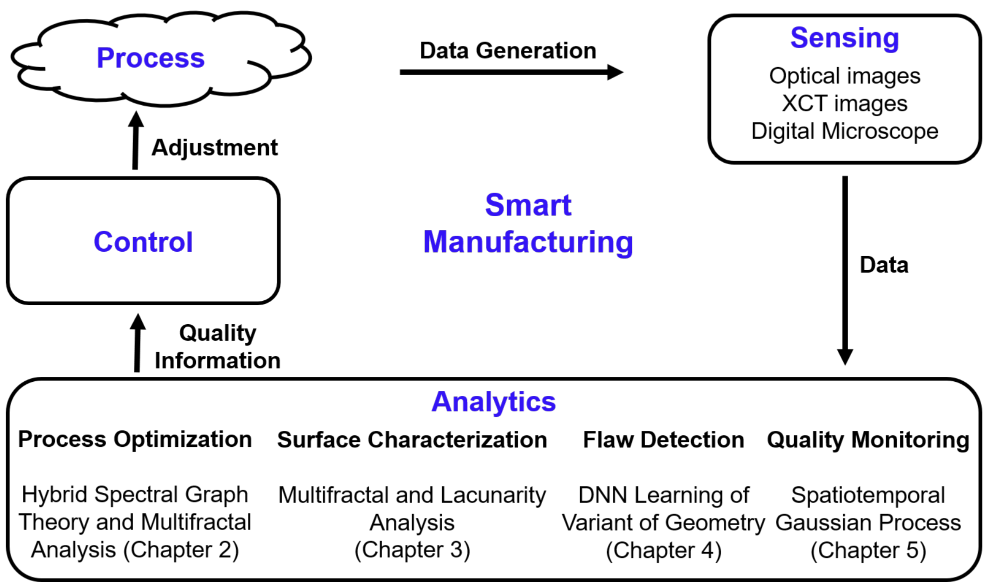

Figure 6.1. The proposed framework to build a basis for smart manufacturing.

6.2 Future Investigations

Based on the developed methodologies in this dissertation, there are some research topics that deserve further investigations, including:

- *Process Optimization*: 1) one limitation of this work is that it does not relate the sensor signatures directly to the defects, but rather isolates the process condition that leads to porosity. This is mainly due to the fact that the resolution of the camera is not sufficient to identify pores, which are in the 16-65 μm, from the images directly. To overcome this drawback, data from multiple sensors will be combined (e.g., thermography and meltpool monitoring) to not only capture multiple types of defects simultaneously but also improve upon the detection fidelity. 2) understanding the effect of process parameters on other types of defects, such as distortion and geometric inaccuracy is the current gap in the literature.

- *Surface Characterization*: 1) the current multifractal and lacunarity analysis is designed to work with grayscale images. However, converting a color image to grayscale to characterize surfaces or layers causes a significant loss of information. As a result, the extent of the scaling range is crucial. The future direction can be focused on developing a novel technique for estimating the multifractal dimension of color images. 2) The current fractal analysis does not provide the certainty level in the dimensional estimation. The integration of the error bars with fractal results in reliable analysis. 3) the current multifractal analysis depends on the geometry of layerwise images. New partitioning methods are required to perform freeform geometry analysis before estimation of fractal dimension.

- *Flaw Detection*: 1) high levels of noise, blur, and brightness have a detrimental effect on the performance of DNN models. Limited work has devoted to the systematical assessment of the robustness of deep learning models for flaw detection against source of variations in AM settings. For instance, hatching pattern in the LPBF process leads to a significant change in the morphology of layerwise images. Accurate flaw detection in AM using DNN methodologies needs to resolve this variation problem. 2) in this study 8 features such as mean and standard deviation of pixel intensities in ROI of layerwise images are extracted and fed into the classification models for flaw detection. Future studies will be conducted to capture other types of statistics for a comprehensive comparison. For example, network topological metrics (e.g., density and degree, betweenness, pagerank, closeness, and eigenvector centralities) as well as wavelet coefficients can be extracted to compare the DNN-based approach and other methods.

- *Quality Monitoring*: 1) in the proposed STGP model, the more inducing points, the better capability of storing information. However, after a certain number of inducing input points, the additional 'information gain' seems to be minimal. At the same time, using more inducing input points does significantly increase the computational complexity of the model. The future research direction can be investigated in determining the optimal number of inducing points using Kullback–Leibler divergence. 2) the run time of STGP model tends to be large when there is a high number of inducing points. The main idea here is that we do not need the full matrix between inducing points. In other words, when two inducing input points are far apart, then the covariance value will be close to zero, even before we start incorporating measurement data. Therefore, we can use this idea to improve computational cost. 3) the capability of sensors in capturing various flaws is not similar. This, in turn, introduces uncertainty in AM process measurements. Future research needs to be conducted to integrate the sensors' capability with monitoring methodologies for accurate quality control in AM.

6.3 Future Directions

My future research plans include:

- *Sensor-based Modeling of Spatiotemporal Thermal Effects in Additive Manufacturing*: In the metal AM process, 3D parts are fabricated with the laser power source to fuse powders together, namely micro-welding. Non-homogenous heating and cooling phenomena often lead to anisotropic residual stresses, resulting in defective products. The temperature distribution within the AM build is critical to realizing high-fidelity control of the strength, residual stress, and microstructures in fabricated products. However, AM parts generally have complex 3D geometries and are manufactured layer-by-layer, which leads to time-varying temperature distributions on the surface and in the internal structure. My research objective is to develop new statistical models of thermal effects in 3D parts for process control. Specifically, this research aims to 1) model the heat transfer dynamics from the surface layer to the internal structure; 2) introduce sensor-based modeling of thermal distribution under uncertainty; 3) extend the spatiotemporal Gaussian process model developed in Chapter 5 to represent joint spatial and temporal structures in thermal data for real-time process monitoring and control. This research will provide novel analytical models to advance the understanding of process dynamics in

AM, and further, enable real-time process modifications for efficient quality control of AM builds.

- *Multi-Task/Transfer Learning in Additive Manufacturing*: High-dimensional sensing data (e.g., image profiles) provide rich information about the dynamics of AM processes. However, a high level of customization in AM leads to the lack of data for learning the underlying processes and thereby causing shallow learning. This project will develop multi-task/transfer learning methods that systematically explore the correlations between different sets of AM data and incorporate them efficiently for enhancing the accuracy of the learning/decision making. I plan to develop an augmented Gaussian process as a surrogate model for representing the objective function of all tasks to integrate the prior knowledge to compensate for the generalization performance loss. Specifically, this research aims to 1) establish geometric representations for optimizing material support during AM processes; 2) develop an optimal decision-making approach for material selection under different AM processes, designs and machines; 3) create a real-time flaw detection framework that generalizes flaw information (e.g., crack, porosity, and lack of fusion) from one setting to another. This research provides novel real-time multi-task/transfer learning techniques for enhancement of the accuracy of the machine learning tools.

Appendix

Hyperparamters Optimization in Chapter 5

To estimate hyperparameters of STGP model from in-control set, we need to maximize the log-likelihood function to best explain the observations.

$$\log p(\boldsymbol{Y}_{L+1}|\boldsymbol{X}_U, \boldsymbol{\Gamma}) = -\frac{1}{2}(\boldsymbol{Y}_{[1:L]} - m\mathbf{1}_{J_{[1:L]}})^T(\boldsymbol{Q}_{[1:L]\,[1:L]} + \tilde{\boldsymbol{\Lambda}}_{[1:L]\,[1:L]})^{-1}$$
$$(\boldsymbol{Y}_{[1:L]} - m\mathbf{1}_{J_{[1:L]}}) - \frac{1}{2}\log|\boldsymbol{Q}_{[1:L]\,[1:L]} + \tilde{\boldsymbol{\Lambda}}_{[1:L]\,[1:L]}| - \frac{J_{[1:L]}}{2}\log(2\pi)$$

where the first section in the above equation is the data fit term. The second part is the complexity penalty that prevents over fitting and the last section denotes the normalization constant. The above equation can be rewritten as follows if we define $\tilde{\boldsymbol{K}}_{[1:L]\,[1:L]} = \boldsymbol{Q}_{[1:L]\,[1:L]} + \tilde{\boldsymbol{\Lambda}}_{[1:L]\,[1:L]}$ as:

$$\log p(\boldsymbol{Y}_{L+1}|\boldsymbol{X}_U, \boldsymbol{\Gamma}) = -\frac{1}{2}(\boldsymbol{Y}_{[1:L]} - m\mathbf{1}_{J_{[1:L]}})^T\tilde{\boldsymbol{K}}^{-1}_{[1:L]\,[1:L]}(\boldsymbol{Y}_{[1:L]} - m\mathbf{1}_{J_{[1:L]}})$$
$$-\frac{1}{2}\log|\tilde{\boldsymbol{K}}_{[1:L]\,[1:L]}| - \frac{J_{[1:L]}}{2}\log(2\pi)$$

We derive the optimal value of hyperparameters with the help of the following theorems.

Theorem 1: For any invertable matrix $\tilde{\boldsymbol{K}}_{[1:L]\,[1:L]}$ and any hyperparamters θ, the derivative of $\tilde{\boldsymbol{K}}^{-1}_{[1:L]\,[1:L]}$ with respect to the hyperparamter equals:

$$\frac{d\,\tilde{\boldsymbol{K}}^{-1}_{[1:L]\,[1:L]}}{d\,\theta} = -\tilde{\boldsymbol{K}}^{-1}_{[1:L]\,[1:L]}\,\frac{d\,\tilde{\boldsymbol{K}}_{[1:L]\,[1:L]}}{d\,\theta}\,\tilde{\boldsymbol{K}}^{-1}_{[1:L]\,[1:L]}$$

Proof: Consider the relation $\tilde{\boldsymbol{K}}_{[1:L]\,[1:L]}\, \tilde{\boldsymbol{K}}^{-1}_{[1:L]\,[1:L]} = \mathbf{I}$. If we take the derivative of both sides and utilizing the chain rule, we have:

$$\frac{d\,\tilde{\boldsymbol{K}}_{[1:L]\,[1:L]}}{d\,\theta}\tilde{\boldsymbol{K}}^{-1}_{[1:L]\,[1:L]} + \tilde{\boldsymbol{K}}_{[1:L]\,[1:L]}\,\frac{d\,\tilde{\boldsymbol{K}}^{-1}_{[1:L]\,[1:L]}}{d\,\theta} = 0$$

Solving the above equation for the $\frac{d\,\tilde{\boldsymbol{K}}^{-1}_{[1:L]\,[1:L]}}{d\,\theta}$ directly proves the theorem.

Theorem 2: For any invertible matrix $\tilde{\boldsymbol{K}}_{[1:L]\,[1:L]}$, the derivative of $|\tilde{\boldsymbol{K}}_{[1:L]\,[1:L]}|$ is given by:

$$\frac{d\,|\tilde{\boldsymbol{K}}_{[1:L]\,[1:L]}|}{d\,\theta} = |\tilde{\boldsymbol{K}}_{[1:L]\,[1:L]}|\,\mathrm{tr}(\tilde{\boldsymbol{K}}^{-1}_{[1:L]\,[1:L]}\,\frac{d\,\tilde{\boldsymbol{K}}_{[1:L]\,[1:L]}}{d\,\theta})$$

Proof: This theorem is a special case of Jacobian's formula.

The helpful consequence of the above theorem is:

$$\frac{d\log|\tilde{\boldsymbol{K}}_{[1:L]\,[1:L]}|}{d\,\theta} = \mathrm{tr}(\tilde{\boldsymbol{K}}^{-1}_{[1:L]\,[1:L]}\,\frac{d\,\tilde{\boldsymbol{K}}_{[1:L]\,[1:L]}}{d\,\theta})$$

Therefore, the derivatives of the log-likelihood function with respect to the hyperparameters θ_i:

$$\begin{aligned}\frac{\partial\log p(\boldsymbol{Y}_{L+1}|\boldsymbol{X}_U,\boldsymbol{\Gamma})}{\partial\theta_i} &= \frac{1}{2}(\boldsymbol{Y}_{[1:L]} - m\mathbf{1}_{J_{[1:L]}})^T(\tilde{\boldsymbol{K}}^{-1}_{[1:L]\,[1:L]}\,\frac{\partial\,\tilde{\boldsymbol{K}}_{[1:L]\,[1:L]}}{\partial\theta_i}\,\tilde{\boldsymbol{K}}^{-1}_{[1:L]\,[1:L]})\\ &\qquad(\boldsymbol{Y}_{[1:L]} - m\mathbf{1}_{J_{[1:L]}}) - \frac{1}{2}\mathrm{tr}(\tilde{\boldsymbol{K}}^{-1}_{[1:L]\,[1:L]}\,\frac{\partial\,\tilde{\boldsymbol{K}}_{[1:L]\,[1:L]}}{\partial\,\theta_i})\end{aligned}$$

We can rewrite the above equation by defining $\boldsymbol{\alpha} = \tilde{\boldsymbol{K}}^{-1}_{[1:L]\,[1:L]}(\boldsymbol{Y}_{[1:L]} - m\mathbf{1}_{J_{[1:L]}})$ and taking trace of the rightmost term to cycle the order of multiplication. Then, the above equation can be rewritten as:

$$\begin{aligned}\frac{\partial\log p(\boldsymbol{Y}_{L+1}|\boldsymbol{X}_U,\boldsymbol{\Gamma})}{\partial\theta_i} &= -\frac{1}{2}\mathrm{tr}(\tilde{\boldsymbol{K}}^{-1}_{[1:L]\,[1:L]}\,\frac{\partial\,\tilde{\boldsymbol{K}}_{[1:L]\,[1:L]}}{\partial\,\theta_i}) + \frac{1}{2}\mathrm{tr}(\boldsymbol{\alpha}^T\,\frac{\partial\,\tilde{\boldsymbol{K}}_{[1:L]\,[1:L]}}{\partial\,\theta_i}\,\boldsymbol{\alpha})\\ &= \frac{1}{2}\mathrm{tr}\big((\boldsymbol{\alpha}\,\boldsymbol{\alpha}^T - \tilde{\boldsymbol{K}}^{-1}_{[1:L]\,[1:L]})\frac{\partial\,\tilde{\boldsymbol{K}}_{[1:L]\,[1:L]}}{\partial\,\theta_i}\big)\end{aligned}$$

The above equation holds for any covariance function that may use in the STGP model. For the squared exponential function, we first estimate the hyperparameter of the ridge term (i.e, σ^2_{noise}). We assume that noise has the same value for each in-control data. As a results, we have:

$$\frac{\partial \tilde{\boldsymbol{K}}_{[1:L]\,[1:L]}}{\partial \sigma^2_{noise}} = \frac{\partial(\boldsymbol{Q}_{[1:L]\,[1:L]} + \tilde{\boldsymbol{\Lambda}}_{[1:L]\,[1:L]})}{\partial \sigma^2_{noise}} = \boldsymbol{I}$$

Next, we take derivative with respect to the signal variance:

$$\frac{\partial \tilde{\boldsymbol{K}}_{[1:L]\,[1:L]}}{\partial \sigma^2_f} = \frac{\partial\, \mathrm{Blockdiag}(\tilde{\boldsymbol{K}}_{[1:L]\,[1:L]})}{\partial \sigma^2_f}$$

$$\frac{\partial \tilde{\boldsymbol{K}}_{[1:L]\,[1:L]}}{\partial \sigma^2_\epsilon} = \frac{\partial(\tilde{\boldsymbol{Q}}_{[1:L]\,[1:L]} - \tilde{\boldsymbol{\Lambda}}_{[1:L]\,[1:L]})}{\partial \sigma^2_\epsilon}$$

To estimate the correlation hyperparameters, we take derivatives for each input dimension. Using all these derivatives, we are able to implement the gradient ascent algorithm to optimize the log-likelihood function.

The last hyperparameter is the mean (i.e., m_f), which is assumed to be a constant prior. Note that the covariance matrix $\tilde{\boldsymbol{K}}_{[1:L]\,[1:L]}$ does not depend on the m_f, but relies on $m\mathbf{1}_{J_{[1:L]}}$.

$$\begin{aligned}\frac{\partial \log p(\boldsymbol{Y}_{L+1}|\boldsymbol{X}_U, \boldsymbol{\Gamma})}{\partial m_f} &= \frac{\partial \frac{-1}{2}(\boldsymbol{Y}_{[1:L]} - m\mathbf{1}_{J_{[1:L]}})^T(\tilde{\boldsymbol{K}}^{-1}_{[1:L]\,[1:L]})(\boldsymbol{Y}_{[1:L]} - m\mathbf{1}_{J_{[1:L]}})}{\partial m_f} \\ &= \mathbf{1}^T_{J_{[1:L]}}\tilde{\boldsymbol{K}}^{-1}_{[1:L]\,[1:L]}(\boldsymbol{Y}_{[1:L]} - m\mathbf{1}_{J_{[1:L]}})\end{aligned}$$

It is worth mentioning that we can analytically find the optimal m_f, which occurs when the above derivative equals zero.

$$m_f = \frac{\mathbf{1}^T_{J_{[1:L]}}\tilde{\boldsymbol{K}}^{-1}_{[1:L]\,[1:L]}\,\boldsymbol{Y}_{[1:L]}}{\mathbf{1}^T_{J_{[1:L]}}\tilde{\boldsymbol{K}}^{-1}_{[1:L]\,[1:L]}\,\mathbf{1}_{J_{[1:L]}}}$$

As a result, it is conducive to set the mean hyperparameters to the above value.

Bibliography

[1] Abdelrahman, M., E. W. Reutzel, A. R. Nassar, and T. L. Starr (2017) "Flaw detection in powder bed fusion using optical imaging," *Additive Manufacturing*, **15**, pp. 1–11.

[2] Imani, F., A. Gaikwad, M. Montazeri, P. Rao, H. Yang, and E. Reutzel (2018) "Process Mapping and In-Process Monitoring of Porosity in Laser Powder Bed Fusion Using Layerwise Optical Imaging," *Journal of Manufacturing Science and Engineering*, **140**(10), pp. 101009–1–101009–14.

[3] Simpson, T. W. (2019) "Designing for Additive Manufacturing," in *Additive Manufacturing, Second Edition*, CRC Press, pp. 233–268.

[4] Simpson, T. W. (2020) "Book Review: Additive Manufacturing for the Aerospace Industry," *AIAA Journal*, **58**(4), pp. 1901–1902.

[5] Kulkarni, A., A. Vidvans, M. Rifat, G. Bicknell, X. Gong, G. Manogharan, J. Terpenny, and S. Basu (2018) "Scalable Detection of Defects in Additively Manufactured PLA Components," in *ASME 2018 13th International Manufacturing Science and Engineering Conference*, American Society of Mechanical Engineers Digital Collection.

[6] Rifat, M., E. C. DeMeter, and S. Basu (2020) "Microstructure evolution during indentation of Inconel-718 created by additive manufacturing," *Materials Science and Engineering: A*, p. 139204.

[7] Khanzadeh, M., S. Chowdhury, M. A. Tschopp, H. R. Doude, M. Marufuzzaman, and L. Bian (2019) "In-situ monitoring of melt pool images for porosity prediction in directed energy deposition processes," *IISE Transactions*, **51**(5), pp. 437–455.

[8] Kan, C. and H. Yang (2017) "Dynamic network monitoring and control of in situ image profiles from ultraprecision machining and biomanufacturing processes," *Quality and Reliability Engineering International*, **33**(8), pp. 2003–2022.

[9] Kan, C., C. Cheng, and H. Yang (2016) "Heterogeneous recurrence monitoring of dynamic transients in ultraprecision machining processes," *Journal of Manufacturing Systems*, **41**(C), pp. 178–187.

[10] Krauss, H., C. Eschey, and M. Zaeh (2012) "Thermography for monitoring the selective laser melting process," in *Proceedings of the Solid Freeform Fabrication Symposium*, pp. 999–1014.

[11] Rodriguez, E., J. Mireles, C. A. Terrazas, D. Espalin, M. A. Perez, and R. B. Wicker (2015) "Approximation of absolute surface temperature measurements of powder bed fusion additive manufacturing technology using in situ infrared thermography," *Additive Manufacturing*, **5**, pp. 31–39.

[12] Berumen, S., F. Bechmann, S. Lindner, J.-P. Kruth, and T. Craeghs (2010) "Quality control of laser-and powder bed-based Additive Manufacturing (AM) technologies," *Physics procedia*, **5**, pp. 617–622.

[13] Craeghs, T., S. Clijsters, J.-P. Kruth, F. Bechmann, and M.-C. Ebert (2012) "Detection of process failures in layerwise laser melting with optical process monitoring," *Physics Procedia*, **39**, pp. 753–759.

[14] Craeghs, T., S. Clijsters, E. Yasa, F. Bechmann, S. Berumen, and J.-P. Kruth (2011) "Determination of geometrical factors in Layerwise Laser Melting using optical process monitoring," *Optics and Lasers in Engineering*, **49**(12), pp. 1440–1446.

[15] Foster, B., E. Reutzel, A. Nassar, B. Hall, S. Brown, and C. Dickman (2015) "Optical, layerwise monitoring of powder bed fusion," in *Solid Freeform Fabrication Symposium, Austin, TX, Aug*, pp. 10–12.

[16] Gobert, C., E. W. Reutzel, J. Petrich, A. R. Nassar, and S. Phoha (2018) "Application of supervised machine learning for defect detection during metallic powder bed fusion additive manufacturing using high resolution imaging." *Additive Manufacturing*, **21**, pp. 517–528.

[17] Francis, J. and L. Bian (2019) "Deep learning for distortion prediction in laser-based additive manufacturing using big data," *Manufacturing Letters*, **20**, pp. 10–14.

[18] Scime, L. and J. Beuth (2018) "A multi-scale convolutional neural network for autonomous anomaly detection and classification in a laser powder bed fusion additive manufacturing process," *Additive Manufacturing*, **24**, pp. 273–286.

[19] ASTM (2012) *Standard terminology for additive manufacturing technologies*, ASTM International, West Conshohocken, PA, Standard No. ASTM 52900-15.

[20] Gibson, I., D. W. Rosen, B. Stucker, et al. (2014) *Additive manufacturing technologies*, vol. 17, Springer.

[21] O'Regan, P., P. Prickett, R. Setchi, G. Hankins, and N. Jones (2016) "Metal based additive layer manufacturing: variations, correlations and process control," *Procedia Computer Science*, **96**, pp. 216–224.

[22] Guo, N. and M. C. Leu (2013) "Additive manufacturing: technology, applications and research needs," *Frontiers of Mechanical Engineering*, **8**(3), pp. 215–243.

[23] Schmidt, M., M. Merklein, D. Bourell, D. Dimitrov, T. Hausotte, K. Wegener, L. Overmeyer, F. Vollertsen, and G. N. Levy (2017) "Laser based additive manufacturing in industry and academia," *CIRP Annals*, **66**(2), pp. 561–583.

[24] Everton, S. K., M. Hirsch, P. Stravroulakis, R. K. Leach, and A. T. Clare (2016) "Review of in-situ process monitoring and in-situ metrology for metal additive manufacturing," *Materials & Design*, **95**, pp. 431–445.

[25] Gorelik, M. (2017) "Additive manufacturing in the context of structural integrity," *International Journal of Fatigue*, **94**, pp. 168–177.

[26] Seifi, M., M. Gorelik, J. Waller, N. Hrabe, N. Shamsaei, S. Daniewicz, and J. J. Lewandowski (2017) "Progress towards metal additive manufacturing standardization to support qualification and certification," *Jom*, **69**(3), pp. 439–455.

[27] Grasso, M., V. Laguzza, Q. Semeraro, and B. M. Colosimo (2017) "In-process monitoring of selective laser melting: spatial detection of defects via image data analysis," *Journal of Manufacturing Science and Engineering*, **139**(5), p. 051001.

[28] Sames, W. J., F. List, S. Pannala, R. R. Dehoff, and S. S. Babu (2016) "The metallurgy and processing science of metal additive manufacturing," *International Materials Reviews*, **61**(5), pp. 315–360.

[29] Cheng, B. and K. Chou (2015) "Geometric consideration of support structures in part overhang fabrications by electron beam additive manufacturing," *Computer-Aided Design*, **69**, pp. 102–111.

[30] Aboulkhair, N. T., N. M. Everitt, I. Ashcroft, and C. Tuck (2014) "Reducing porosity in AlSi10Mg parts processed by selective laser melting," *Additive Manufacturing*, **1**, pp. 77–86.

[31] Mahmoudi, M., A. Elwany, A. Yadollahi, S. M. Thompson, L. Bian, and N. Shamsaei (2017) "Mechanical properties and microstructural characterization of selective laser melted 17-4 PH stainless steel," *Rapid Prototyping Journal*, **23**(2), pp. 280–294.

[32] Bi, G., C. Sun, and A. Gasser (2013) "Study on influential factors for process monitoring and control in laser aided additive manufacturing," *Journal of Materials Processing Technology*, **213**(3), pp. 463–468.

[33] Imani, F., A. Gaikwad, M. Montazeri, P. Rao, H. Yang, and E. Reutzel (2018) "Layerwise in-process quality monitoring in laser powder bed fusion," in *ASME 2018 13th International Manufacturing Science and Engineering Conference*, American Society of Mechanical Engineers, p. V001T01A038.

[34] Imani, F., B. Yao, R. Chen, P. Rao, and H. Yang (2018) "Fractal pattern recognition of image profiles for manufacturing process monitoring and control," in *ASME 2018 13th International Manufacturing Science and Engineering Conference*, American Society of Mechanical Engineers, p. V003T02A003.

[35] Yao, B., F. Imani, and H. Yang (2018) "Markov decision process for image-guided additive manufacturing," *IEEE Robotics and Automation Letters*, **3**(4), pp. 2792–2798.

[36] Rao, S., R. Cunningham, T. Ozturk, and A. D. Rollett (2016) "Measurement and Analysis of Porosity in Al-10Si-1Mg Components Additively Manufactured by Selective Laser Melting," *Materials Performance and Characterization*, **5**(5), pp. 701–716.

[37] Maskery, I., N. Aboulkhair, M. Corfield, C. Tuck, A. Clare, R. K. Leach, R. D. Wildman, I. Ashcroft, and R. J. Hague (2016) "Quantification and characterisation of porosity in selectively laser melted Al–Si10–Mg using X-ray computed tomography," *Materials Characterization*, **111**, pp. 193–204.

[38] Gong, H., K. Rafi, T. Starr, and B. Stucker (2012) "Effect of defects on fatigue tests of as-built Ti-6Al-4V parts fabricated by selective laser melting," in *Solid freeform fabrication symposium*, University of Texas Austin, Texas, pp. 499–506.

[39] DebRoy, T., H. Wei, J. Zuback, T. Mukherjee, J. Elmer, J. Milewski, A. Beese, A. Wilson-Heid, A. De, and W. Zhang (2017) "Additive manufacturing of metallic components–process, structure and properties," *Progress in Materials Science*.

[40] Gong, H., K. Rafi, H. Gu, G. J. Ram, T. Starr, and B. Stucker (2015) "Influence of defects on mechanical properties of Ti–6Al–4 V components produced by selective laser melting and electron beam melting," *Materials & Design*, **86**, pp. 545–554.

[41] Khairallah, S. A., A. T. Anderson, A. Rubenchik, and W. E. King (2016) "Laser powder-bed fusion additive manufacturing: Physics of complex melt flow and formation mechanisms of pores, spatter, and denudation zones," *Acta Materialia*, **108**, pp. 36–45.

[42] Gong, H., K. Rafi, H. Gu, T. Starr, and B. Stucker (2014) "Analysis of defect generation in Ti–6Al–4V parts made using powder bed fusion additive manufacturing processes," *Additive Manufacturing*, **1**, pp. 87–98.

[43] King, W. E., H. D. Barth, V. M. Castillo, G. F. Gallegos, J. W. Gibbs, D. E. Hahn, C. Kamath, and A. M. Rubenchik (2014) "Observation of keyhole-mode laser melting in laser powder-bed fusion additive manufacturing," *Journal of Materials Processing Technology*, **214**(12), pp. 2915–2925.

[44] Beuth, J., J. Fox, J. Gockel, C. Montgomery, R. Yang, H. Qiao, E. Soylemez, P. Reeseewatt, A. Anvari, S. Narra, et al. (2013) "Process mapping for qualification across multiple direct metal additive manufacturing processes," in *Proceedings of SFF Symposium., Austin, TX*, pp. 12–14.

[45] Beuth, J. and N. Klingbeil (2001) "The role of process variables in laser-based direct metal solid freeform fabrication," *Jom*, **53**(9), pp. 36–39.

[46] Vasinonta, A., J. L. Beuth, and M. Griffith (2007) "Process maps for predicting residual stress and melt pool size in the laser-based fabrication of thin-walled structures," *Journal of Manufacturing Science and Engineering*, **129**(1), pp. 101–109.

[47] Morgan, R., A. Papworth, C. Sutcliffe, P. Fox, and W. O'neill (2002) "High density net shape components by direct laser re-melting of single-phase powders," *Journal of Materials Science*, **37**(15), pp. 3093–3100.

[48] Montazeri, M., R. Yavari, P. Rao, and P. Boulware (2018) "In-process Monitoring of Material Cross-Contamination Defects in Laser Powder Bed Fusion," *Journal of Manufacturing Science and Engineering*, pp. 111001–111001–19.

[49] Gu, H., H. Gong, D. Pal, K. Rafi, T. Starr, and B. Stucker (2013) "Influences of energy density on porosity and microstructure of selective laser

melted 17-4PH stainless steel," in *2013 Solid Freeform Fabrication Symposium*, vol. 474.

[50] Rafi, H. K., D. Pal, N. Patil, T. L. Starr, and B. E. Stucker (2014) "Microstructure and mechanical behavior of 17-4 precipitation hardenable steel processed by selective laser melting," *Journal of materials engineering and performance*, **23**(12), pp. 4421–4428.

[51] Rafi, H. K., T. L. Starr, and B. E. Stucker (2013) "A comparison of the tensile, fatigue, and fracture behavior of Ti–6Al–4V and 15-5 PH stainless steel parts made by selective laser melting," *The International Journal of Advanced Manufacturing Technology*, **69**(5-8), pp. 1299–1309.

[52] Mani, M., B. M. Lane, M. A. Donmez, S. C. Feng, and S. P. Moylan (2017) "A review on measurement science needs for real-time control of additive manufacturing metal powder bed fusion processes," *International Journal of Production Research*, **55**(5), pp. 1400–1418.

[53] Tapia, G. and A. Elwany (2014) "A review on process monitoring and control in metal-based additive manufacturing," *Journal of Manufacturing Science and Engineering*, **136**(6), p. 060801.

[54] Mani, M., S. Feng, B. Lane, A. Donmez, S. Moylan, and R. Fesperman (2015) *Measurement science needs for real-time control of additive manufacturing powder bed fusion processes*, US Department of Commerce, National Institute of Standards and Technology.

[55] Spears, T. G. and S. A. Gold (2016) "In-process sensing in selective laser melting (SLM) additive manufacturing," *Integrating Materials and Manufacturing Innovation*, **5**(1), p. 2.

[56] Lane, B., S. Moylan, E. P. Whitenton, and L. Ma (2016) "Thermographic measurements of the commercial laser powder bed fusion process at NIST," *Rapid prototyping journal*, **22**(5), pp. 778–787.

[57] Reutzel, E. and A. Nassar (2014) "A survey of sensing and control for metal-based additive manufacturing," in *Solid Free. Fabr. Symp. Proc. Univ. Tex. Austin TX*.

[58] Nassar, A., T. Spurgeon, and E. Reutzel (2014) "Sensing defects during directed-energy additive manufacturing of metal parts using optical emissions spectroscopy," in *Solid Free. Fabr. Symp. Proc. Univ. Tex. Austin TX*.

[59] Dunbar, A. J., A. R. Nassar, E. W. Reutzel, and J. J. Blecher "A real-time communication architecture for metal powder bed fusion additive manufacturing," in *Annual International Solid Freefrom Fabrication Symposium*, pp. 67–80.

[60] Foster, B. K., E. W. Reutzel, A. R. Nassar, C. J. Dickman, and B. T. Hall (2015) "A brief survey of sensing for metal-based powder bed fusion additive manufacturing," in *Dimensional Optical Metrology and Inspection for Practical Applications Iv*, vol. 9489, International Society for Optics and Photonics, p. 94890B.

[61] Boulware, P. (2016) "Final Technical Report to National Institute of Standards and Technology and National Center for Defense Manufacturing and Machining-Measurement Science Innovation Program for Additive Manufacturing: An Evaluation of In-Process Sensing Techniques Through the Use of an Open Architecture Laser Powder Bed Fusion Platform," *Edison Welding Institute (EWI), Cincinnati, OHNIST*.

[62] zur Jacobsmühlen, J., S. Kleszczynski, D. Schneider, and G. Witt (2013) "High resolution imaging for inspection of laser beam melting systems," in *Instrumentation and Measurement Technology Conference (I2MTC), 2013 IEEE International*, IEEE, pp. 707–712.

[63] Kleszczynski, S., J. zur Jacobsmühlen, B. Reinarz, J. T. Sehrt, G. Witt, and D. Merhof "Improving process stability of laser beam melting systems," in *Fraunhofer Direct Digital Manufacturing Conference*, pp. 1–6.

[64] Kleszczynski, S., J. Zur Jacobsmühlen, J. Sehrt, and G. Witt (2012) "Error detection in laser beam melting systems by high resolution imaging," in *Proceedings of the twenty third annual international solid freeform fabrication symposium*, vol. 2012, pp. 975–987.

[65] Wegner, A. and G. Witt (2011) "Process monitoring in laser sintering using thermal imaging," in *SFF Symposium, Austin, Texas, USA*, pp. 8–10.

[66] Calta, N. P., J. Wang, A. M. Kiss, A. A. Martin, P. J. Depond, G. M. Guss, V. Thampy, A. Y. Fong, J. N. Weker, K. H. Stone, et al. (2018) "An instrument for in situ time-resolved X-ray imaging and diffraction of laser powder bed fusion additive manufacturing processes," *Review of Scientific Instruments*, **89**(5), p. 055101.

[67] Hu, D. and R. Kovacevic (2003) "Sensing, modeling and control for laser-based additive manufacturing," *International Journal of Machine Tools and Manufacture*, **43**(1), pp. 51–60.

[68] Barua, S., T. Sparks, and F. Liou (2011) "Development of low-cost imaging system for laser metal deposition processes," *Rapid Prototyping Journal*, **17**(3), pp. 203–210.

[69] Rieder, H., A. Dillhöfer, M. Spies, J. Bamberg, and T. Hess (2014) "Online monitoring of additive manufacturing processes using ultrasound," in *11th European Conference on Non-Destructive Testing (ECNDT), Prague, Czech Republic, Oct*, pp. 6–10.

[70] Derakhshani, M., T. Berfield, and K. D. Murphy (2018) "Dynamic Analysis of a Bi-stable Buckled Structure for Vibration Energy Harvester," in *Dynamic Behavior of Materials, Volume 1*, Springer, pp. 199–208.

[71] Chiu, T.-M., M. Mahmoudi, W. Dai, A. Elwany, H. Liang, and H. Castaneda (2018) "Corrosion assessment of Ti-6Al-4V fabricated using laser powder-bed fusion additive manufacturing," *Electrochimica Acta*, **279**, pp. 143–151.

[72] Krauss, H., T. Zeugner, and M. F. Zaeh (2014) "Layerwise monitoring of the selective laser melting process by thermography," *Physics Procedia*, **56**, pp. 64–71.

[73] Melvin III, L. S., S. Das, and S. Beaman Jr (1994) "Video microscopy of selective laser sintering," in *Proceedings of the Solid Freeform Fabrication Symposium, DTIC Document*, pp. 34–41.

[74] Bartkowiak, K. (2010) "Direct laser deposition process within spectrographic analysis in situ," *Physics Procedia*, **5**, pp. 623–629.

[75] Chivel, Y. and I. Smurov (2010) "On-line temperature monitoring in selective laser sintering/melting," *Physics Procedia*, **5**, pp. 515–521.

[76] Craeghs, T., S. Clijsters, E. Yasa, and J.-P. Kruth (2011) "Online quality control of selective laser melting," in *Proceedings of the Solid Freeform Fabrication Symposium, Austin, TX*, pp. 212–226.

[77] Craeghs, T., F. Bechmann, S. Berumen, and J.-P. Kruth (2010) "Feedback control of Layerwise Laser Melting using optical sensors," *Physics Procedia*, **5**, pp. 505–514.

[78] Heigel, J. C. and B. M. Lane (2018) "Measurement of the melt pool length during single scan tracks in a commercial laser powder bed fusion process," *Journal of Manufacturing Science and Engineering*, **140**(5), p. 051012.

[79] Dunbar, A. J. and A. R. Nassar (2018) "Assessment of optical emission analysis for in-process monitoring of powder bed fusion additive manufacturing," *Virtual and Physical Prototyping*, **13**(1), pp. 14–19.

[80] Stutzman, C. B., A. R. Nassar, and E. W. Reutzel (2018) "Multi-sensor investigations of optical emissions and their relations to directed energy deposition processes and quality," *Additive Manufacturing*, **21**, pp. 333–339.

[81] Montazeri, M. and P. Rao (2018) "Sensor-Based Build Condition Monitoring in Laser Powder Bed Fusion Additive Manufacturing Process Using a Spectral Graph Theoretic Approach," *Journal of Manufacturing Science and Engineering*, **140**(9), p. 091002.

[82] Hirsch, M., R. Patel, W. Li, G. Guan, R. K. Leach, S. D. Sharples, and A. T. Clare (2017) "Assessing the capability of in-situ nondestructive analysis during layer based additive manufacture," *Additive Manufacturing*, **13**, pp. 135–142.

[83] Smith, R. J., M. Hirsch, R. Patel, W. Li, A. T. Clare, and S. D. Sharples (2016) "Spatially resolved acoustic spectroscopy for selective laser melting," *Journal of Materials Processing Technology*, **236**, pp. 93–102.

[84] Solomon, C. and T. Breckon (2011) *Fundamentals of Digital Image Processing: A practical approach with examples in Matlab*, John Wiley & Sons.

[85] Chung, F. R. and F. C. Graham (1997) *Spectral graph theory*, 92, American Mathematical Soc.

[86] Shi, J. and J. Malik (2000) "Normalized cuts and image segmentation," *IEEE Transactions on pattern analysis and machine intelligence*, **22**(8), pp. 888–905.

[87] Rao, P. K., O. F. Beyca, Z. Kong, S. T. Bukkapatnam, K. E. Case, and R. Komanduri (2015) "A graph-theoretic approach for quantification of surface morphology variation and its application to chemical mechanical planarization process," *IIE Transactions*, **47**(10), pp. 1088–1111.

[88] Tootooni, M. S., C. Liu, D. Roberson, R. Donovan, P. K. Rao, Z. J. Kong, and S. T. Bukkapatnam (2016) "Online non-contact surface finish measurement in machining using graph theory-based image analysis," *Journal of Manufacturing Systems*, **41**, pp. 266–276.

[89] Mohar, B. (1991) "Eigenvalues, diameter, and mean distance in graphs," *Graphs and combinatorics*, **7**(1), pp. 53–64.

[90] Jiang, X., P. J. Scott, D. Whitehouse, and L. Blunt (2007) "Paradigm shifts in surface metrology. Part II. The current shift," in *Proceedings of the Royal Society of London A: Mathematical, Physical and Engineering Sciences*, vol. 463, The Royal Society, pp. 2071–2099.

[91] Jiang, X., P. J. Scott, D. Whitehouse, and L. Blunt (2007) "Paradigm shifts in surface metrology. Part I. Historical philosophy," in *Proceedings of the*

Royal Society of London A: Mathematical, Physical and Engineering Sciences, vol. 463, The Royal Society, pp. 2049–2070.

[92] WHITEHOUSE, D. J. (2010) *Handbook of surface and nanometrology*, CRC press.

[93] YAO, B., F. IMANI, A. S. SAKPAL, E. REUTZEL, and H. YANG (2018) "Multifractal analysis of image profiles for the characterization and detection of defects in additive manufacturing," *Journal of Manufacturing Science and Engineering*, **140**(3), p. 031014.

[94] YANG, H. and Y. CHEN (2014) "Heterogeneous recurrence monitoring and control of nonlinear stochastic processes," *Chaos: An Interdisciplinary Journal of Nonlinear Science*, **24**(1), p. 013138.

[95] FEDER, J. (1988) "Fractals (physics of solids and liquids)," *New York: Plenu*.

[96] MEISEL, L., M. JOHNSON, and P. COTE (1992) "Box-counting multifractal analysis," *Physical Review A*, **45**(10), p. 6989.

[97] BARNSLEY, M. F. and S. DEMKO (1985) "Iterated function systems and the global construction of fractals," *Proc. R. Soc. Lond. A*, **399**(1817), pp. 243–275.

[98] CHHABRA, A. and R. V. JENSEN (1989) "Direct determination of the f (α) singularity spectrum," *Physical Review Letters*, **62**(12), p. 1327.

[99] FABIO, D., A. REIS, and R. RIERA (1994) "Lacunarity calculation in the true fractal limit," *Journal of Physics A: Mathematical and General*, **27**(6), p. 1827.

[100] TOLLE, C. R., T. R. MCJUNKIN, and D. J. GORSICH (2008) "An efficient implementation of the gliding box lacunarity algorithm," *Physica D: Nonlinear Phenomena*, **237**(3), pp. 306–315.

[101] IMANI, F. and K.-H. G. BAE (2017) "Preventive maintenance modelling in lifetime warranty," *International Journal of Quality Engineering and Technology*, **6**(4), pp. 249–268.

[102] IMANI, F., H. SHAHRIARI, and A. A. HADAD (2013) "An optimal preventive maintenance policy during the lifetime warranty," *Technical Journal of Engineering and Applied Sciences*, **3**(24), pp. 3525–3533.

[103] SALTZMAN, D., M. BICHNEVICIUS, S. LYNCH, T. W. SIMPSON, E. W. REUTZEL, C. DICKMAN, and R. MARTUKANITZ (2018) "Design and evaluation of an additively manufactured aircraft heat exchanger," *Applied Thermal Engineering*, **138**, pp. 254–263.

[104] Flank, S., A. R. Nassar, T. W. Simpson, N. Valentine, and E. Elburn (2017) "Fast authentication of metal additive manufacturing," *3D Printing and Additive Manufacturing*, **4**(3), pp. 143–148.

[105] Jiang, X., P. J. Scott, D. Whitehouse, and L. Blunt (2007) "Paradigm shifts in surface metrology. Part II. The current shift," in *Proceedings of the Royal Society of London A: Mathematical, Physical and Engineering Sciences*, vol. 463, The Royal Society, pp. 2071–2099.

[106] Kumara, S. and S. Bukkapatnam (2007) "Characterization and monitoring of nonlinear dynamics and chaos in manufacturing enterprise systems," in *Network Science, Nonlinear Science and Infrastructure Systems*, Springer, pp. 99–122.

[107] Gültekin, M., E. Elsayed, J. English, and A. Hauksdottir (2002) "Monitoring automatically controlled processes using statistical control charts," *International Journal of Production Research*, **40**(10), pp. 2303–2320.

[108] Singer, G. and I. Ben-Gal (2007) "The funnel experiment: The Markov-based SPC approach," *Quality and Reliability Engineering International*, **23**(8), pp. 899–913.

[109] Yang, H. (2011) "Multiscale recurrence quantification analysis of spatial cardiac vectorcardiogram signals," *IEEE Transactions on Biomedical Engineering*, **58**(2), pp. 339–347.

[110] Chen, Y. and H. Yang (2016) "Numerical simulation and pattern characterization of nonlinear spatiotemporal dynamics on fractal surfaces for the whole-heart modeling applications," *The European Physical Journal B*, **89**(8), pp. 1–16.

[111] Chen, R., F. Imani, and H. Yang (2019) "Heterogeneous recurrence analysis of disease-altered spatiotemporal patterns in multi-channel cardiac signals," *IEEE Journal of Biomedical and Health Informatics*, **24**(6), pp. 1619–1631.

[112] Ruschin-Rimini, N., I. Ben-Gal, and O. Maimon (2013) "Fractal geometry statistical process control for non-linear pattern-based processes," *IIE transactions*, **45**(4), pp. 355–373.

[113] Majumdar, A. and B. Bhushan (1990) "Role of fractal geometry in roughness characterization and contact mechanics of surfaces," *Journal of tribology*, **112**(2), pp. 205–216.

[114] Jahn, R. and H. Truckenbrodt (2004) "A simple fractal analysis method of the surface roughness," *Journal of Materials Processing Technology*, **145**(1), pp. 40–45.

[115] Davies, S. and P. Hall (1999) "Fractal analysis of surface roughness by using spatial data," *Journal of the Royal Statistical Society: Series B (Statistical Methodology)*, **61**(1), pp. 3–37.

[116] Gefen, Y., A. Aharony, and B. B. Mandelbrot (1984) "Phase transitions on fractals. III. Infinitely ramified lattices," *Journal of Physics A: Mathematical and General*, **17**(6), p. 1277.

[117] Plotnick, R. E., R. H. Gardner, W. W. Hargrove, K. Prestegaard, and M. Perlmutter (1996) "Lacunarity analysis: a general technique for the analysis of spatial patterns," *Physical review E*, **53**(5), p. 5461.

[118] Allain, C. and M. Cloitre (1991) "Characterizing the lacunarity of random and deterministic fractal sets," *Physical review A*, **44**(6), p. 3552.

[119] Beyca, O. F., P. K. Rao, Z. Kong, S. T. Bukkapatnam, and R. Komanduri (2016) "Heterogeneous sensor data fusion approach for real-time monitoring in ultraprecision machining (UPM) process using non-parametric bayesian clustering and evidence theory," *IEEE Transactions on Automation Science and Engineering*, **13**(2), pp. 1033–1044.

[120] Bourell, D. L. (2016) "Perspectives on additive manufacturing," *Annual Review of Materials Research*, **46**, pp. 1–18.

[121] Imani, F., B. Yao, R. Chen, P. Rao, and H. Yang (2019) "Joint Multifractal and Lacunarity Analysis of Image Profiles for Manufacturing Quality Control," *Journal of Manufacturing Science and Engineering*, **141**(4), p. 044501.

[122] Imani, F., R. Chen, C. Tucker, and H. Yang (2019) "Random Forest Modeling for Survival Analysis of Cancer Recurrences," in *2019 IEEE 15th International Conference on Automation Science and Engineering (CASE)*, IEEE, pp. 399–404.

[123] Malekipour, E. and H. El-Mounayri (2018) "Defects, Process Parameters and Signatures for Online Monitoring and Control in Powder-Based Additive Manufacturing," in *Mechanics of Additive and Advanced Manufacturing, Volume 9*, Springer, pp. 83–90.

[124] Amini, M. and S. Chang (2017) "Assessing Data Veracity for Data-Rich Manufacturing," in *IIE Annual Conference. Proceedings*, Institute of Industrial and Systems Engineers (IISE), pp. 1661–1666.

[125] Tang, M., P. C. Pistorius, and J. L. Beuth (2017) "Prediction of lack-of-fusion porosity for powder bed fusion," *Additive Manufacturing*, **14**, pp. 39–48.

[126] Momenzadeh, N., S. Nath, T. Berfield, and S. Atre (2019) "In Situ Measurement of Thermal Strain Development in 420 Stainless Steel Additive Manufactured Metals," *Experimental Mechanics*, pp. 1–9.

[127] Kim, W., K. Mechitov, J.-Y. Choi, and S. Ham (2005) "On target tracking with binary proximity sensors," in *Information Processing in Sensor Networks, 2005. IPSN 2005. Fourth International Symposium on*, IEEE, pp. 301–308.

[128] Cheng, B., B. Lane, J. Whiting, and K. Chou (2018) "A Combined Experimental-Numerical Method to Evaluate Powder Thermal Properties in Laser Powder Bed Fusion," *Journal of manufacturing science and engineering*, **140**(11), pp. 111008–1–111008–8.

[129] Cerniglia, D., M. Scafidi, A. Pantano, and J. Rudlin (2015) "Inspection of additive-manufactured layered components," *Ultrasonics*, **62**, pp. 292–298.

[130] Leach, R. (2011) *Optical measurement of surface topography*, vol. 14, Springer.

[131] Bayle, F. and M. Doubenskaia (2008) "Selective laser melting process monitoring with high speed infra-red camera and pyrometer," in *Fundamentals of laser assisted micro-and nanotechnologies*, vol. 6985, International Society for Optics and Photonics, p. 698505.

[132] Mahmoudi, M., A. A. Ezzat, and A. Elwany (2019) "Layerwise anomaly detection in laser powder-bed fusion metal additive manufacturing," *Journal of Manufacturing Science and Engineering*, **141**(3), p. 031002.

[133] Kruth, J.-P., P. Mercelis, J. Van Vaerenbergh, and T. Craeghs (2007) "Feedback control of selective laser melting," in *Proceedings of the 3rd international conference on advanced research in virtual and rapid prototyping*, pp. 521–527.

[134] Kruth, J.-P., J. Duflou, P. Mercelis, J. Van Vaerenbergh, T. Craeghs, and J. De Keuster (2007) "On-line monitoring and process control in selective laser melting and laser cutting," in *Proceedings of the 5th Lane Conference, Laser Assisted Net Shape Engineering*, vol. 1, pp. 23–37.

[135] Clijsters, S., T. Craeghs, S. Buls, K. Kempen, and J.-P. Kruth (2014) "In situ quality control of the selective laser melting process using a high-speed, real-time melt pool monitoring system," *The International Journal of Advanced Manufacturing Technology*, **75**(5-8), pp. 1089–1101.

[136] Seifi, S. H., W. Tian, H. Doude, M. A. Tschopp, and L. Bian (2019) "Layer-wise modeling and anomaly detection for laser-based additive manufacturing," *Journal of Manufacturing Science and Engineering*, pp. 081013–1–081013–12.

[137] Chen, R., F. Imani, E. Reutzel, and H. Yang (2019) "From Design Complexity to Build Quality in Additive Manufacturing—A Sensor-Based Perspective," *IEEE Sensors Letters*, **3**(1), pp. 1–4.

[138] Malekipour, E. and H. El-Mounayri (2018) "Common defects and contributing parameters in powder bed fusion AM process and their classification for online monitoring and control: a review," *The International Journal of Advanced Manufacturing Technology*, **95**(1-4), pp. 527–550.

[139] Yavari, M. R., K. D. Cole, and P. Rao (2019) "Thermal Modeling in Metal Additive Manufacturing Using Graph Theory," *Journal of Manufacturing Science and Engineering*, **141**(7), pp. 071007–1–071007–20.

[140] Sun, T.-H., F.-C. Tien, F.-C. Tien, and R.-J. Kuo (2016) "Automated thermal fuse inspection using machine vision and artificial neural networks," *Journal of Intelligent Manufacturing*, **27**(3), pp. 639–651.

[141] Librantz, A. F., S. A. de Araújo, W. A. Alves, P. A. Belan, R. A. Mesquita, and A. H. Selvatici (2017) "Artificial intelligence based system to improve the inspection of plastic mould surfaces," *Journal of Intelligent Manufacturing*, **28**(1), pp. 181–190.

[142] Zhang, Y., G. S. Hong, D. Ye, K. Zhu, and J. Y. Fuh (2018) "Extraction and evaluation of melt pool, plume and spatter information for powder-bed fusion AM process monitoring," *Materials & Design*, **156**, pp. 458–469.

[143] Kwon, O., H. G. Kim, M. J. Ham, W. Kim, G.-H. Kim, J.-H. Cho, N. I. Kim, and K. Kim (2018) "A deep neural network for classification of melt-pool images in metal additive manufacturing," *Journal of Intelligent Manufacturing*, pp. 1–12.

[144] Lloyd, S. (1982) "Least squares quantization in PCM," *IEEE transactions on information theory*, **28**(2), pp. 129–137.

[145] Oliver, M. A. and R. Webster (1990) "Kriging: a method of interpolation for geographical information systems," *International Journal of Geographical Information System*, **4**(3), pp. 313–332.

[146] Krizhevsky, A., I. Sutskever, and G. E. Hinton (2012) "Imagenet classification with deep convolutional neural networks," in *Advances in neural information processing systems*, pp. 1097–1105.

[147] Han, X., Y. Zhong, L. Cao, and L. Zhang (2017) "Pre-trained alexnet architecture with pyramid pooling and supervision for high spatial resolution remote sensing image scene classification," *Remote Sensing*, **9**(8), p. 848.

[148] Nair, V. and G. E. Hinton (2010) "Rectified linear units improve restricted boltzmann machines," in *Proceedings of the 27th international conference on machine learning (ICML-10)*, pp. 807–814.

[149] Chen, R., F. Imani, E. Reutzel, and H. Yang (2018) "From Design Complexity to Build Quality in Additive Manufacturing-A Sensor-based Perspective," *IEEE Sensors Letters*, **3**(1), pp. 1–4.

[150] Rao, P. K., J. P. Liu, D. Roberson, Z. J. Kong, and C. Williams (2015) "Online real-time quality monitoring in additive manufacturing processes using heterogeneous sensors," *Journal of Manufacturing Science and Engineering*, **137**(6), p. 061007.

[151] Wang, K. and W. Jiang (2009) "High-dimensional process monitoring and fault isolation via variable selection," *Journal of Quality Technology*, **41**(3), pp. 247–258.

[152] Bakshi, B. R. (1998) "Multiscale PCA with application to multivariate statistical process monitoring," *AIChE journal*, **44**(7), pp. 1596–1610.

[153] Gaikwad, A., F. Imani, H. Yang, E. Reutzel, and P. Rao (2019) "In Situ Monitoring of Thin-Wall Build Quality in Laser Powder Bed Fusion Using Deep Learning," *Smart and Sustainable Manufacturing Systems*, **3**(1), pp. 98–121.

[154] Gaikwad, A., F. Imani, P. Rao, H. Yang, and E. Reutzel (2019) "Design Rules and In-Situ Quality Monitoring of Thin-Wall Features Made Using Laser Powder Bed Fusion," in *International Manufacturing Science and Engineering Conference*, vol. 58745, American Society of Mechanical Engineers, p. V001T01A039.

[155] Imani, F., R. Chen, E. P. Diewald, E. Reutzel, and H. Yang (2019) "Deep learning of Variant Geometry in Layerwise Imaging Profiles for Additive

Manufacturing Quality Control," *Journal of Manufacturing Science and Engineering*, **141**(11), p. 111001.

[156] Imani, F., R. Chen, E. Diewald, E. Reutzel, and H. Yang (2019) "Image-Guided Variant Geometry Analysis of Layerwise Build Quality in Additive Manufacturing," in *International Manufacturing Science and Engineering Conference*, vol. 58745, American Society of Mechanical Engineers, p. V001T02A041.

[157] Lin, H.-D., C.-Y. Chung, and W.-T. Lin (2008) "Principal component analysis based on wavelet characteristics applied to automated surface defect inspection," *WSEAS Transactions on Computer Research*, **3**(4), pp. 193–202.

[158] Yan, H., K. Paynabar, and J. Shi (2014) "Image-based process monitoring using low-rank tensor decomposition," *IEEE Transactions on Automation Science and Engineering*, **12**(1), pp. 216–227.

[159] Lu, C.-J. and D.-M. Tsai (2005) "Automatic defect inspection for LCDs using singular value decomposition," *The International Journal of Advanced Manufacturing Technology*, **25**(1-2), pp. 53–61.

[160] Wood, B. R., K. R. Bambery, C. J. Evans, M. A. Quinn, and D. McNaughton (2006) "A three-dimensional multivariate image processing technique for the analysis of FTIR spectroscopic images of multiple tissue sections," *BMC medical imaging*, **6**(12), pp. 1–9.

[161] Mei, Y. (2010) "Efficient scalable schemes for monitoring a large number of data streams," *Biometrika*, **97**(2), pp. 419–433.

[162] Megahed, F. M., L. J. Wells, J. A. Camelio, and W. H. Woodall (2012) "A spatiotemporal method for the monitoring of image data," *Quality and Reliability Engineering International*, **28**(8), pp. 967–980.

[163] Xi, X., M. Tang, S. M. Miran, and Z. Luo (2017) "Evaluation of feature extraction and recognition for activity monitoring and fall detection based on wearable sEMG sensors," *Sensors*, **17**(6), p. 1229.

[164] Xi, X., Z. Sun, T. Hua, P. Jiang, S. M. Miran, and X. Li (2019) "Adaptive compensation for measurement error in remote sensing of mobile source emissions," *Measurement*, **148**, p. 106927.

[165] Hung, Y.-C., W.-C. Tsai, S.-F. Yang, S.-C. Chuang, and Y.-K. Tseng (2012) "Nonparametric profile monitoring in multi-dimensional data spaces," *Journal of Process Control*, **22**(2), pp. 397–403.

[166] Miran, S. M., C. Ling, A. Gerard, and L. Rothfusz (2019) "Effect of Providing the Uncertainty Information About a Tornado Occurrence on the Weather Recipients' Cognition and Protective Action: Probabilistic Hazard Information Versus Deterministic Warnings," *Risk Analysis*, **39**(7), pp. 1533–1545.

[167] Cressie, N. and G. Johannesson (2008) "Fixed rank kriging for very large spatial data sets," *Journal of the Royal Statistical Society: Series B (Statistical Methodology)*, **70**(1), pp. 209–226.

[168] Imani, F., C. Cheng, R. Chen, and H. Yang (2019) "Nested Gaussian process modeling and imputation of high-dimensional incomplete data under uncertainty," *IISE Transactions on Healthcare Systems Engineering*, **9**(4), pp. 315–326.

[169] Imani, F., C. Cheng, R. Chen, and H. Yang (2018) "Nested gaussian process modeling for high-dimensional data imputation in healthcare systems," in *IISE 2018 Conference & Expo, Orlando, FL, May*, pp. 19–22.

[170] Liu, J., C. Liu, Y. Bai, P. Rao, C. B. Williams, and Z. Kong (2019) "Layer-wise spatial modeling of porosity in additive manufacturing," *IISE Transactions*, **51**(2), pp. 109–123.

[171] Zhang, L., K. Wang, and N. Chen (2016) "Monitoring wafers' geometric quality using an additive Gaussian process model," *IIE Transactions*, **48**(1), pp. 1–15.

[172] Quiñonero-Candela, J. and C. E. Rasmussen (2005) "A unifying view of sparse approximate Gaussian process regression," *Journal of Machine Learning Research*, **6**, pp. 1939–1959.

[173] Bijl, H., T. B. Schön, J.-W. van Wingerden, and M. Verhaegen (2017) "System identification through online sparse Gaussian process regression with input noise," *Journal of Systems and Control*, **2**, pp. 1–11.

[174] Quiñonero-Candela, J., C. E. Rasmussen, A. R. Figueiras-Vidal, et al. (2010) "Sparse spectrum Gaussian process regression," *Journal of Machine Learning Research*, **11**, pp. 1865–1881.

[175] Nassar, A. R., M. A. Gundermann, E. W. Reutzel, P. Guerrier, M. H. Krane, and M. J. Weldon (2019) "Formation processes for large ejecta and interactions with melt pool formation in powder bed fusion additive manufacturing," *Scientific reports*, **9**(5038), pp. 1–11.

Vita
Farhad Imani

Education

Ph.D. — August 2020
Dual-title in Industrial Engineering and Operations Research
The Pennsylvania State University

M.S. — August 2016
Industrial Engineering
University of Louisville

B.S. — September 2010
Industrial Engineering
University of Science and Culture

Selected Publications

1. **F. Imani**, B. Yao, R. Chen, P. Rao, and H. Yang, "Joint Multifractal and Lacunarity Analysis of Image Profiles for Manufacturing Quality Control," *ASME Journal of Manufacturing Science and Engineering*, Vol. 141, No. 4, p044501, 2019.
2. **F. Imani**, C. Cheng, R. Chen, and H. Yang, "Nested Gaussian Process Modeling and Imputation of High-dimensional Incomplete Data Under Uncertainty," *IISE Transactions on Healthcare Systems Engineering*, Vol. 9, No. 4, p315-326, 2019.
3. **F. Imani**, R. Chen, E. Diewald, E. Reutzel, and H. Yang, "Deep Learning of Variant Geometry in Layerwise Imaging Profiles for Additive Manufacturing Quality Control," *ASME Transactions Journal of Manufacturing Science and Engineering*, Vol. 141, No. 11, p111001, 2019.
4. A. Gaikwad, **F. Imani**, P. Rao, H. Yang, and E. Reutzel, "In-situ Monitoring of Thin-Wall Build Quality in Laser Powder Bed Fusion using Deep Learning," *ASTM Journal of Smart and Sustainable manufacturing systems*, Vol. 3, No. 1, p98-121, 2019.
5. R. Chen, **F. Imani**, and H. Yang, "Heterogeneous Recurrence Analysis of Disease-altered Spatiotemporal Patterns in Multi-channel Cardiac Signals," *IEEE Journal of Biomedical and Health Informatics*, 2019.
6. **F. Imani**, A. Gaikwad, M. Montazeri, P. Rao, H. Yang, and E. Reutzel, "Process Mapping and In-process Monitoring of Porosity in Laser Powder Bed Fusion Using Layerwise Optical Imaging," *ASME Transactions Journal of Manufacturing Science and Engineering*, Vol. 140, No. 10, p101009, 2018.
7. B. Yao, **F. Imani**, H. Yang, and E. Reutzel, "Multifractal Analysis of Image Profiles for the Characterization and Detection of Defects in Additive Manufacturing," *ASME Journal of Manufacturing Science and Engineering*, Vol. 140, No. 3, p031014, 2018.
8. B. Yao, **F. Imani**, and H. Yang, "Markov Decision Process for Image-guided Additive Manufacturing," *IEEE Robotics and Automation Letters*, Vol. 3, No. 4, p2792-2798, 2018.
9. R. Chen, **F. Imani**, E. Reutzel, and H. Yang, "From Design Complexity to Build Quality in Additive Manufacturing - A Sensor-based Perspective," *IEEE Sensor Letters*, Vol. 3, No. 4, p1-4, 2018.

Honors & Awards

- **2020, James E. Marley Graduate Fellowship in Engineering,** The Pennsylvania State University
- **2020, Breakthrough Project,** Highlighted in NSF Web page
- **2019, Brush Graduate Fellowship,** The Pennsylvania State University
- **2019, Featured Article in ISE Magazine,** IISE Transactions on Healthcare Systems Engineering
- **2019, The 3rd Place,** Poster Competition in IAB Meetings, NSF CHOT, Seattle, WA
- **2019, The 2nd Place,** Service Enterprise Engineering Poster Competition, IME, PSU
- **2018, Best Poster Award,** QCRE, IISE Annual Conference, Orlando, FL
- **2018, Best Paper Finalist,** Healthcare Systems Track, IISE Annual Conference, Orlando, FL
- **2018, NSF Student Travel Award,** ASME MSEC, College Station, TX
- **2016 - 2017, Prestigious University Graduate Fellowship,** The Pennsylvania State University
- **2014 - 2016, University Fellowship,** University of Louisville